Doctoral Thesis

Emergent behavior of bacterial collectives: *Pseudomonas aeruginosa* interstitial biofilms

A thesis submitted in fulfilment of the requirements

for the degree of Doctor of Philosophy

School of Mathematical and Physical Sciences

University of Technology Sydney

Author

Cameron James Zachreson

Supervisor

Prof. Milos Toth

May 2017

Certificate of Original Authorship

I, Cameron James Zachreson, certify that the work in this thesis titled, 'Emergent behavior of bacterial collectives: *Pseudomonas aeruginosa* interstitial biofilms' has not previously been submitted for a degree nor has it been submitted as part of requirements for a degree except as fully acknowledged within the text.

I also certify that the thesis has been written by me. Any help that I have received in my research work and the preparation of the thesis itself has been acknowledged. In addition, I certify that all information sources and literature used are indicated in the thesis. This research is supported by an Australian Government Research Training Program Scholarship.

Signature of Student:

Date: 9 May 2017

Acknowledgements

The work presented in this dissertation was carried out under the supervision of Prof. Milos Toth at the School of Mathematical and Physical Sciences, University of Technology Sydney, New South Wales, Australia. The research was conducted in collaboration with Cynthia B. Whitchurch and Lynne Turnbull at The iThree institute, University of Technology Sydney.

I'm particularly grateful to my advisor, Prof. Milos Toth, who provided consistent feedback and valuable critique, despite this project being outside his area of expertise. I guess old dogs can learn new tricks.

Prof. Cynthia B. Whitchurch helped inspire the project, advised me, and made data gathered by her students available to the collaboration. Dr. Erin S. Gloag performed much of the experimental work that served as inspiration for my research. Dr. Christian Wolff inspired me to improve my code and, more importantly, provided moral support in stressful moments. Prof. Prabhakar Ranganathan took part in many useful discussions in the initial stages of the project.

My brother, Alec Zachreson, gave valuable advice on writing style and assisted with proof reading. My friend and colleague Joshua Pritchard also assisted substantially with proof reading. My parents, Lynn and Nick Zachreson, provided encouragement and emotional support throughout the project. I am grateful to my friends Sam Nishanian, Catherine Rose, Luke Van Upstal, Kaie Johansen, Vladimira Rosolova, Russell Sandstrom, Jacqueline Loyola Echeverria, James Bishop, and Chris Elbadawi for their encouragement and for inspiring me with many stimulating discussions.

This research was supported by an Australian Government Research Training Program Scholarship and FEI Company.

Thank you Charles Mingus, Eric Dolphy, Danny Richmond, Mal Waldron, John Coltrane, Miles Davis, Cannonball Adderley, Sun Ra, *et al.* for drowning out the noise.

Contributing Publications

Peer-reviewed publications that contributed to this work:

- Emergent pattern formation in an interstitial biofilm, **Cameron Zachreson**, Christian Wolff, Cynthia B. Whitchurch, and Milos Toth *Physical Review E* - accepted
- Network patterns in exponentially growing 2D biofilms, **Cameron Zachreson**, Xinhui Yap, Erin Gloag, Cynthia B. Whitchurch, and Milos Toth *Physical Review* - under review

Non-Contributing Publications

Peer-reviewed publications not featured in this work containing research undertaken during the PhD program:

- Electron Beam Controlled Restructuring of Luminescence Centers in Polycrystalline Diamond, **Cameron Zachreson**, Aiden Martin, Igor Aharonovich, and Milos Toth, *ACS applied materials & interfaces*, 2014, 6(13), 10367-10372.
- Role of recombination pathway competition in spatially resolved cathodoluminescence spectroscopy, Milos Toth, **Cameron Zachreson**, and Igor Aharonovich, *Applied Physics Letters*, 105(24), 241112.
- Quantum Emission from Defects in Single-Crystalline Hexagonal Boron Nitride, Toan Trong Tran, **Cameron Zachreson**, Amanuel Michael Berhane, Kerem Brau, Russell Guy Sandstrom, Lu Hua Li, Takahi Taniguchi, Kenji Watanabe, Igor Aharonovich, and Milos Toth, *Physical Review Applied*, 5(3), 034005.
- Micro-Patterned Surfaces that Exploit Stigmergy to Inhibit Biofilm Expansion, Erin S. Gloag, Christopher Elbadawi, **Cameron Zachreson**, Igro Aharonovich, Milos Toth, Ian G. Charles, Lynne Turnbull, and Cynthia B. Whitchurch, *Frontiers in Microbiology*, 7, 2157.
- Room temperature quantum emission from cubic silicon carbide nanoparticles, Stefania Castelletto, Brett C. Johnson, **Cameron Zachreson**, David Beke, István Balogh, Takeshi Ohshima, Igor Aharonovich, and Adam Gali, *ACS nano*, 8(8), 7938-7947.
- Bright, water-soluble CeF3 photo-, cathodo-, and X-ray luminescent nanoparticles, Sandhya Clement, Wei Deng, Krystyna Drozdowicz-Tomsia, Deming Liu, **Cameron Zachreson**, and Ewa M. Goldys, *Journal of Nanoparticle Research*, 17(1), 1-9.

Contents

List of Figures

List of Tables

Abstract

In this work, I discuss my investigation into the collective behavior of *Pseudomonas aeruginosa* interstitial biofilms, bacterial systems that exhibit a unique variety of pattern formation. The patterns appear to emerge through some form of *stigmergy*, a term that applies to processes in which the action of an individual leaves a trace in a medium that modifies or stimulates the performance of other actions in the modified location. The term was invented to describe the self-organization processes used by insects such as termites or ants. For the present investigation, I developed a novel agent-based computer simulation of bacterial behavior that explicitly simulates two distinct stigmergy mechanisms. One of these is biological while the other is physical, and the two are mechanistically independent. The physical stigmergy mechanism arises from the deformation of the medium over which the bacteria move, and depends sensitively on the material properties of this medium. The biological stigmergy mechanism arises from secretion and deposition of extracellular polymeric substances that increase the movement rate of bacteria encountering them. My results reveal that neither of these processes alone is sufficient for the formation of the observed patterns. Instead, the morphogenesis mechanism arises from an emergent interplay between them.

Chapter 1

Introduction

1.1 Emergence

Emergence occurs when many individuals come together to form a collective. Individuals can be defined on any scale, from subatomic particles, to galaxies, their additive properties and interactions determining the nature of the collective. Additive properties of individuals sum together (e.g., resource consumption rate of a population of organisms, or the forces exerted by gas molecules on the walls of their container), while interaction effects describe what happens when information is shared between individuals (e.g., trail formation by ants, or the gravitational forces between celestial bodies). Properties of the collective distinct from those of the individuals composing it are the *emergent* properties of the system. There is a familiar adage that describes this concept: *the whole is greater than the sum of its parts*, which is an attempt to describe the occurrence of collective properties distinct from those of the constituent individuals.

As Terrence Deacon pointed out, emergent properties are constructed due to the restriction of individual degrees of freedom during interactions [1]. Take the simple example of a starling flock. An individual bird outside of the flock has many

possibilities available to it: hunting, mating, singing, and all of the individual behaviors that birds enjoy. However, when this starling enters the flock, its individual behavior is reduced to a simple trajectory. A very basic algorithm has been used to explain this behavior that is based on alignment of neighboring trajectories [2–4]. The bird's behavior is now constrained enormously by its existence as a member of a collective, and its survival will be compromised if it deviates from those constraints. However, the collective can do things that an individual bird cannot: it can relocate an entire population, it can protect its members from predation, it can form physical structures unimaginable at the individual level, and influence entire ecosystems.

From this perspective, the adage stated above is false. If we count the individual degrees of freedom, the emergent structure contains much less than the sum of its parts, while through this reduction of individual complexity, new properties are created. This fundamental mechanism of emergence makes it very difficult to predict the properties of a collective by examining the characteristics and behaviors of the constituent individuals in isolation. On the scale of multicellular biology, these individuals themselves emerge from the interactions of their constituent cells. The study of the individual organism can therefore be arbitrarily detailed, and it is unclear how such study could allow one to predict which properties will be relevant to a collective.

Broadly, the detailed study of the individual and the assertion that collective properties can be understood simply through detailed knowledge of individual properties, is called *reductionism*. Given the unpredictability of emergent systems, and the arbitrarily fine detail on which the individual may be studied, the reductionist approach may appear futile in the study of emergence. However, it is a prevalent scientific philosophy in all fields. The intention here is not to devalue reductionist analysis, and it has proven to be a very productive strategy in cases such as deterministic design of drugs and chemical reaction products, particle physics, effective field theories, and mechanics. However, in the study of biological structure development

(morphogenesis) and pattern formation in nonequilibrium conditions, such an approach has limited utility for the reasons stated above. In such cases, the *holistic* approach, the assertion that phenomena may only be understood in reference to the collective, is an attractive prospect. However, the details of how such an approach may be taken, without reference to a reductionist understanding of the individual, is unclear. The historical disconnect between holistic and reductionist philosophy has made understanding the mechanisms of biological emergence an elusive task ever since the problems were first formulated by the ancient greeks [5, 6].

The synthesis of holistic and atomistic models is currently leading the scientific community into a new process for understanding emergent phenomena [7]. The field of molecular dynamics (MD) is a simple case of this. In MD, up to millions of individual molecules or atoms are simulated using high-performance computing. Usually, only interactions between nearest neighbors are considered, and the geometries and potentials describing the constituents lead to interaction effects that give rise to emergent collective properties such as gas pressure, surface tension, aggregation, and magnetism. This example highlights the interplay between holistic and reductionist approaches: by understanding the properties of isolated individuals, it is possible to model the interactions between them. Resulting emergent phenomena can then be understood on the basis of these individual properties and the associated interactions.

Traditionally, MD simulations are used when atoms and molecules are considered as the individual constituents of the system. However, individuals (and the interactions between them) can be defined on any space or time scale. Indeed, the individual, or 'agent'-based approach has been used to describe and simulate a diverse array of biological and social collectives ranging in scale from individual bacteria and amoebas [8–10], to human beings and other large mammals [4, 11], to social systems like cities [12, 13].

Such studies have shown that certain classes of collective patterns and behaviors

appear to have common mechanisms. Surprisingly, these mechanisms do not depend heavily on the scale or complexity of the individuals involved. Such independence on individual complexity appears to apply in a wide variety of 'flocking' phenomena that occur in collectives of bacteria, fish, birds, humans, and herding mammals to name a few [14]. The behavior of these systems is well described by the minimal model of flocking introduced by Reynolds and developed by Tamás Vicsek *et al.* [15, 16]. This model (the 'standard Vicsek model' or SVM) reduces the complexity of the individual to a single point particle described completely by its trajectory, spatial location, and the configuration of nearby particles within its sensory range. The common trait connecting these systems is the ability for one moving individual to align its movement direction to that of its neighbors.

A complementary behavioral phenomenon that occurs in many systems of varying complexity and scale is that of path formation and trail following. This process involves the modification of the environment by a moving individual that affects the behavior of the same or other individuals arriving at the same location at a later point in time. A word used to define this process is *stigmergy*, a term first applied to the collective behavior of termites [17]. In general, stigmergy applies to processes in which some action leaves a trace in a medium that modifies or stimulates the performance of other actions in the modified location [18, 19].

This is a very broad definition. Indeed, it is difficult to think of a biological system in which this process cannot occur. However, whether or not stigmergy leads to collective pattern formation depends heavily on the medium in which activity occurs. The medium's capacity to be modified, and the rates at which modifications form and vanish determine whether or not stigmergy is effective at inducing collective behavior.

In this work, I discuss my investigation into the collective behavior of *Pseudomonas aeruginosa* **interstitial biofilms, bacterial systems that exhibit a unique variety of pattern formation. The patterns appear to emerge**

through some form of stigmergy. To investigate this process, I have developed an agent-based computer simulation of bacterial behavior that explicitly simulates two distinct stigmergy mechanisms. One of these is biological while the other is physical, and the two are mechanistically independent. My results reveal that an emergent interplay between these two processes can explain how the observed patterns form.

P. aeruginosa is a species of gram-negative bacteria, and an opportunistic human pathogen. Individual *P. aeruginosa* cells can move independently through liquids and on surfaces (they are 'motile'). Because they can bind to and spread over surfaces, *P. aeruginosa* cells tend to inhabit interstitial spaces. The term 'interstitial' describes the environment created in the space between two closely apposed surfaces. Such environments are ubiquitous in clinical and biological settings (between, for example, a urinary catheter and the urethral epithelium, a bandage and a burn, or the surfaces of the respiratory epithelium in the lungs). In these spaces, *P. aeruginosa* forms biofilms, densely packed colonies of surface-associated bacteria. While biofilms are often defined as 'sessile' or nonmotile, *P. aeruginosa* and other bacteria like *N. gonorrhea*, *B. subtilis* and *M. xanthus* are motile on surfaces and within biofilms [20], which leads to complex pattern formation processes and emergent migration behaviors.

Much of the research in emergent behaviors of bacteria asks the question: "what properties of the individual determine the behavior of the collective?". Because of the great complexity of organisms, it is challenging to isolate only the aspects of the individual that are responsible for a given collective phenomenon. To narrow the scope of this investigation, it helps to isolate individual properties that affect interactions between individuals. These can be loosely divided into those that determine physical interactions and those that determine biological interactions.

I define 'physical' interactions as those which would exist between inanimate objects with the same physical characteristics as bacteria. The properties affecting such

interactions (shape, texture, hardness, etc.) apply to nonliving as well as living systems, and determine what happens when two individuals come into physical contact. On the other hand, 'biological' properties are those which only apply to living systems, and include phenomena such as substance secretion, metabolism, and biochemical signal processing. Bacterial emergence results from the combination of biological and physical interactions. The relative weight of these two classes depends on the situation considered.

Because the cells composing biofilms are densely packed, the physical interactions between individuals are crucial to the behavior of collectives. High cell density has complex biological consequences as well due to social phenomena such as the altruistic production of common goods (leading to kin selection), and mutually beneficial behaviors such as cooperative metabolism [21, 22]. In this work, I will not focus on social phenomena in metabolism or sub-population selection, but rather emphasize the importance of physical interactions and motility in morphogenesis mechanisms.

The goal of this work is a simulation model of bacterial behavior that maintains a connection with both experiment and general theories of emergence. Therefore, the mechanistic processes that determine the interactions between individuals must be defined and implemented in an experimentally testable framework. A successful implementation will maintain a strong connection with the general principles of collective behavior discovered in minimal models like the SVM and its variants [14, 23].

In Chapter 2, I will begin by reviewing in more detail the literature precedent for this work, with a special focus on stigmergic phenomena in models of bacterial pattern formation. In Chapter 3 I will discuss the conceptual model that underpins the numerical implementation used here. In Chapters 4 and 5 I will go through the results of simulations beginning with the properties of simple individuals and progressively including more phenomena from the conceptual model, which will naturally lead to

collective behavior. I characterize these behaviors using established and novel metrics to quantitatively and mechanistically describe how emergent phenomena arise from the individual-based model. As elements of the system are included, I will describe the numerical implementation of each. Collective behaviors can be studied either in the steady state (constant bacterial density) or in simulations of colony growth, to answer different questions about the pattern formation processes at play. Chapter 4 deals with steady-state conditions, while Chapter 5 pertains to colony growth.

The main findings of this thesis are as follows: the experimentally observed patterns in *P. aeruginosa* interstitial biofilms are the result of a mechanism that combines physical (sematectonic) and biological (marker-based) stigmergy. The sematectonic stigmergy mechanism depends sensitively on the material properties of the surface over which the bacteria move. The marker-based stigmergy mechanism that arises from the excretion of extracellular polymeric substances (EPS) is essential, but due to the stochastic nature of bacterial movement, *insufficient* for the formation of the observed patterns.

Chapter 2

Motivation and Background

2.1 Agent-based models of biofilms

In biofilms, emergent phenomena and collective motion play important roles in proliferation, and may produce significant survival advantages in diverse environments [24–26]. The fundamental principles of collective motion have been explored extensively using minimal simulation models of moving, interacting individuals, and the prospect of applying the insights gained from such studies to understanding infection and disease is very attractive [14, 16, 23]. However, most minimal models of collective motion are not directly applicable to simulations of bacterial colonies due to oversimplification of the interactions between individuals, and between individuals and their enclosing, physical environment. Indeed, the latter is often ignored entirely for the sake of simplicity and generality.

Early attempts at modeling morphogenesis during bacterial colony expansion are exemplified by the 'communicating walkers' (CW) model introduced by Ben-Jacob *et al.* to model colony growth in the bacterial species *Bacillus subtilis* [8]. The CW model framework was developed in order to explain morophological patterns formed by *B. subtilis* colonies as observed by, for example, Matsushita and Fujikawa [27,

28]. These include a uniform, isotropically spreading morphology, a fractal morphology (presumably produced through nutrient diffusion-limited aggregation), a thick-branched morphology, and a remarkable "dense-branched" morphology. These patterns were found to be sensitive to nutrient concentration, agar concentration, and moisture level.

The CW model consists of a collection of point-particles that consume nutrients, divide, move at a rate depending on their nutrition level, and are subject to random perturbations in their velocity direction. The environment is a key aspect of the CW simulation framework and consists of the 'fluid envelope' within which the bacteria move, and the diffusing nutrient field. By repeatedly contacting the the edge of the fluid envelope, the walkers can expand the colony area.

This simple type of model is a surprisingly effective framework for explaining some large-scale observations. For example, the experimentally observed thick-branched and fractal patterns were reproduced by tuning the parameters corresponding to nutrient concentration, consistent with experiment. On the other hand, the dense-branched morphology observed at low nutrient concentration and high moisture level was simulated by including the ability for starving cells to secrete a chemorepellant [8]. This diffusing substance biases movement of other cells away from areas of depleted nutrient concentration, altering morphogenesis.

In general, the CW model is a flexible framework into which a diverse set of biological rules can be implemented without becoming computationally intractable. However, it ignores physical interactions between its agents, a major limitation. One possible reason that physical interactions were not included in the CW model is that the moving particles representing bacteria are best viewed as 'superindividuals'. These represent clusters containing dozens to thousands of cells. In reality, the behavior of clusters emerges from interactions among the constituent individuals which can be exchanged during collisions between groups. These aspects of the system make

it difficult to precisely describe realistic interactions between agents (and between agents and the environment) in superindividual models.

Another factor limiting the usefulness of superindividual models is that most strategies for controlling bacterial proliferation operate on the scale of the true individual. For example, antimicrobial compounds and materials are usually designed to kill individual cells or prevent their attachment to surfaces [29, 30]. Of course, predicting the effect of an individual-level perturbation on the collective requires an appropriate description of the individual. Such a description must include the characteristics necessary to translate the perturbation into altered cell behavior. Hence, useful models must connect the observed behavior to a testable mechanism.

Phenomenological models describe behavior through numerical implementations that do not reflect the underlying mechanism. Such models can describe emergent processes, but provide little capacity to predict how collective behavior could be altered through individual-level perturbation. In models of bacterial motility, the mechanistic details must describe processes such as surface attachment and force application that could in a more abstract model be easily approximated with a mathematically simple, computationally efficient, phenomenological description.

On the other hand, mechanistic simulations at the true individual level are difficult because of the level of detail that is necessary for a useful representation of an individual. To design effective models, individual-level data is required. Fortunately, modern experiments increasingly provide data on cellular or subcellular resolution, and engineering techniques allow the fabrication of materials structured on the scale of individual microbes (see, for example, [31–37]). With these advancements, the coarse picture provided by the CW framework is no longer satisfying.

The most effective models on this challenging scale systematically investigate a particular trait that is of interest with respect to emergence. Interaction mechanisms associated with that characteristic are simulated explicitly with a relatively high degree of detail while using phenomenological rules for other essential behaviors. This

type of approach is exemplified by the work of Fernando Peruani *et al.* [38, 39]. They investigated the role of cell aspect ratio on the clustering behavior of motile, rod-shaped bacteria. Invoking only single-cell motility and elongated shape, they were able to explain how individual bacteria align their movement directions and form large clusters that move collectively. Their simple model of physical interaction produced results that agreed well with experimental observations. This success exemplified how a minimal model can result in realistic emergent behavior despite the great complexity of individual bacteria.

The result is indeed remarkable in its elegance. In other work, clustering behavior had been ascribed to diverse biological mechanisms such as contact-based signaling or quorum sensing [40, 41]. Peruani *et al.*'s work argues convincingly that these higher-order effects are not necessary for giant cluster formation and collective motion of rod-shaped bacteria [38, 39]. Importantly, this result emphasized the significance of individual shape in bacterial collective behavior, due to the way in which collisions between rods tend to align their long-axis orientations.

Recently, Farrell *et al.* and Ghosh *et al.*, have shown that individual shape is also essential to pattern formation during nutrient diffusion-limited colony expansion [42, 43]. These studies focused on cases in which the bacteria grow and divide, but do not actively move (they are nonmotile). Both works pertain to the two-dimensional (2D) case, and it is not known whether the importance of individual shape in determination of emergent morphology applies in three dimensions. For nonmotile bacteria the transition between monolayer (2D) to multilayer (3D) happens inevitably (unless restricted by a microfluidic cell [36]). This occurs even for colonies trapped in the space between two surfaces [44]. The transition from 2D to 3D occurs due to internal pressure exerted by cells growing in the colony interior. Motile bacteria can alleviate such pressure through expansion due to movement, and the monolayer case is quite common in experiments on interstitial biofilms [39, 45–51]. In these moving, 2D bacterial collectives, individual shape and motility will play important roles in emergent behavior.

2.2 Bacterial stigmergy

Another important aspect of bacterial behavior commonly included in more complex agent-based models of motile bacteria is the phenomenon of path formation and trail following. The mechanisms behind such phenomena are examples of *stigmergy*, (as defined in Chapter 1). With the exception of the 'fluid envelope' mechanism as implemented in the CW model of *B. subtilis* [8], stigmergy has been attributed to the creation and following of 'slime trails'. The secretion of slime trails composed of extracellular polymeric substances (EPSs) has indeed been implicated in trail following in *Myxococcus xanthus* [52]. However, the mechanistic role of EPS has not been directly confirmed.

In simulation models, trail following is often implemented in conjunction with many other effects such as chemotaxis, quorum sensing, and contact-based communication [40, 41, 51]. In the case of bacteria, the phenomenon has only recently been the main focus of simulation studies [53–55], even though it has a complex effect on a model's phase space and is extremely important in collective behavior [56]. Existing models of bacterial trail following rely on phenomenological rules, rather than mechanistic description. For this reason, they have not been useful in providing insight into how such a process could be controlled in order to manipulate bacterial behavior.

For simulation work to move from description to predictive modeling, the parameters included in the model must have direct analogs to experimentally determined quantities or distributions. Phenomenological implementations of trail following do not provide this predictive capacity, which can only be obtained with a more detailed implementation that reflects the underlying mechanism.

Recently, Gloag *et al.* conducted experiments to investigate a physical mechanism by which a trail formation process may occur [45]. The proposed mechanism emphasizes the critical interplay between bacterial motility and the properties of the

surrounding environment. The hypothesis was guided by experimental work on interstitial biofilms, where the bacteria are confined to the space between two closely apposed surfaces, and are often confined to a monolayer [45, 48]. The bacteria 'furrow' through the interstitial space, altering the local topography, and creating lasting trail systems that appear to direct collective migration through paths of least resistance. The resulting furrows gradually vanish due to the presence of an apposed surface (e.g., a microscope coverslip), through a process that is likely mediated by capillary forces (see Chapter 3 for a detailed discussion of this process). While topographical modification on agar surfaces has been documented for several types of myxobacteria [52, 57], it had not been systematically investigated or studied quantitatively until the work of Gloag *et al.* [45, 58]. The importance of this process with respect to pattern formation has yet to be determined and this question was a motivation for the present work.

The terms 'sematectonic' and 'marker-based' stigmergy describe two general classes of stigmergic processes. The two differ in the type of mechanism by which the environmental modifications affect individual behavior. Sematectonic stigmergy is *passive* and occurs, for example, through physical perturbation such as a difference in topography or surface texture imparted to the environment by the movement process (i.e., the formation of paths through vegetation) [59]. The furrowing process described by Gloag *et al.* is an example of sematectonic stigmergy [45]. Marker-based stigmergy on the other hand is *deliberate* and requires some shared knowledge and processing of signal information (e.g., an arrow on the ground, or a pheromone signal [60, 61]). Marker-based signals therefore require deliberate interpretation, while sematectonic signals do not. These processes occur in many diverse types of networks of individual agents that move while actively modifying their environment.

Path following, and trail formation processes may combine these two generic mechanistic types. Consider, for example, a human following a line of footprints through the desert. The perturbation is imparted passively and unintentionally into the landscape by the individual who left the prints, a sematectonic process. However,

the follower does not experience a physical perturbation from the footprints and instead follows the trail using a marker-based mechanism requiring the interpretation of footprint trail direction through visual inspection and deduction.

Several published agent-based models of emergent pattern formation in insects and bacteria incorporate stigmergy. Models of ant-trail formation, for example, include terms that bias the movement direction of the ants along pheromone trails deposited in the environment [56, 59–61]. This process is marker-based stigmergy: the ants deposit pheromones deliberately, and interpret the trail direction through spatial sampling and interpretation. In the case of bacterial stigmergy the mechanistic details are not known, and the implementations in simulation models are phenomenological.

In models of bacterial behavior, environmental modification is consistently implemented as a process where no 'decision' is made to leave markers, and trails are created through passive modification of the environment by bacteria secreting slime. Because the path following mechanism is not explicitly implemented in existing models, it cannot be interpreted as either deliberate or passive. Therefore, it is difficult to say whether real bacterial trail formation is sematectonic or marker-based stigmergy. Regardless of the mechanism, there are several fundamental characteristics that are shared by all models of stigmergy [18, 19]:

- individuals modify their local environment at some rate
- an individual responds to modifications by changing its behavior
- the modifications vanish at some rate

The first two of these traits are obviously necessary for any trail following phenomena. However, the necessity for trail degradation is not necessarily intuitive but turns out to be fundamentally important to any type of stigmergic behavior. This aspect of the situation requires two additional assumptions that are consistent with all known examples of stigmergy:

- the modified medium has a finite capacity to sustain modification
- the trails are not followed perfectly

Under these two assumptions, degradation of modifications in the environment prevents the medium from becoming uniform in the saturated condition. If the environment is uniformly saturated, no trails can exist. Saturation can occur even with a finite degradation rate if trail formation is fast enough and trail following noisy enough. The conditions listed above highlight the extreme importance of timescales and fluctuations when modeling stigmergic phenomena (see section 4.3).

For bacteria, these timescales are associated with the mechanistic processes involved in trail formation, trail sensing, individual movement, and trail degradation (which depend on the physico-chemical nature of the trail and medium). Therefore, the descriptive capacity of path following models may be irrelevant to experiments if the appropriate physical and biological constraints on these timescales are not taken explicitly into account.

2.3 Comparison of *P. aeruginosa* and *M. xanthus*

Until recently [54, 55], all simulation models of bacterial trail following have focused on explaining observations in *M. xanthus*. Because we focus here on the behavior of *P. aeruginosa*, it is important to discuss the relevant similarities and differences between the two types of bacteria. While they share the general similarities of rod shape, surface motility via type IV pili (T4P), and the tendency to elongate and divide, there are some important differences.

Firstly, *M. xanthus* possesses another type of motility not observed in *P. aeruginosa*. The so-called adventurous motility (A-motility) appears to be essential to the movement of individual cells away from groups, and allows cells to move continuously in time [32, 62, 63]. As a result, isolated cells can be observed to move in conditions

for which *P. aeruginosa* cells are only observed moving in clusters [45, 58]. Another important difference is the aspect ratio and degree of flexibility. *M. xanthus* cells are longer than *P. aeruginosa* cells and are also more flexible.

T4P motility is polar, that is, at a given point in time the pili are localized at one end of the rod-shaped cell, but not the other. Polarity results in directed motility along the cell's long axis. Spontaneous polarity reversal has been observed in both species. The frequency of polarity reversal in *M. xanthus* is modulated by the *frz* chemosensory system [64]. Recently, polarity reversals in *P. aeruginosa* have been quantified and found to be modulated by the Chp chemosensory system [33]. Interestingly, these measurements on individual cells showed over one order of magnitude slower reversal frequency (less than one reversal per hour), as compared to *M. xanthus*, which has been observed to reverse direction approximately once every 8 minutes [62]. To summarize, *M. xanthus* cells are long, flexible rods that may move continuously or discontinuously, and reverse direction frequently, while *P. aeruginosa* cells are short, rigid rods that move discontinuously, and rarely reverse direction.

Discontinuous movement via T4P is relevant only in situations where either the viscosity of the environment will not allow for movement from flagellar motility (swimming, or swarming), or liquid flow removes cells that are not attached to a surface [33, 65, 66]. In such situations, movement relies on the assembly, extension, attachment, and retraction of pilus fibers that act like grappling hooks pulling the cell body towards the attachment site. Attachment occurs through unspecific, electrostatic interaction between the pilus tip and the binding site [34, 67–69]. The characteristic time and length scales of pilus extension and individual cell movement from retraction have been quantified [34]. This type of motility is especially relevant in confined spaces where the bacteria are in contact with solid surfaces to which their T4P can attach.

In the interstitial environment between, for example, a plastic petri dish and a layer

of agar, a quasi-2D biofilm develops and spreads in a monolayer for extended distances. This behavior has been observed both in *P. aeruginosa*, as well as *M. xanthus* [48, 58]. While this basic description applies to both species, there are distinct differences in the micromorphology. In *P. aeruginosa*, the leading edge of this monolayer is composed of large groups of collectively moving cells, while in *M. xanthus* the leading edge contains many single cells that set out trails which are filled in by the cells arriving later [45, 58]. It is an open question whether these differences in collective morphology can be attributed to the differences in individual characteristics between the two species, or whether there are higher-order communication processes that modify individual behavior in group situations.

Interstitial spaces are ubiquitous in nature and in clinical environments (e.g., medical implant surfaces, the catheter-epithelium interface and contact lenses), and they can readily host notoriously persistent hospital born infections [70–72]. Hence, understanding bacterial motion in such environments will help improve not only the fundamental understanding of emergence in complex biophysical systems, but also the design of biomedical surfaces that reduce the viability of infectious interstitial biofilms [73, 74].

This bacterial system is highly complex, with many possible mechanisms for the formation of patterns. In the next chapter, I define a relatively simple conceptual model that focuses on the T4P-mediated motility of *P. aeruginosa* in the interstitial environment.

Chapter 3

Conceptual Model

3.1 Introduction

The goal of this project is to create a simulation model that provides mechanistic insight and predictive capacity in experiments on emergent pattern formation in *P. aeruginosa* interstitial biofilms [45, 48]. This species of bacteria is useful for studying general principles of bacterial self-propulsion due to the availability of motility mutants [75, 76]. It is also a clinically relevant pathogen responsible for a large portion of catheter-associated urinary tract infections and other medical surface-associated infections [70, 71, 77].

In this chapter, I will describe the concepts that are included in the simulation framework. This basic set of rules is intended to describe bacterial behavior without explicitly modeling biochemical processes. As a result, our model may appear simplistic from the biological perspective. However, even this simplified model leads to a complex and computationally daunting parameter space that from the physical perspective borders on intractable. I have attempted to balance these extremes to create a model that is computationally tractable and physically understandable while including behavioral elements that could be recast as functions of biochemical

processes, depending on the biological or physical questions of interest. The model can be constrained and simplified for demonstrations of basic physical principles of emergence and comparison to simpler models, or it can be expanded to include complex biochemical processes that regulate the behaviorally important phenomena.

The present model bears similarity to others that include rod shape, cell division, and motilty. The aspects of this model that are unique are related to the implementation of T4P-mediated surface motility and the stigmergy mechanisms that arise due to that process. One of these is a type of trail following mediated by preferential attachment of T4P to secreted EPS. The other is a sematectonic stigmergy process where the bacteria modify the topography as they move. Topographical deformation produces resistance opposing movement into unexplored areas. This sematectonic process describes the furrowing behavior observed in real biofilms [45, 52, 57]. These two stigmergy mechanisms are independent. Their timescales and strengths can be tuned arbitrarily to investigate the importance of each and the interplay between them.

3.2 The interstitial environment

In an interstitial biofilm assay, bacteria are grown between a soft surface such as agar, and an abiotic surface such as quartz, silicone polymers such as polydimethysiloxane (PDMS), or the polystyrene surface of a petri dish (Fig. 3.1) [78]. The system attempts to mimic the situation between human tissue and a medical device. The agar is a surrogate for the soft tissue, and the abiotic surface represents the device.

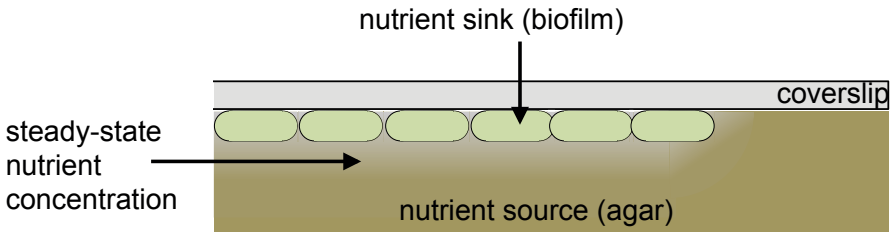

FIGURE 3.1: Schematic of a 2D biofilm growing in an interstitial environment between a coverslip and a slab of nutrient-infused agar. The substratum acts as an effectively infinite source of nutrients. The nutrient concentration near the growing biofilm equilibrates to a concentration determined by the diffusion rate of nutrients through the agar and the nutrient uptake rate of the bacteria.

Bacteria in this environment are initially forced into a monolayer. They will stay in the quasi-2D state unless the internal pressure from expanding cell density forces the system into the multilayered state. The transition from monolayer to multilayer occurs quickly and inevitably if the bacteria are nonmotile [44]. However, the monolayer state can be maintained over much longer culture times if the internal pressure can be relieved due to cell motility. For this reason, the 'twitching motility' assay produces quasi 2D biofilms over large areas [45, 48, 78].

3.3 Cell morphology

3.3.1 Shape

P. aeruginosa cells are rod shaped, and do not bend appreciably during collisions or movement [Fig. 3.2(a)]. Collisions between rod shaped objects lead to alignment of their long-axis orientations [Fig. 3.2(b)], which can lead to collective motion phenomena (see section 4.2) [38, 39]. When nutrients are available, *P. aeruginosa* cells elongate and divide [Fig. 3.2(c)]. Because cell width is approximately constant throughout the growth process and within the population, I use the cell width as the natural length scale of the system. By setting $w \equiv 1$ μm, the cell aspect ratio ($\kappa = l/w$) becomes the metric of interest when deriving model parameters from

experimental data. Aspect ratios and growth rates were calculated by analyzing time-series phase contrast movies of the colony edge [Fig. 3.3(a), Supplemental Movie S1 C.1] and interior [Fig. 3.3(b), Supplemental Movie S2 C.1]. Aspect ratio distributions from the colony edge and interior are given in Figure 3.3(c), and indicate an average aspect ratio between 4 and 5. See Appendix D.1 for details on image processing and Appendix D.2 for a description of aspect ratio calculations.

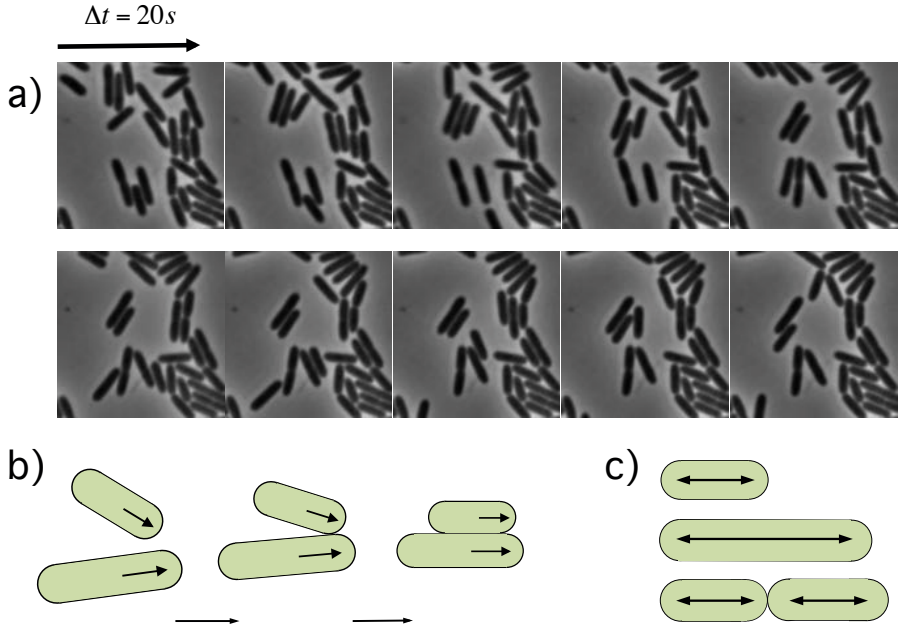

FIGURE 3.2: (a) Time-series phase contrast micrographs of *P. aeruginosa* moving in the interstitial space between a coverslip and a slab of agar. (b, c) Schematic illustrations of cell growth/division (b), and orientational alignment due to collisions (c). (Raw data provided by Erin Gloag and Cynthia Whitchurch [45])

3.3.2 Growth

Due to the 2D nature of the interstitial biofilm we assume constant nutrient availability throughout the system. Such an assumption is possible when diffusion of nutrient molecules through the porous substratum is fast and the substratum is thick [79]. These conditions ensure that nutrient availability is determined by diffusion in the vertical direction, and that the steady-state nutrient concentration at the biofilm-substratum interface remains constant (Fig. 3.1).

In conditions where nutrient availability is constant, individual bacterial cell growth is weakly exponential by mass [31]. For our purposes, the scaling of cell aspect ratio with time is the metric of interest. Specifically, the present work requires a model of cell growth and division that approximates experimentally determined aspect ratio distributions [Fig. 3.3(c)].

The most detailed studies of cell size regulation have been conducted in *E. coli*, and indicate an 'incremental' mechanism whereby each newly divided cell grows until a certain length increment has been added before dividing [80, 81]. Recently, this mechanism was observed in *P. aeruginosa* [82], however, for simplicity the present work uses a 'critical size' linear growth model. In this simple model, the cells elongate at a constant rate and divide at a critical length. This growth law captures the basic behavior of gradual individual elongation followed by division. It is easy to implement, and allows the precise definition of generation time and colony growth rate. We do not expect the substitution of an incremental ('adder'-type) model to alter emergent properties related to motility that are the primary focus of this work.

Importantly, our choice not to explicitly model nutrient uptake is justified based on the data presented in Figure 3.3(d). These histograms of the approximate growth rates for cells on the edge and interior of an interstitial biofilm demonstrate that growth rate does not depend on the position of cells within the colony. The 'growth rate' values reported are linear approximations. They represent $\frac{\Delta\kappa}{\Delta t}$, the total change in aspect ratio κ of individual cells over an interval Δt. See Appendix D.2 for a description of how growth rate values were estimated.

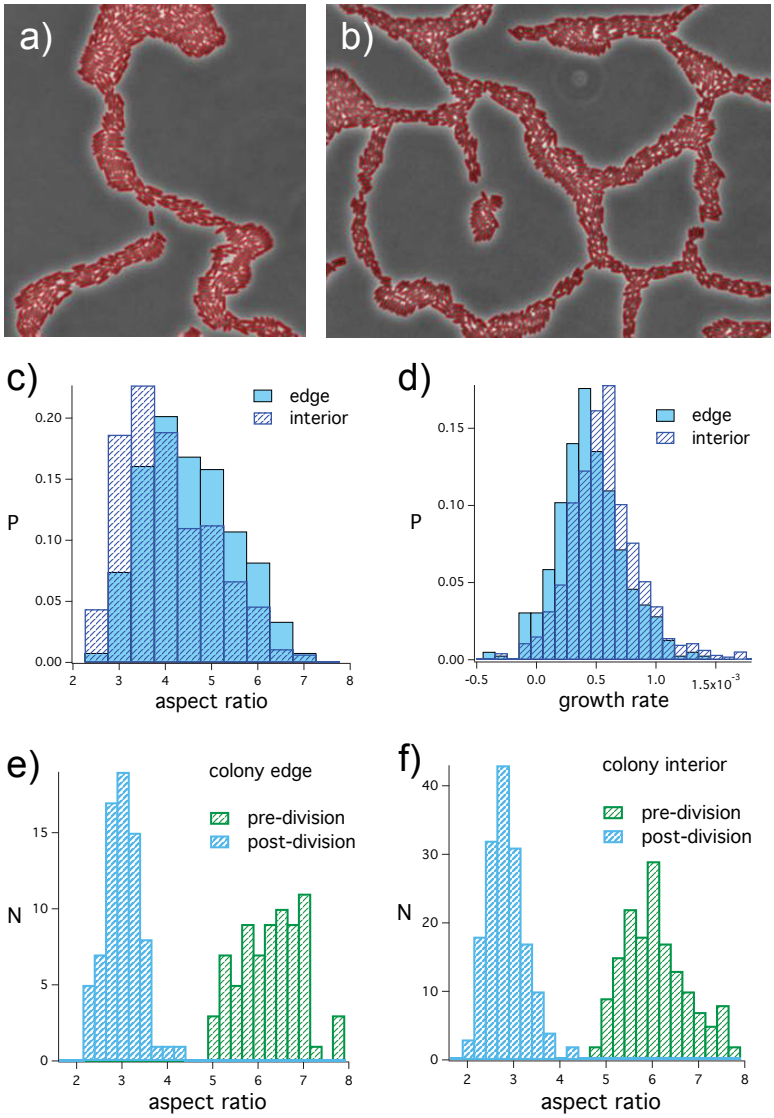

FIGURE 3.3: Phase contrast micrographs of *P. aeruginosa* interstitial biofilms depicting the expanding edge (a), and the interior approximately 200 μm towards the inoculation point (b). Overlaid in red are the binary masks produced by the cell segmentation algorithm detailed in Appendix D.1. Growth statistics in these locations are similar, but vary slightly in aspect ratio distribution (c), and growth rate (linear approximation, see Appendix D.2) (d). The distributions of cell length at division and just after division differ by the expected factor of 2, and are similar near the edge (e), and in the interior (f). (Raw data provided by Erin Gloag and Cynthia Whitchurch [45])

If nutrient depletion were affecting cell growth, slower growth rates would be expected in the colony interior relative to the edge, which is not observed here. On the contrary, the average elongation rate is slightly faster in the colony interior,

with an average of $5.1 \times 10^{-4}\langle w\rangle s^{-1}$ (interior) compared to $3.9 \times 10^{-4}\langle w\rangle s^{-1}$ on the edge (here, $\langle w\rangle$ is the population average cell width). While these distributions are statistically significant (Kolmogorov-Smirnov test, $p = 9.56 \times 10^{-12}$), each of the respective mean values lie within 0.5 standard deviations of the other ($\sigma = 2.9 \times 10^{-4}$, and $\sigma = 3.2 \times 10^{-4}$ for the exterior and interior, respectively). This evidence is intriguing, and further investigation into the counterintuitive result is warranted. However, the distributions in Fig. 3.3(d) are derived from only one dataset for each condition, which is not sufficient to substantiate the conclusion that growth rates are indeed *faster* in the colony interior. Therefore, in our simulations we treat the individual growth rate g, as a fixed parameter, constant throughout the colony.

To further justify this assumption, I used the average linear growth rate (corrected for single-pixel trimming during image processing) of 3.5×10^{-4} μm/s to estimate the constant mass uptake rate of a single bacterium with density 1.16 g/ml (experimentally determined for *E. coli* [83]) and calculated the time required for 10% depletion of a 3 mm nutrient-infused column beneath a bacterium of length 4 μm and width 0.6 μm. I used the nutrient mass concentration of 1 $\times$ LB-Lennox bacterial culture medium (15 mg/ml) multiplied by the column volume as the initial reservoir mass. The time required for 10% depletion of the initial nutrient mass calculated by this simple estimation method is 1.57×10^5 s, or approximately 13.75 division cycles. This is substantially longer than the timescale of interest.

3.3.3 Division

Cell division occurs after some interdivision time, during which the initial cell elongates before dividing into two daughter cells of approximately equal length [Fig. 3.2(c)]. In the *P. aeruginosa* interstitial biofilms studied for this work, cells divide after reaching an aspect ratio between 5 and 8, producing two daughter cells which are each approximately half the length of the dividing cell [Fig. 3.3(e), and 3.3(f)].

While at this point there is not sufficient data to confirm the trend, this analysis shows a tendency for the cells near the colony edge to be longer than those in the interior. See Appendix D.2 for a description of how cell divisions were identified and how pre-, and post-division aspect ratios were determined.

As will be discussed in more detail below, each cell has a general movement direction, or 'polarity', that is defined as the tip of the cell out of which its pili extrude. When cell division occurs, polarity must be assumed for each daughter cell. It is not known whether a systematic mechanism controls this initial polarity. In the present model I decided to give the two daughter cells the same orientation as the initial cell.

3.4 Motility

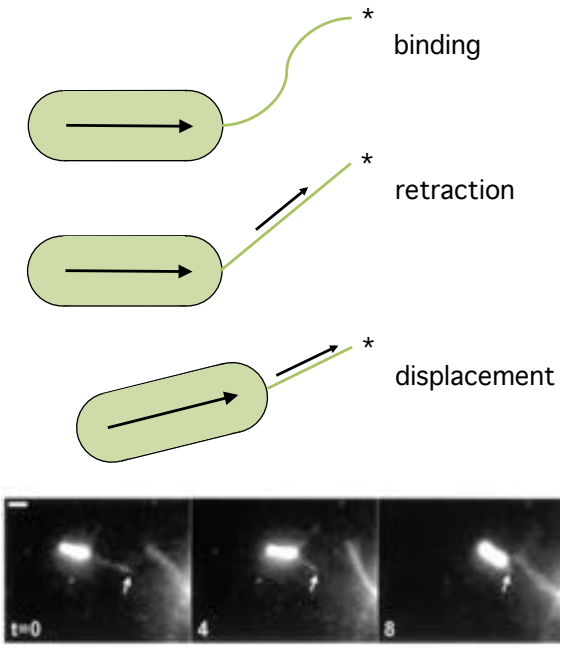

FIGURE 3.4: Twitching motility occurs due to the extension, binding, and retraction of type IV pili, a process that was directly observed by Skerker *et al.* [34]. The fluorescence micrographs in this figure were copied directly from [34].

3.4.1 Mechanism

As mentioned in the previous section, surface-attached *P. aeruginosa* cells can move via the extension, binding, and subsequent retraction type IV pili (or T4P). T4P are long, thin protein fibers composed of thousands of monomeric precursors joined together in a chain [68]. They emerge from assembly protein complexes on the rounded tips of the rod shaped cells and extend into the area in front of a cell's leading pole. The binding site of a pilus fiber is located at its tip [68, 84], and the strands are subject to diffusive fluctuations which would cause them to stochastically sample the area in front of a cell while extended [34]. If the pilus fiber binding site finds purchase, the subsequent retraction will move the cell body towards the binding site. A detailed analysis of this behavior has been provided by Skerker and Berg [34], and this model uses an implementation that can accept the values from that work as inputs. A schematic representation of this process and an example of the dynamics reported in [34] are provided in Figure 3.4(a) and Figure 3.4(b), respectively. The behavior associated with this mechanism is called *twitching* motility due to the discontinuous nature of cell movement [68].

3.4.2 Twitching motility

There are two aspects of twitching motility that make it phenomenologically unique. Firstly, the discontinuous nature of the movement means that the cells can spend substantial amounts of time stationary. Secondly, the spatially random selection of binding site produces fluctuations in movement direction resulting in diffusive transport. For a single cell, the angular diffusion rate contributing to diffusive transport is a function of the parameters defining pilus extension, binding and retraction, including the angular uncertainty between the orientation of a cell's long axis and the angle between the cell pole and the pilus binding site. These properties distinguish twitching motility from other behaviors such as flagellar swarming, or gliding via the binding and translocation of focal adhesions [32].

3.4.3 Polarity reversal

An additional factor important to bacterial surface motility is the tendency for bacteria to reverse direction spontaneously. In twitching motility, this involves extending their pili from the opposite pole and switching the general direction of transport. It has been suggested that the frequency of reversals is modulated by a chemosensory process, but even in the absence of chemical gradients, polarity reversals occur [33]. The reversal frequency is a very important parameter when quantifying diffusive transport, and may be under direct control of intracellular processes. Unlike the other parameters affecting diffusive transport, (attachment probability, friction, random fluctuations), the reversal frequency and retraction frequency are the two parameters that can affect the transport of cells and are also, in principle, controllable on the single-cell level. These mechanisms are therefore clearly of interest when investigating motility adaptation of individual cells.

3.5 Marker-based stigmergy

As discussed in section 2.2, the tendency for surface-motile bacteria to create trails that guide the movement of other cells has been documented for some time, and has been most carefully studied in the species *M. xanthus* [52]. These studies have focused on understanding *M. xanthus* gliding motility, or "Adventurous" motility (A-motility). In *M. xanthus*, trail following has been attributed to the deposition of 'slime trails', or extracellular polymeric substances (EPS) excreted by cells within surface-attached biofilms. In early studies, a propulsion effect was proposed as the primary mechanistic role of EPS excretion in *M. xanthus* motility [62].

In this case, the trail following process could be viewed as a side effect of the motility mechanism responsible for A-motility. However, this theory has been revised in more recent work which shows that *M. xanthus* A-motilty occurs from the attachment and subsequent translocation of focal adhesions along the length of the

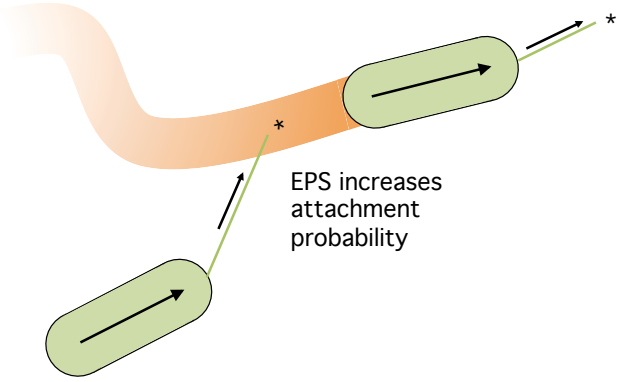

FIGURE 3.5: Extracellular polymeric substances are excreted by bacteria, modifying the surfaces over which they move. This surface modification increases the probability of pilus attachment to previously occupied areas, biasing movement along EPS trails.

cell body [32]. This finding has interesting implications for the mechanistic importance of EPS excretion, since it is not, in this case, directly responsible for the force necessary for cell movement. Instead, the EPS appears to have a primary role in biasing the movement of cells along previously explored trails. The exact mechanism by which this process occurs is not known, and models including this process have relied on phenomenological approaches that are effective in reproducing the experimental observations, but do not provide predictive capacity [40, 41, 51, 53]. Indeed, understanding the mechanism by which bacteria create and follow trails will provide unprecedented ability to manipulate the structures they collectively produce [74].

3.5.1 Attachment probability

Lacking A-motility, a likely mechanism of trail following in *P. aeruginosa* twitching motility is binding between T4P and EPS excreted by the bacteria (Fig. 3.5). Evidence for this mechanism has recently been published [85]. The composition of EPS in *P. aeruginosa* has been characterized to a reasonable degree and is composed of polysaccharides, alginates, and extracellular DNA (eDNA) [86]. Pili are

known to bind DNA, a process that has been associated with horizontal gene transfer, and genetic competence in biofilms [87]. Therefore, eDNA may be important in the trail following behavior observed in interstitial biofilm assays. However, the pilus tip binding site has not been shown to require specific molecular species or functional groups for binding, and therefore probably behaves as an unspecific adhesion site, with binding occurring via electrostatic attraction between the positively charged pilus tip and a negatively charged substrate [34, 84]. With that in mind, any negatively charged species within the EPS could act as an effective agent for trail following by biasing pilus attachment. The phenomenon of EPS trail following therefore requires two conditions. Firstly, the EPS must provide an effective anchoring site by adhering both to itself and to the surrounding, stationary environment. Secondly, the T4P affinity to the EPS must be substantially greater than its affinity to the bare substrate or native surrounding material.

3.5.2 Chemotaxis or chemokinesis?

This type of EPS trail following behavior has recently been referred to as chemotaxis [54]. This classification is not accurate. In chemotaxis, the displacement rate of cells is not altered by gradients of chemoattractants or repellents. Instead, these gradients guide the random motion of cells in a favorable direction through a bias to their random walk [88, 89]. In the case described here, EPS increases the movement rate of cells by increasing the probability of pilus binding. The cells respond to increased EPS levels by moving more quickly, even if EPS levels are increased uniformly and no concentration gradients exist. Such processes are referred to as *chemokinesis*. However, the term *chemokinesis* is generally reserved for situations in which no directional biasing occurs. In this case, spatial heterogeneity in a chemokinetic agent (the EPS) does lead to directional biasing. This occurs because local deposition, and very slow diffusion, of EPS can produce gradients on the spatial scale of individual

cells. This case is therefore a unique class of directional biasing that I will refer to as *micrograd*ient *chemokinesis* or 'micro-Ck'.

3.5.3 Movement bias

The influence of micro-Ck on trail following would depend enormously on the extension and retraction frequency of pili. This rate establishes how far a cell moves based on a single binding event, and how many possible binding events occur within a set period of time. This frequency could be viewed as a sampling rate of the space within the region in front of a cell over which its pili may be located. If this sampling rate is very fast compared to the movement rate of a cell, its direction will be effectively biased along a pre-existing trail. In the case of *P. aerugionsa* twitching motility, the sampling rate and movement rate are coupled because the pilus acts as both a sensory organ and a motility apparatus. In many other systems, such as human or ant trail networks [56, 59], the sensory and motility mechanisms are independent, allowing a very fast sampling frequency relative to the movement rate of the organism. In these cases, the ability to follow trails is facilitated by a complex information processing system that individual bacteria do not possess. Because the movement rate during single pilus retraction events has been documented, as well as the frequency at which pili extend and retract [34], it is possible to build a constrained numerical model of this process (see section 4.3).

3.5.4 EPS secretion and degradation

Implementation of the marker-based stigmergy mechanism described above within the framework of an individual-based model requires the definition of a function describing marker creation and marker degradation. However, it is difficult to define such functions based on experimental observations. In the present case, the markers consist of EPS material that has binding affinity to pili. Presumably, the function

describing the scaling of attachment probability as a function of EPS concentration would saturate to a maximum. An interpretation of the assumption that binding probability depends on the fraction of the surface covered in binding sites.

Degradation of the marker would be associated with the removal of effective attachment sites from the EPS. This could occur either due to decomposition of the polymer molecules themselves and the corresponding loss of structural integrity. On faster timescales, occlusion of attachment sites due to nonspecific binding to other materials, or neutralization by positively charged counterions could remove binding sites. Due to the free diffusion of dissolved counterions, neutralization processes would probably occur quickly compared to all other relevant timescales (including the rate of excretion), and would be important when defining the maximum binding probability. Occlusion by particulates and decomposition, however, would presumably occur slowly relative to the EPS excretion rate and would therefore define the time dependence of binding probability associated with existing EPS deposits.

As discussed in section 2.2, degradation of traces is an essential feature of stigmergic systems, as pointed out by Heylighen [18, 19]. We therefore expect the timescales of deposition, degradation, and individual response to trails to play important roles in collective pattern formation.

3.6 Sematectonic stigmergy

In addition to the marker-based stigmergy mechanism described in the previous section, Gloag *et al.* suggested the passive (or 'unintentional') modification of surface topography during cell movement could facilitate trail following [Fig. 3.6(a)] [45–47, 58]. Such processes have been defined as *sematectonic* stigmergy [18]. Even early observations show that surface motile bacteria do indeed create lasting grooves and trenches when moving across soft surfaces [52]. While this phenomenon appears to be ubiquitous for surface motile bacteria, whether or not these topographical

features play a decisive role in directing bacterial behavior remains to be directly investigated. Indeed, the process has been largely ignored in the existing literature, even though it may provide a useful means of manipulating bacterial behavior by altering the material properties of the interstitial environment [74].

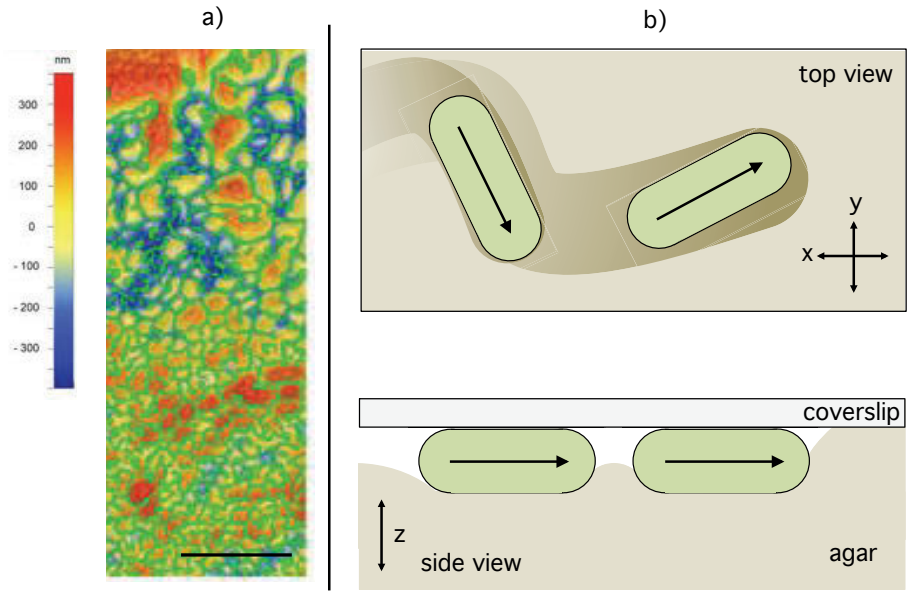

FIGURE 3.6: Bacteria in an interstitial environment locally deform the substratum. (a) A phase contrast image of an interstitial biofilm (green), overlaid on an optical topographical profile of the agar surface over which it moved (scale bar represents 100 μm). This figure was copied and adapted from Gloag *et al.* [46]). (b) Schematic representation of the substratum deformation process. If the rate at which deformations vanish is slower than the rate at which bacteria move, these deformations persist as trails that direct the movement of bacteria arriving later.

3.6.1 Topographical gradients

Here, we model substratum deformation as the deposition of a stigmergic trace representing the surface topography [Fig. 3.6(b)]. Deformation of surface topography acts on cells by changing their movement direction and velocity through the application of force down the topographical gradient.

3.6.2 Deformation and restitution

For this sematectonic process of 'furrowing', the deposition rate of the stigmergic signal corresponds to the time required for a cell to physically modify the shape of the surface with an applied force. In the interstitial space, the "degradation" rate of the trace would correspond to the rate at which capillary action between the two apposed surfaces causes restitution of the deformation to its initial state. The timescales associated with sematectonic stigmergy are therefore controlled by the composition of the material comprising the medium through which the bacteria move. For a hydrogel material such as agar or gellan gum, there are several important preparation parameters [90, 91]:

- concentration of monomer
- concentration of stabilizing cations (e.g., Mg^{2+}, Na^{+})
- curing time
- hydration level of the hydrogel

While the monomer and cation concentrations and curing time can be explicitly and precisely controlled during culture medium preparation, the hydration level depends on the temperature and humidity during curing of the hydrogel, and the humidity of the ambient environment during culture. Hydration level is therefore likely to be the most difficult parameter to control in practice.

The simple implementation of the furrowing process in the present model does not explicitly include terms for these different experimental parameters, and can therefore be considered phenomenological on this level of detail. However, the scaling functions determining the time dependence of furrow creation and degradation, as well as the coefficients defining the strength of the signal do correspond to physical processes that could be studied in isolation as a function of these three different experimental variables.

3.7 Attractive forces

Particulate objects surrounded by fluid are likely to aggregate due to a number of possible mechanisms (electrostatic interactions, depletion attraction, ion bridging, etc.). Aggregation can be simulated the same way as stigmergy due to substratum deformation. This requires increasing the deposition and degradation rates of the stigmergic trace corresponding to deformation of the environment to the timescale of bacterial movement. By doing so I observed realistic short-range attraction between cells. However, a systematic inclusion of this phenomenon would require parametrization based on measurement of aggregation forces, and was outside the scope of the present work.

Biological attraction mechanisms exist as well. In the case of *P. aeruginosa*, cross-linking between bacteria due to attachment of pili between neighboring cells represents a reasonable, system specific process.

3.7.1 T4P Cross-linking

Binding of T4P between cells was implemented by allowing pili to bind to bacterial surfaces, and distributing the retraction force between the pole of the cell retracting its pilus and the attachment site on the other bacterium (Fig. 3.7). This process produces a stochastic, point-point attraction between cells, that can pull them together over relatively long distances compared to the physical mechanisms leading to generic particle aggregation.

3.8 Simulations

In the next chapter, I will present and discuss the results of simulations carried out using various combinations of the conceptual elements discussed above (summarized

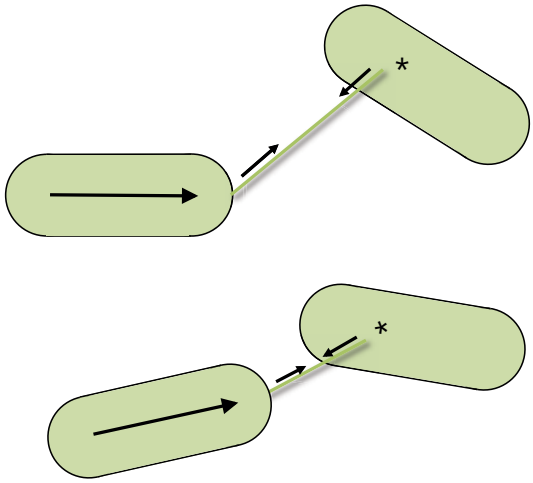

FIGURE 3.7: Point attractions can be caused by the retraction of T4P attached to the bodies of nearby cells.

in Figure 3.8). This will be accompanied by detailed descriptions of the equations and numerical implementation used for each of them.

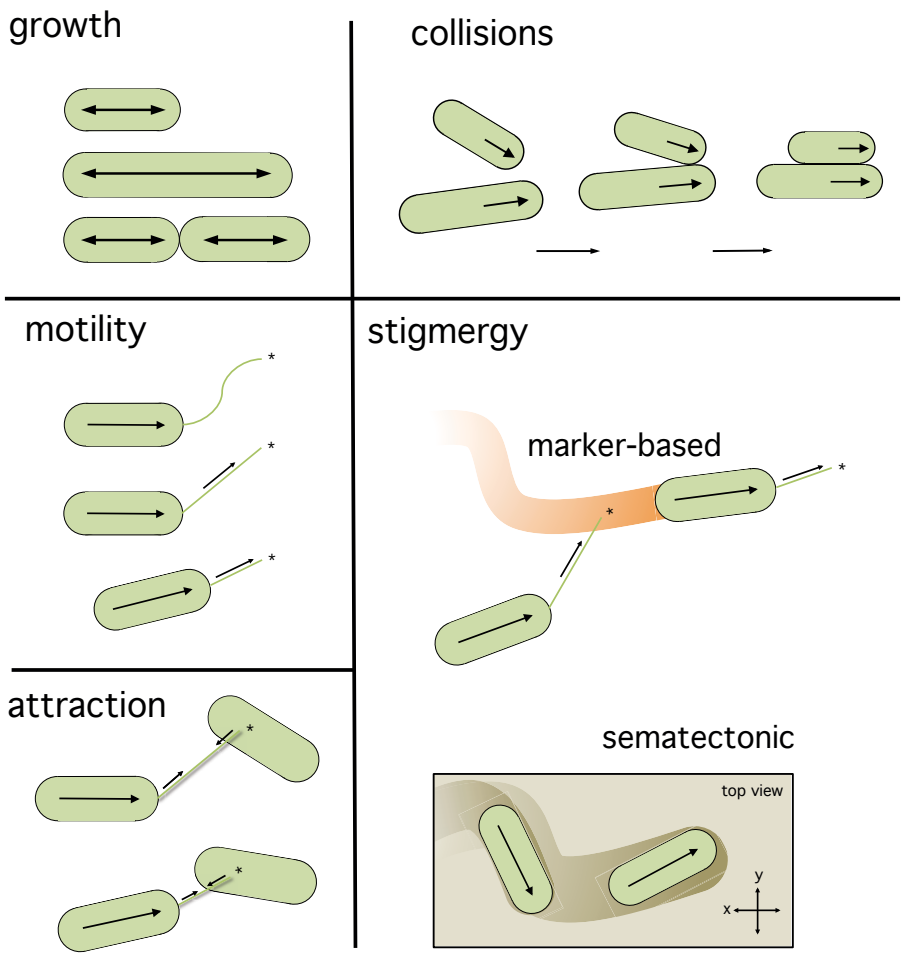

FIGURE 3.8: The main components of the phenomenological model developed here for *P. aeruginosa* twitching motility in the interstitial environment. Cells grow and divide, collide with each other, move around and pull on each other with T4P, and leave modifications in their environment due to EPS excretion (marker-based stigmergy) and physical deformation of the substratum (sematectonic stigmergy).

Chapter 4

The Steady State

4.1 Behavior of individuals

Before investigating the emergent properties of collectives, I will briefly explore and discuss the behavior of individuals within the model framework described in Chapter 3. The model is concerned with the description of microbial motility on surfaces. In accordance with that priority, I will describe the mathematical model of individual movement and its numerical implementation, recap the parameters that can affect individual motility, and proceed to explore the effects of those parameters and the associated dependence of displacement with time.

This section is concerned with understanding how the free parameters affecting movement alter the mean behavior of individuals. I will ignore stigmergy in this investigation of individual behavior as its effects on the individual are distinct from its effects on collectives [55]. I will show that the physical model and behavioral rules discussed in section 3.4 define an average displacement rate that on sufficiently long time scales behaves according to regular diffusion ($\langle \Delta x \rangle = \sqrt{Dt}$, where D is the translational diffusion constant). Therefore, ignoring stigmergy, and the interactions

between bacteria, each individual bacterium can be viewed as a particle of a diffusing substance.

4.1.1 Movement without stigmergy

Motility, as described in section 3.4, occurs due to the stochastic extension, binding, and retraction of pili. This 'twitching rod' model of surface motility is represented schematically in Figure 4.1. There are a number of parameters in this model implementation that affect motility behavior, some of which can be estimated based on pubilshed observations. Where possible, we derive these parameters from the results given in Skerker and Berg [34], and will make a note of these when they appear in the following description. The analysis to follow will investigate those parameters which remain unconstrained.

The retraction duration can be determined by two possible events, the random unbinding of the pilus tip, or the complete retraction of the pilus (in which case the leading cell pole reaches the binding site). Therefore the translational movement Δx_{ret} resulting from a single retraction event is given by:

$$\Delta x_{ret} = \min \left[\frac{F_{ret}}{\mu l} t_{ret} \, , d_{ret} \right] \tag{4.1}$$

Where $F_{ret} = 1.5$ is the retraction force, l is the cell length, $\mu = 1$ is the (constant) friction coefficient per unit length, t_{ret} is the retraction duration, and d_{ret} is the pilus length at the time of binding. The unobstructed movement rate reported by Skerker and Berg was, 0.1 - 0.5 μm/s, in excursions of 1 - 6 μm [34]. In the present model, the retraction force and friction are constant, so that differences in cell length are the only sources of variation in movement rate. This result of our physical model has not been tested, but could be investigated in further experiments on single-cell movement. In our model of cell growth, the minimum cell length is 3 μm, the average

is 5 μm, and the maximum is 7 μm, which correspond to movement rates of 0.5, 0.3, and ~ 0.21 μm/s, respectively. For this investigation of individual behavior, the length is kept uniform at $l = 5$ μm, the average value.

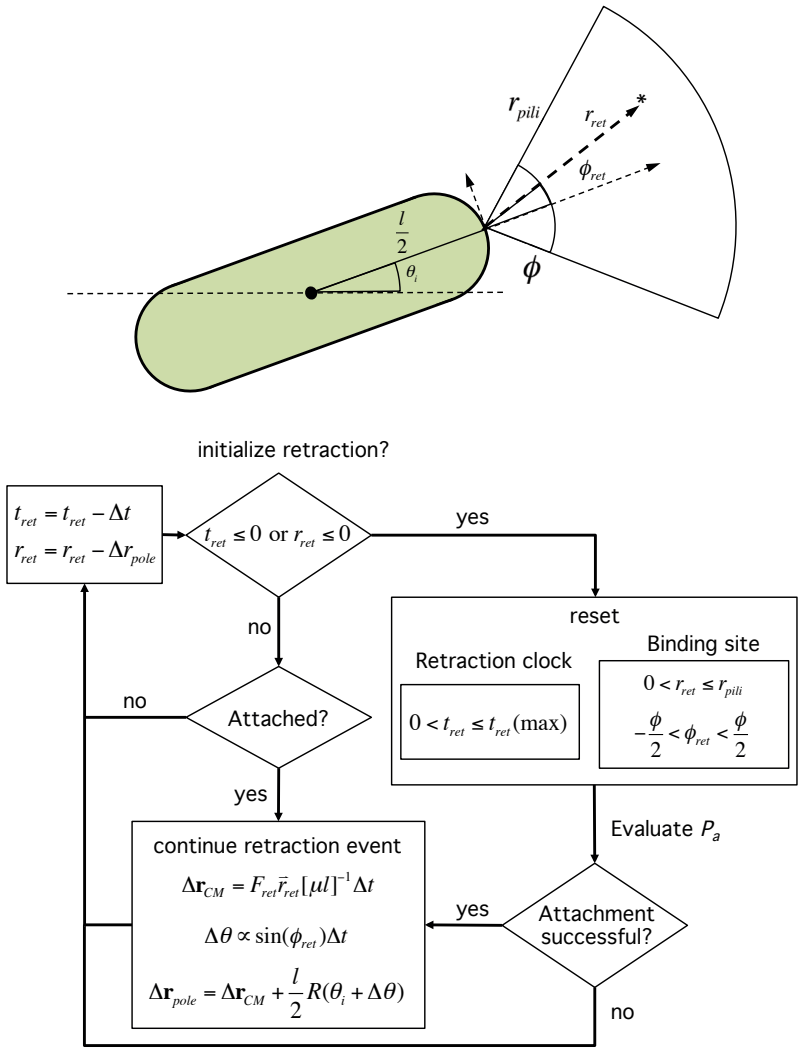

FIGURE 4.1: Schematic of T4P retraction process and the associated workflow.

At the initiation of a retraction event the retraction duration t_{ret} is randomly assigned in a uniform interval so that $0 < t_{ret} \leq 2\langle t_{ret} \rangle$ where we set the maximum retraction duration $2\langle t_{ret} \rangle = 10$ s. The retraction duration corresponds to the time between binding and stochastic unbinding and gives maximum displacements of 5, 3, and 2.1 μm for the minimum, average, and maximum cell lengths respectively. These values all fall within the range observed by Skerker and Berg [34], though the

physical cause of the variation has not been experimentally attributed to cell length, as it is in this model.

The delay time between binding attempts can be given either by the retraction duration t_{ret} or by the time required for complete retraction of pili, determined by the pilus extension distance d_{ret}. With each attempt, the latter is assigned so that $0 < d_{ret} \leq r_{pili}$, where the maximum pilus range r_{pili} is somewhat arbitrary, but should be on the order of the cell length. In these simulations $r_{pili} = 3$ μm, which is reasonable based on inspection of the fluorescence images in Skerker and Berg (as discussed in section 3.4) [34]. This value of r_{pili} acts as an upper limit on the displacement from a single twitching event. This value is conservative compared to the maximum reported movement distance (6 μm). However, Skerker and Berg only measured 11 events, and the chosen value constrains events in the model to within the reported time and distance scales [34]. The results reported here should be robust to higher values of r_{pili} because in general the movement distance will be regulated by random unbinding of pili according to Eqn. 4.1.

In two dimensions, diffusive motion requires rotational diffusion of the cell's velocity vector. In the present model the dynamics are assumed to be overdamped and Brownian motion negligible. Rotational diffusion is therefore a result of the angular range ϕ over which a pilus may reach, producing movement vectors that change the orientation of the cell's long axis. Without ϕ, motility would be unidirectional and displacement would be trivially determined by the average velocity (the retraction velocity multiplied by the attachment probability).

Along with the retraction distance d_{ret} and duration t_{ret}, a random retraction angle $\phi_{ret}(t)$ is selected within ϕ so that $-\frac{\phi}{2} \leq \phi_{ret}(t = 0) \leq \frac{\phi}{2}$ (here, $t = 0$ corresponds to the point in time at which retraction is initialized). The attachment probability P_a is then evaluated at the binding site defined by $\phi_{ret}(0)$ and d_{ret}. If binding occurs, force is applied to the cell pole during subsequent time steps for the duration of retraction. For $\phi_{ret} \neq 0$, a change in cell orientation occurs due to torque proportional to the

component of the retraction vector that is perpendicular to the cell's orientation and the distance from the cell pole to its center of mass:

$$\tau = F_{ret}\frac{l}{2}\sin(\phi_{ret})\,, \tag{4.2}$$

As the cell is pulled towards the binding site, ϕ_{ret} and the corresponding torque decrease. Therefore, the instantaneous rate of change in orientation during a single retraction event is not constant in time and is described as follows:

$$\frac{d\theta}{dt} = A\sin(\phi_{ret})\,, \tag{4.3}$$

where $A = 12F_{ret}\frac{l}{2}[\mu l^3]^{-1}$ is a constant describing the damping due to friction and the effect of cell length on torque applied by the retraction force [42].

If $\phi \leq \pi$ (the pili only attach to points in front of the cell's leading pole), the angular displacement rate decreases exponentially for the retraction duration as the cell's forward pole approaches the binding site. In general, the total angular displacement from a single retraction will be a function of the cell length, linear and radial pilus range, retraction force, and the retraction duration. In other words, if $\phi > 0$, the rotational diffusion rate will be a function of the amount of displacement per successful retraction. In this scenario, t_{ret} stands out as a significant parameter because it is under the biological control of individual cells and can dramatically alter the diffusion rate.

To summarize, the average movement behavior of individual bacteria is determined by the following parameters:

- attachment probability, P_a

- average binding time, $\langle t_{ret} \rangle$
- linear pilus range, r_{pil}
- radial pilus range, ϕ
- retraction force, F_{ret}
- friction per unit length, μ
- cell length, l

Because the attachment probability is an exogenous parameter, determined by the environment and not by bacterial physiology, I will proceed by investigating its effect on the displacement rate of individual bacteria. To reiterate, the parameters affecting individual movement were estimated by examining the fluorescence images, unobstructed movement rate during pilus retraction, and retraction distance documented in Skerker and Berg [34] and our own observations of average cell length [Fig. 3.3(c)]. These constrained parameters will be held constant in the following analysis.

The bacterial movement model investigated in the following section does not include stochastic polarity reversals as discussed in section 3.4.3. Because the cell polarity remains fixed, this model represents *polar* movement. After investigating the effects of the unconstrained parameter P_a on polar movement, I will present a systematic investigation of *apolar* movement (with polarity reversals enabled) since there are no data in the existing literature that allow precise estimation of the polarity reversal period, which defines apolar movement in the present model.

4.1.2 Polar movement

The translational diffusion rate D is determined by the fixed parameters and the attachment probability only. Due to random changes in direction there will be a

time τ_θ, the angular decoherence time, when on average, the initial orientation has randomized. τ_θ can be estimated by initializing k replicates with the same initial orientation at t_0 and comparing the entropy $H_\theta(t)$ of the distribution of angles at time $t = t_0 + \Delta t$ with the expected entropy of a uniform distribution H_u. This value of merit $\Delta H(t)$ is given by

$$\Delta H(t) = 1 - \frac{H_\theta(t)}{H_u}\,, \tag{4.4}$$

where $H_u = \ln(n)$, the log of the number of bins n used to represent the distribution of k orientations. Because of the finite nature of the sample at time t, ΔH will stabilize to a nonzero value that depends on the number of bins and the number of replicates:

$$\Delta H_{min}(n,k) = \frac{n}{k}[Bn^b + c]\,, \tag{4.5}$$

where $B \approx 0.37$, $b \approx -0.38$, and $c \approx 0.045$ were determined empirically from finite samples of uniform distributions evaluated for different values of k and n (see Appendix A.1.2). This numerical estimate of ΔH_{min} is valid if $k \gg n$. By applying a satisfaction criterion such as $\Delta H(\tau_\theta) \equiv 1.05\Delta H_{min}$, τ_θ can be estimated for a given set of parameters.

For polar movement, the scaling of displacement with time becomes diffusive after τ_θ is exceeded [Fig. 4.2(a)]. By fitting $\langle \Delta x \rangle = \sqrt{Dt}$ for $t > \tau_\theta$, a diffusion coefficient D can be assigned for different values of the attachment probability. The value of D increases linearly with attachment probability [Fig. 4.2(b)], according to $D = D_{max}P_a$ where $D_{max} = 28.5 \pm 0.1\ \mu\text{m}^2/s$. When $P_a = 1$, diffusion is as fast as it can be for a given biological condition as defined by the other parameters affecting movement rate. Because more frequent attachment means more frequent changes in direction, τ_θ decreases with increasing P_a and scales as $\tau_\theta = [\tau_{min}][P_a]^{-1}$ where $\tau_{min} = 765 \pm 38\ s$ is the orientational decoherence time when $P_a = 1$ [Fig. 4.2(c)]. The

maximum diffusion rate D_{max} and minimum decoherence time τ_{min} are determined by the fixed parameters that describe bacterial motility.

To summarize, even though increased P_a makes the bacteria move faster on average, it also increases the rate at which their movement direction randomizes, resulting in diffusive motion over much shorter timescales. Ignoring polarity reversals and interactions between cells, the attachment probability changes the diffusion rate of bacteria, but does not change the nature of the resulting configuration. In this simple case, τ_θ defines how long it takes for anisotropic initial conditions to become isotropic, and D defines the expansion rate of the isotropic state. This result is not surprising, but confirms that the motility model behaves as expected.

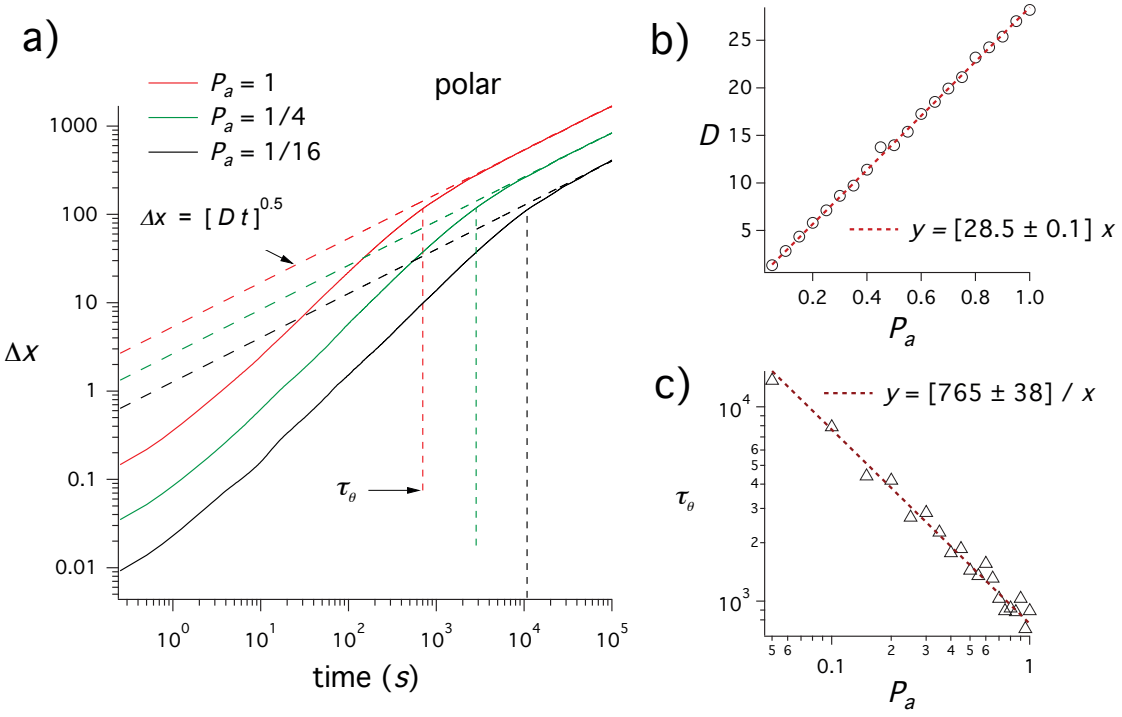

FIGURE 4.2: With polarity reversals disabled, diffusive motion begins when the angular randomization time (τ_θ) is exeeded. Plots of displacement as a function of time (a), demonstrate how movement evolves from directed ($t < \tau_\theta$), to diffusive ($t > \tau_\theta$). The corresponding translational diffusion coefficient D increases linearly with attachment probability P_a (b). The angular randomization time scales as the inverse of attachment probability (c).

4.1.3 Apolar movement

As discussed in the previous chapter, cells stochastically reverse polarity which produces diffusive motion in 1D. The average reversal period T_{rev} determines the frequency of polarity reversal events. To implement these stochastic reversals in movement direction, a reversal time t_{rev} is initially assigned from a uniform distribution with mean T_{rev} so that $0 \leq t_{rev} \leq 2T_{rev}$. As the simulation proceeds, a countdown occurs from t_{rev}, initiating a polarity reversal (adding $\pm\ \pi$ to the cell's orientation) upon reaching 0, at which point a new value of t_{rev} is assigned.

Allowing cells to reverse direction dramatically alters both the translational and angluar diffusion characteristics of the motility behavior that is controlled only by the attachment probability in the case of polar movement. While the attachment probability is an environmental parameter that will be determined by the material and chemical properties of the substance comprising the substratum, the reversal frequency is likely to be under the biological control of the bacteria [33, 64]. Therefore, it is of interest to investigate the interplay between these two effects by systematically varying both.

As in the polar case, a diffusion constant can be defined for each combination of T_{rev} and P_a. However, there are now two time scales that determine the onset time of diffusive motion t_D: the angular randomization time for the polar case τ_θ, and the maximum reversal period $2T_{rev}$.

Three types of behavior are possible in the apolar case [Fig. 4.3(a)]:

- type 1: if $2T_{rev} \lesssim \tau_\theta$ diffusion is determined only by direction reversals and $t_D \approx 2T_{rev}$
- type 2: if $T_{rev} \lesssim \tau_\theta \lesssim 2T_{rev}$, diffusion is determined by a combination of direction reversals and angular diffusion and $2T_{rev} \lesssim t_D \lesssim \tau_\theta$
- type 3: if $T_{rev} \gtrsim \tau_\theta$, apolar diffusion is identical to the polar case and $t_D \approx \tau_\theta$

The above three cases pertain to the timescale associated with the transition from uniform initial conditions (all k replicates have the same initial position, length, and orientation), to a state in which orientations are uniformly random, positions are normally distributed in 2D around the center of mass, and diffusive movement can be described by the translational diffusion constant D.

There are two scaling regimes for D as a function of T_{rev} that are again determined by the two timescales T_{rev} and τ_θ [Fig. 4.3(b)]:

- regime 1: $T_{rev} \lesssim \tau_\theta$, D increases approximately linearly with T_{rev}
- regime 2: $T_{rev} \gtrsim \tau_\theta$, D saturates to approach $D(\tau_\theta)$, the value corresponding to the polar case

This inequality determines the scaling of D with P_a as well [Fig. 4.3(c)]. In regime 1, $D \propto {P_a}^2$, while in regime 2, D increases linearly with P_a just as it does in the polar case [Fig. 4.2(b)].

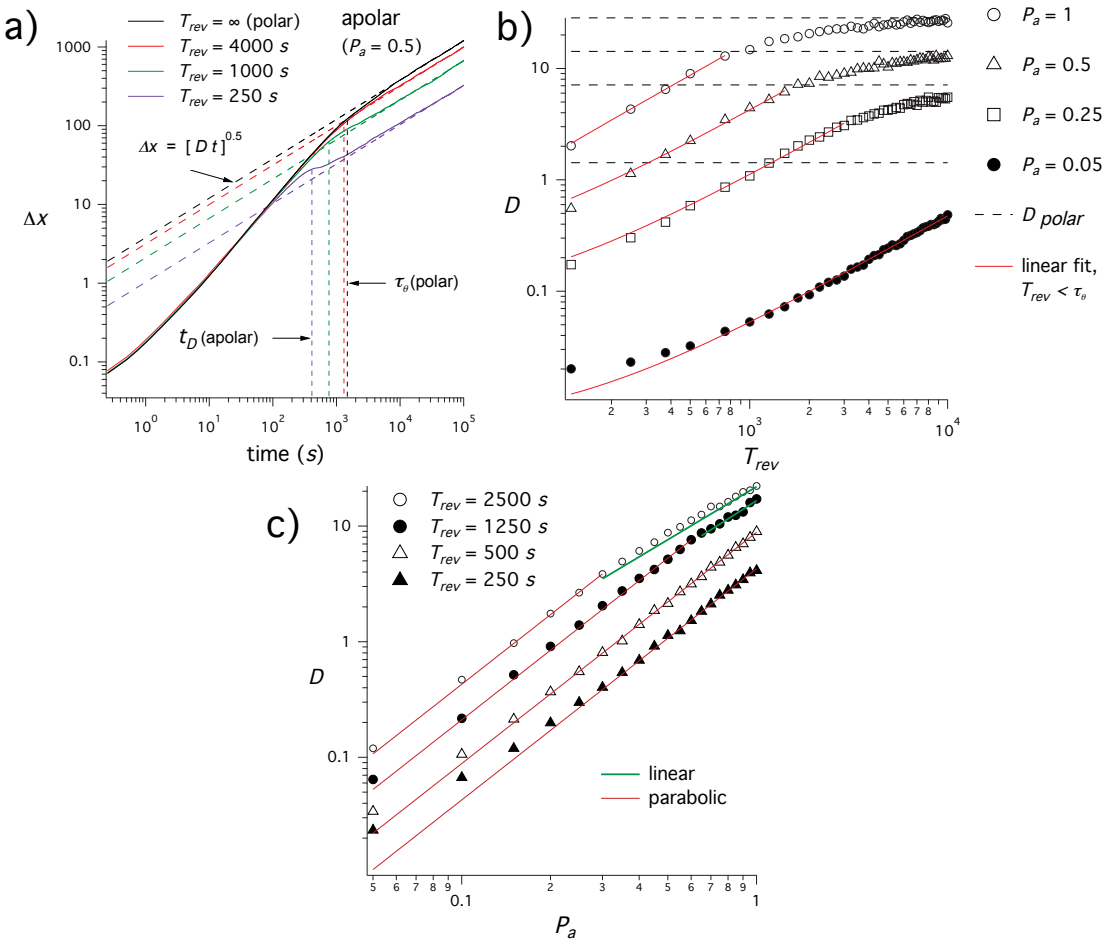

FIGURE 4.3: Direction reversals alter diffusive behavior. (a) Plots of displacement as a function of time for different values of T_{rev}, and fixed attachment probability ($P_a = 0.5$). (b) Plots of diffusion coefficient D as a function of T_{rev} for different values of P_a show linear behavior when $T_{rev} < \tau_\theta$ (red) and saturation for $T_{rev} > \tau_\theta$. (c) Plots of D as a function of P_a show parabolic (red) and linear (green) scaling regimes.

The results in this section are summarized by a 2D plot of D as a function of T_{rev} and P_a as shown in Figure 4.4(a). The contour provided by the inequality discussed above is superimposed on the plot and can be matched if the apolar diffusion constants are normalized to the polar ones determined for the corresponding value of P_a [Fig. 4.2(b)]. This illustrates the two different scaling regimes discussed above and emphasizes the saturation of D as a function of T_{rev}.

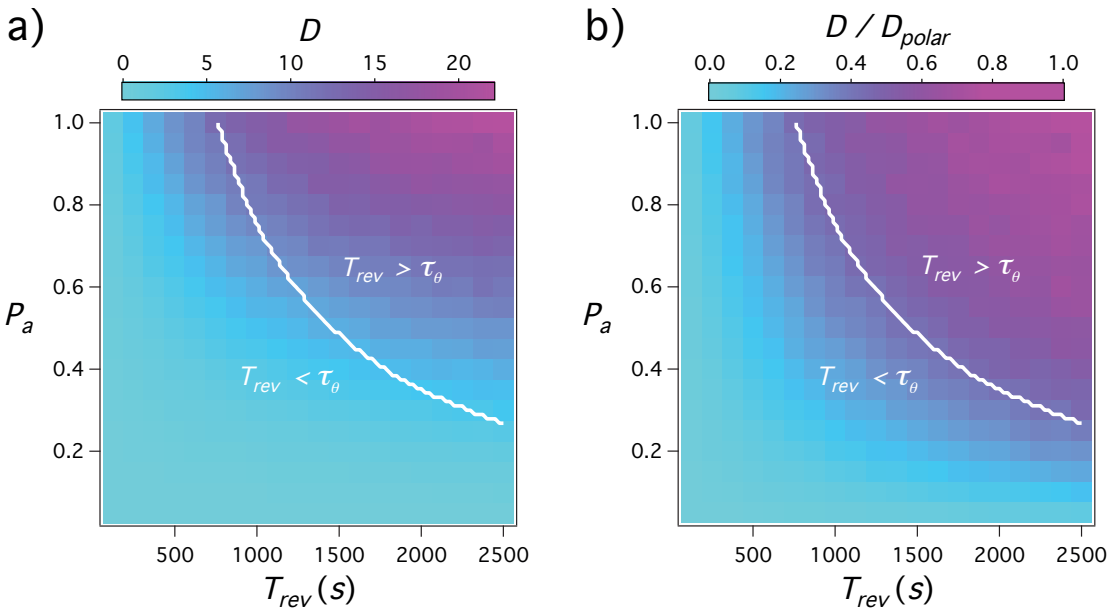

FIGURE 4.4: 2D maps of D as a function of P_a and T_{rev} demonstrate two distinct regimes, separated by a line representing the set of parameters for which $T_{rev} = \tau_\theta$. By normalizing each row to the corresponding diffusion coefficient expected for the polar case $D_{polar}(P_a)$, the scaling trend matches the contour set by the transition line.

This saturation effect is potentially significant with respect to the possibility of biological control over polarity reversals as a means of biasing movement due to chemical stimulus (chemotaxis). Because of saturation, the angular randomization time provides a quantitative estimate of the time scale over which such biasing would have an effect on the net movement of bacteria.

If chemotaxis was determined by adaptive temporal sampling of the chemical environment as it is in swimming *E. coli* [88, 89], adaptation of the chemotaxis mechanism to environments with different pilus-surface binding affinity would require the equilibrium reversal period to decrease as the polar movement rate increases. Without such an adaptation process, chemotaxis may not be robust to different surface characteristics. These results support the hypothesis that robust chemotaxis in *P. aeruginosa* twitching motility may be facilitated by spatial (rather than temporal) sampling of weak chemical gradients along the length of individual cells.

In addition to chemotactic control over reversal frequency, preferential pilus binding to surface-bound substances appears as a plausible mechanism of motility bias as discussed in section 3.5. Section 4.2 discusses my investigation into the phenomenon of *microgradient chemokinesis* (micro-Ck, see section 3.5.2) as a potential mechanism of marker-based stigmergy.

Before implementing stigmergy, repulsive cell-cell interactions and cross-linking through pilus binding will be included in the model framework. The inclusion of interactions between cells allows the simulation of collective behaviors. In the next section, I will compare the collective behavior of the 'twitching rod' model to results from the existing literature on models of self-driven rods.

4.2 Collective behavior of twitching rods

4.2.1 Introduction

In this section I will investigate the collective behavior resulting from extending the model of individual movement mechanics introduced in the previous section [Fig. 4.5(a)] to include repulsive interactions between motile rods [Fig. 4.5(b)], and attractive forces mediated by T4P [Fig. 4.5(c), see section 3.7.1]. Supplemental material for this section including links to the source code can be found in Appendix A.2.

The intention here is to compare this specific model to those investigated in other, similar work. Specifically, the results of Peruani *et al.* [38], and Balagam and Igoshin [53] are relevant to the present model which is a direct extension of their research. These previous investigations demonstrated that collections of motile rods moving in polar, deterministic paths (no orientational noise or direction reversal) will exhibit nonequilibrium clustering due to collisions between rods that tend to align their orientations. Peruani *et al.* found that this general trend holds if Brownian motion is considered as a source of orientational noise [38]. However, Balagam and Igoshin found that nonequilibrium clustering vanished upon the inclusion of spontaneous polarity reversals [53].

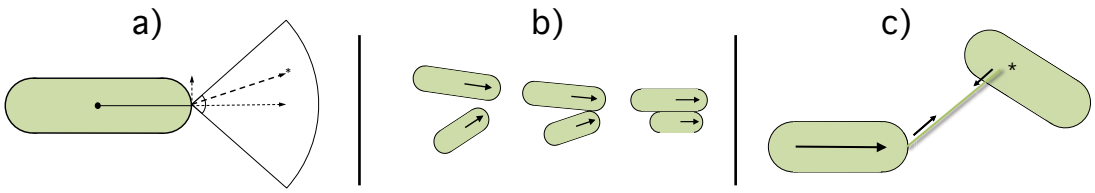

FIGURE 4.5: (a) The motility mechanism in this model is the same as in the previous section, a numerical approximation of twitching motility. (b) Repulsive interactions between motile rods leads to alignment of physical orientation and velocity direction. (c) Attractive forces mediated by T4P may occur if the binding site is on the body of another bacterium.

While the results presented below confirm that polarity reversals prevent clustering and collective motion, I will show that Peruani *et al.*'s result [38] is sensitive to cell velocity and does not hold for the unobstructed movement rate reported by Skerker and Berg [34]. Additionally, discontinuous movement due to stochastic pilus binding prevents the transition to clustering for the polar case. For these reasons, the results in this section indicate that alignment due to collisions is insufficient to produce nonequilibrium clustering in *P. aeruginosa*. This minimal description therefore cannot describe the nonequilibrium clustering behavior and morphogenesis observed in the species.

In the reports mentioned above, the aspect ratio of the rods was fixed for each simulation. It was an important control parameter, which dictated the density of bacteria necessary for the onset of nonequilibrium clustering. Here, we investigate a mixed aspect ratio to more accurately represent what would be found experimentally in bacterial colonies composed of growing, dividing cells. To clarify, the length of each individual cell is fixed in the present investigation, but each bacterium is assigned their length at random from a uniform distribution $[l_{min}, l_{max}]$ where $l_{min} = 3$ μm and $l_{max} = 7$ μm are the centerline lengths of each cell which are shaped as rectangles with hemispherical caps (2D spherocylinders). Because of the hemispherical caps, the total length of each cell is $l + w$ which also defines the aspect ratio κ since each cell has unit width.

In addition to the distributed aspect ratio, there are two slight differences between the model used in this section and the model used in the previous section to investigate individual behavior. The first is that here, reversal periods are drawn from a Gaussian distribution (rather than a uniform distribution). The second is that the delay time between pilus retractions is given only by the binding duration t_{ret}, which means that a cell will remain anchored to the attachment site of its pilus if full retraction occurs before unbinding. The change in the reversal period distribution was made because this model is not just concerned with global, average behavior and therefore a more defined distribution of reversal periods is more appropriate.

The difference in retraction duration is necessary because, due to repulsive cell-cell interactions, the distance between the cell pole and the binding site is not only a function of pilus retraction and therefore approach between the cell pole and the binding site does not necessarily correspond to the disappearance of the pilus.

The other interaction effect that is implemented here is the attractive effect of pilus cross-linking between cell surfaces. This is taken into account here, with the probability of pilus binding to cell surfaces held constant ($P_{pp} = 0.25$), and evaluated if the pilus binding site is located in the coverage are of another cell. Retraction then pulls the cells towards each other, with the retraction force producing translational and rotational movement of both cells.

The results of this section will be useful when interpreting the behavior of simulations that include more complex rule sets describing stigmergy due to the interaction between the bacteria and their environment, and EPS excretion.

4.2.2 Physical properties of individuals

Note: this section is adapted from the model description in the manuscript entitled *Emergent pattern formation in an interstitial biofilm* by Zachreson *et al.* [92, 93]

Because cell-cell interactions are taken into account here, the model must explicitly describe individual geometry and the potentials that determine the forces produced by collisions between cells. This section gives the details of the physical description of individuals and the interaction scheme implemented to resolve collisions.

The physical interaction scheme is similar to that used in Ref. [42, 43]. Friction is uniform in space, so that damping does not vary along the length of a rod-shaped cell. Translational and angular velocities that arise from physical interactions therefore depend on cell length and a constant friction coefficient per unit length μ, and are proportional to the applied forces and torques, respectively.

In this model of collective behavior, translational motion is calculated as in the previous section using:

$$\frac{dx_i}{dt} = \frac{\vec{F}_i}{\mu l_i}\,, \tag{4.6}$$

here, $\vec{F}_i$ is the sum of forces generated by motility $\vec{F}_p$ (here, F_p includes the forces applied to cell i by the pili of neighboring cells) and cell-cell interactions $\vec{F}_{ij}$ so that $\vec{F}_i = \vec{F}_p + \sum_j \vec{F}_{ij}$.

Similarly, angular velocity is given by:

$$\frac{d\theta_i}{dt} = \frac{12\tau_i}{\mu l_i^3}\,, \tag{4.7}$$

in which $\tau_i = \tau_p + \sum_j \tau_{ij}$ is the net torque on cell i due to motility τ_p, and interaction forces τ_{ij}. See A.2.1 for a detailed description of the numerical implementation of cell-cell repulsion.

In addition to repulsive contact forces, the model of collective behavior includes attractive forces mediated by pili. The latter rule is implemented by defining a constant attachment probability $P_{pp} = 0.25$ that is evaluated every time an attachment point is selected that is located on the body of another cell. If attachment is successful, the retraction force produces attraction between the forward pole of the cell retracting its pilus, and the binding site on the cell to which it is attached.

4.2.3 Simulations

For general simulation details see Appendix A.2.2.

The simulation space is a 2D square area with side length $L = 240$ μm. Simulations ran for 5×10^5 s (sections 4.2.4 and 4.2.5), or 10×10^5 s (sections 4.2.6). In the sections to follow we assess collective behavior for 4 different attachment probabilities $P_a = [0.1, 0.3, 0.6, 1.0]$, and 6 different coverage fractions η = [0.05, 0.1, 0.15, 0.2,

0.25, 0.3], where $\eta = Na_oL^{-2}$ for a population of N bacteria of mixed length with average length $\langle l \rangle = [l_{max} + l_{min}]/2$ for an average area per cell $a_o = \langle l \rangle w + \pi(w/2)^2$ confined to area L^2. Coverage fractions are used in this section rather than cell density to facilitate direct comparison to the paper by Peruani *et al.* [38].

We proceed to investigate whether or not these conditions lead to emergent nonequilibrium density fluctuations or cluster formation.

4.2.4 Density fluctuations

A fundamental characteristic of any system of cells distributed in space is the density distribution. A defining characteristic of nonequilibrium structures is spatial heterogeneity in this property. [See Appendix A.2.3 for more background and on density and number fluctuations, and details about how they were computed for this work.]

Plots of time-averaged spatial density fluctuations [Fig. 4.6(a) and 4.6(b)] for each of the conditions investigated reveal some interesting characteristics. When the coverage fraction is low ($\eta \leq 0.05$), all attachment probabilities give equilibrium density fluctuations. In this condition, interactions between cells occur infrequently enough that the system behaves approximately as a non-interacting group of independently diffusing particles.

As coverage increases, all attachment probabilities in both apolar and polar modes show nonequilibrium behavior as a function of coverage fraction except for one: when movement is apolar and attachment probability is low ($P_a = 0.1$), the density fluctuations increase according to the square root of the average local population divided by a_{sub}, as expected for systems of non-interacting particles at equilibrium [Figs. 4.6(a) and 4.6(b) red dashed lines]. This is not surprising, since interactions produce nonequilibrium behavior, and the condition of slow movement combined with the tendency to reverse direction can reasonably be assumed to result in fewer

interactions. Indeed, for the case of apolar movement ($T_{rev} = 1000 \pm 200\ s$), the magnitude of density fluctuations systematically increases with attachment probability [Fig. 4.6(b)].

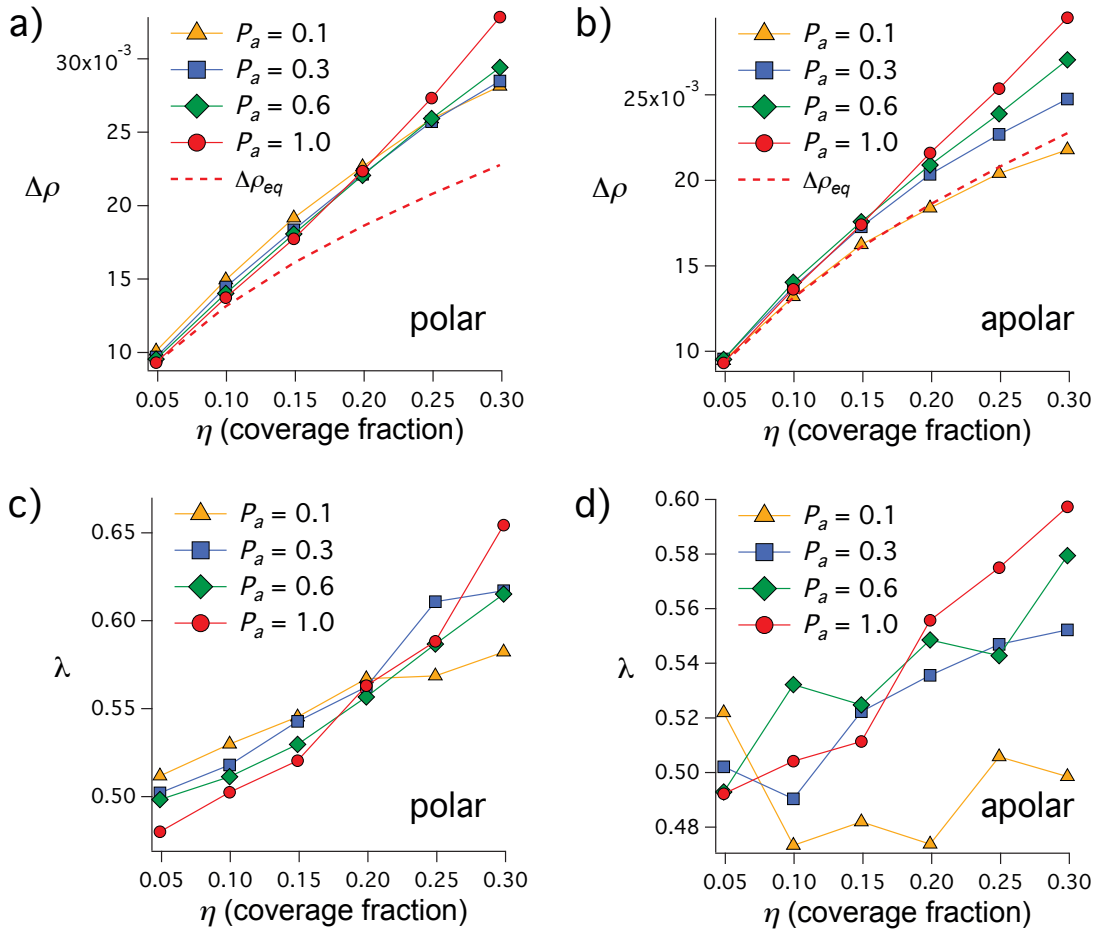

FIGURE 4.6: Steady-state density fluctuations (a, b), and number fluctuation scaling exponents (c, d) as a function of coverage fraction η, and attachment probability P_a for polar (a, c) and apolar (b, d) movement. In most cases, the density fluctuations (a, b) are higher than the equilibrium value for the corresponding coverage fraction (dashed red line) which is matched only in the case where $P = 0.1$ and movement is apolar. Scaling coefficients λ (c, d) describing the dependence of number fluctuations on subregion area indicate that the nonequilibrium behavior demonstrated in (a) and (b) is independent of the choice of subregion dimension used for calculating density fluctuations, and is therefore scale independent up to the system size $L = 240\ \mu$m.

In the case of polar motility, density fluctuations are larger than those observed in the corresponding apolar simulations and there is more similarity in density fluctuations

vs. coverage fraction for the various values of attachment probability investigated. On careful inspection, it appears that there is an inversion in the trend as a function of P_a as η increases [Figs.4.6(a) and 4.6(c)]. For low coverage fractions ($\eta < 0.2$), lower attachment probability corresponds to higher density and number fluctuations, possibly due to the attractive effects mediated by pili when the probability of pilus attachment to the cell body (P_{pp}) is comparable to, or greater than P_a. This trend reverses for ($\eta > 0.2$) with faster, more continuous movement (higher P_a) giving much greater density fluctuations than slower, discontinuous movement at the same coverage fraction.

The increase in density fluctuations at higher values of P_a for both polar and apolar cases is likely due to the effect of attachment probability on movement continuity. When movement is continuous ($P_a = 1$), cells that undergo collisions align their movement directions and proceed to move together, remaining in close proximity and constituting a cluster. If movement is stochastic and discontinuous, collisions still cause orientational alignment, but clustering is hindered because the movement rates of the cells fluctuate, causing them to separate in space after colliding.

To investigate the scale dependence of these density variations, it is instructive to examine the cell number fluctuations as a function of subspace area. The number fluctuation exponent λ quantifies how spatial fluctuations in particle number scale with the size of the subspace area used to count them. See Appendix A.2.3 for details of how λ is calculated.

Here, plots of λ vs. η [Figs. 4.6(c) and 4.6(d)] confirm that the trends demonstrated in Figures 4.6(a) and 4.6(b) are scale-independent up to the system size investigated here.

4.2.5 Clustering

Because nonequilibrium density fluctuations were observed for all cases excluding the apolar condition with low attachment probability [Fig. 4.6(b)], I examined whether these density fluctuations correspond to anomalous cluster size distributions (CSD) such as those observed by Peruani *et al.* [38]. See Appendix A.2.4 for a description of how CSD calculations were performed.

All simulations had reached the steady state during the final 1×10^4 s so I used that interval ($t \in [4 \times 10^4,\ 5 \times 10^4]$ s) to evaluate cluster statistics representing the steady-state condition. The steady-state cluster size distributions for the polar and apolar cases are shown in Figures 4.7(a) and 4.7(b) respectively.

Surprisingly, none of these distributions demonstrate the bimodal or power-law characteristics observed by Peruani *et al.* for deterministically moving rods [38]. Instead, the CSD decays exponentially even though the average aspect ratio used here is well above the predicted critical aspect ratio required to produce collective behavior for coverage fractions of $\eta = 0.3$. Indeed, the average aspect ratio in this work is 6, while the critical aspect ratio giving nonequilibrium clustering for the same coverage fraction in the model by Peruani *et al.*. is $\kappa_c \approx 1.46/0.3 - 1 = 3.87$, which is actually smaller than the minimum aspect ratio in our length distribution. This indicates that the movement mechanism we employ negates the transition to nonequilibrium clustering as observed for continuously driven rods.

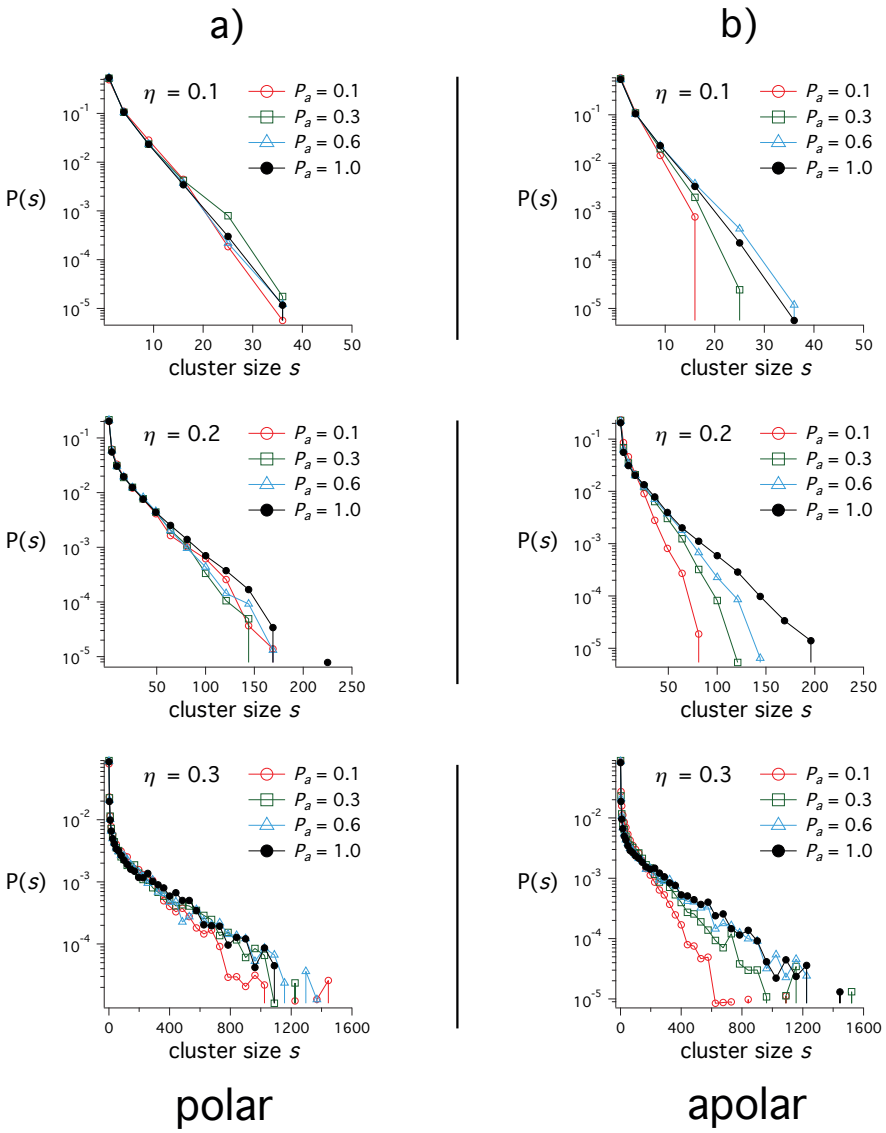

FIGURE 4.7: CSD plots corresponding to (a) polar, and (b) apolar motility. The probability $P(s)$ of finding a randomly selected cell in a cluster of size s is plotted for the indicated values of attachment probability (P_a) and coverage fraction (η). When movement is polar, $P(s)$ is independent of P_a. When movement is apolar, cluster sizes increase with P_a to approach the polar CSD for the same η value.

Given that the movement mechanism we have developed is based on real observations of bacterial motility, this result indicates that for bacteria moving discontinuously in 2D environments, the collective motion mechanism described by Peruani *et al.* [38] that is based solely on collisions between moving rods, is not an adequate explanation of observed collective motion phenomena in bacteria like *P. aeruginosa*

that move on surfaces using the extension and retraction of T4P, and do not employ continuous movement mechanisms such as the A-motility mechanism characterized for *M. xanthus*. In the next section, I will investigate which aspects of the motility behavior in the present model prevent bimodal clustering.

4.2.6 Robustness of the bimodal CSD

To investigate the robustness of bimodal clustering to the model parameters, I began by tuning the present model of bacterial twitching motility until the bimodal cluster size distribution was observed. The model of interest is a system of self-propelled rods with the following defining characteristics: continuous, polar, directed movement, uniform aspect ratio, and no attractive forces between cells. Additionally, in Peruani *et al.*'s published results [38, 39], the velocity of cells is approximately one order of magnitude less than the documented retraction speed [34]. The following adjustments mimic Peruani *et al.*'s model within the framework used here to simulate twitching motility:

- **polar movement:** direction reversals disabled
- **directed movement:** orientational uncertainty in the pilus retraction vector set to zero, ($\phi = 0$)
- **continuous movement:** pilus-surface attachment probability set to 1, ($P_a = 1$) so that movement never pauses
- **attractive forces disabled:** pilus-cell attachment probability set to 0, ($P_{pp} = 0$) so that no attractive forces occur
- **uniform aspect ratio:** cell length defined uniformly, and equal to the average of the distribution used previously, ($\kappa = 6$)
- **reduced velocity:** retraction force decreased to approximately match the individual movement rate used by Peruani *et al.* [38], ($F_{ret} = 0.15$).

These modifications indeed result in a bimodal cluster size distribution for values of κ and η corresponding to the bimodal phase (Fig. 4.8). The system size employed here is much larger than the one Peruani *et al.* used to demonstrate their result [38]. Therefore, the cluster statistics reported here are not identical to theirs, but still show bimodality. This is an encouraging result. It confirms that Peruani *et al.*'s findings are applicable to this biophysical model of cell-cell repulsion. It also shows that the qualitative trend is still observable when the system size is increased.

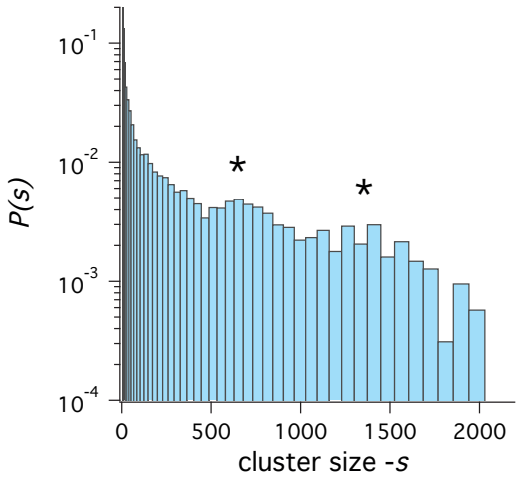

FIGURE 4.8: Cluster size distribution for the self-propelled rod model tuned to reproduce the bimodality observed in Peruani *et al.* [38]. Nonequilibrium clustering modes are marked with asterisks (*).

I tested the robustness of this result to each behavioral element distinguishing the 'twitching rod' model from the continuous self-propelled rod model. The results (Fig. 4.9) indicate that apolarity, increased velocity, and discontinuity in movement are responsible for the lack of bimodality in the CSD data for the twitching rod model [Figs. 4.7(a) and 4.7(b)]. However, bimodality can still be observed with distributed rod aspect ratios, high orientational diffusion rate, and is enhanced by including T4P-mediated cross linking.

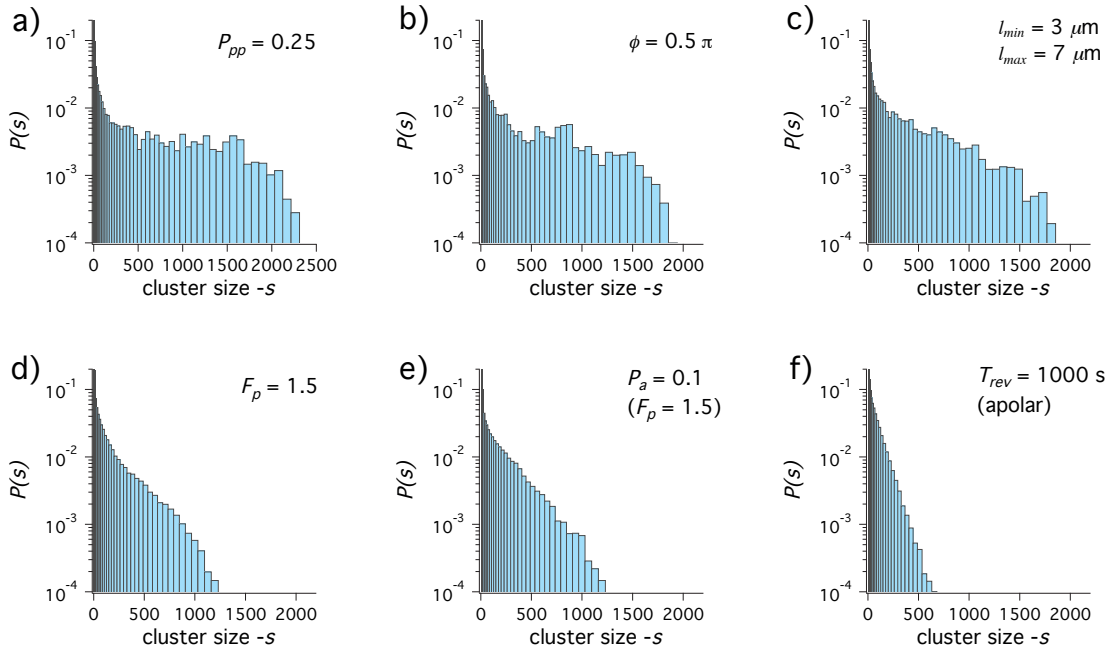

FIGURE 4.9: Cluster size distributions for the self-propelled rod models modified with pilus attachment between bacteria (a), orientational noise ($\phi = 0.5\pi$) (b), distributed aspect ratio ($\kappa_{min} = 4, \kappa_{max} = 8$) (c), stochastic movement: increased retraction force, decreased attachment probability ($F_{ret} = 1.5$, $P_a = 0.1$) (d), stochastic movement: decreased attachment probability ($P_a = 0.1$) (e), apolar movement ($\langle T_{rev} \rangle = 1000\ s$) (f).

Velocity is a function of the environmental parameter μ, the friction coefficient. Increased F_{ret} could be offset by increased μ. This part of my result is therefore superficial because bimodality would be sensitive to the type of substratum. Similarly, apolarity can yield the same movement characteristics as the polar case if the reversal period and movement rate are sufficiently high. Because these are free parameters, my result regarding the role of apolarity in negating bimodality only applies to a subset of conditions. While discontinuity is a defining aspect (the namesake) of *P. aeruginosa* twitching motility, continuity is possible if pilus binding is assured ($P_a = 1$). The mechanism of bimodal clustering published by Peruani *et al.* [38] could therefore apply to *P. aeruginosa* under fine-tuned environmental conditions, but this process would not be robust to changes in the nature of the substratum.

Here, the behavioral sensitivity to T4P attachment probability results in discontinuous movement and negates clustering. However, it also provides the capacity for heterogeneity in the environment to bias cell motility. Indeed, micro-Ck (see section 3.5.2) would not be possbile without this sensitivity to surface properties. In the next section, I will investigate whether micro-Ck due to EPS deposition and the preferential attachment of pili to secreted trails provides a robust stigmergy mechanism in the twitching rod model.

4.3 Stigmergy I: EPS trail following

4.3.1 Introduction

As discussed in section 3.5, the secretion of extracellular polymeric substances (EPS) by moving bacteria has been proposed as a trail formation mechanism in *M. xanthus* [52, 53]. Recently, this mechanism has also been proposed for *P. aeruginosa*, based on experiments and simulations with low numbers of surface-attached cells on a liquid-solid interface [54, 85].

In this section I approach the question of whether such a mechanism is feasible in the context of the motilty model introduced in section 3.4 and detailed in sections 4.1 and 4.2. In principle, the sensory area determined by the linear and radial pilus range (r_{pili} and ϕ, respectively) coupled with the random sampling of that area at a rate determined by the pilus retraction frequency t_{ret} enables such a mechanism, based on the tendency for bacteria to turn towards areas where pili are more likely to bind. Assuming that T4P are more likely to bind to secreted EPS, deposition of those substances can theoretically facilitate trail following through micro-Ck, the mechanism defined in section 3.5.2. Here, I investigate the robustness of trail following behavior to variations in the timescales of EPS secretion and degradation, and test whether the collective motion effects detailed in section 4.2 act to enhance or hinder trail following. [Note: in this section, T4P-mediated cross-linking was disabled, to isolate the effects of EPS secretion.]

This section is divided into three parts. Firstly, I will describe the numerical implementation of marker-based stigmergy based on EPS trail deposition as described in section 3.5. I will then introduce a metric designed to quantify trail following behavior and present the results of simulations where physical interactions between bacteria are ignored and the dynamics of the system are solely governed by stigmergy. Finally, I will demonstrate the collective behavior resulting from the interplay between EPS trail following and repulsive cell-cell interactions. The simulations in

this section do not include cell growth, and (as in the previous section) the statistics presented describe steady-state dynamics.

The results emphasize the following main points:

- When repulsive cell-cell interactions are ignored, marker-based stigmergy provides a trail following mechanism that is robust to variations in cell density, but highly sensitive to variations in pilus retraction frequency. This is due to the dual role of the pilus as both a sensory and motor apparatus.
- When repulsive cell-cell interactions are included, trail following from EPS deposition ceases to be robust to cell numbers and would therefore only be expected to facilitate such behavior in the low density condition in which collisions between cells are infrequent.

4.3.2 Numerical implementation of stigmergy

Note: this subsection is derived from the manuscript entitled: *Emergent pattern formation in an interstitial biofilm* that I wrote in collaboration with coauthors Christian Wolff, Cynthia B. Whitchurch, and Milos Toth [92, 93].

The simulation takes place in finite 2D space with periodic boundary conditions. The space is discretized into a square mesh with a pixel resolution of $\Delta x = w/4$, where w is the bacterial cell width of 1 μm. The pixels are used to accumulate a stigmergy tracer as the bacteria traverse the simulation space (Fig. 4.10). We used Eulerian integration to calculate changes in tracer level.

Bacteria deposit a trace in their environment represented by counts that decay exponentially in time and accumulate when a bacterium is present. Count accumulation in each pixel of area $[\Delta x]^2$ saturates according to:

$$\frac{dC^+}{dt} = k_p \frac{C_{max} - C(t)}{C_{max}} [\Delta x]^2 \,, \tag{4.8}$$

where k_p is the EPS trace deposition rate per unit area and C_{max} is the maximum tracer count per pixel. Accumulation competes with exponential decay taking place at rate β:

$$\frac{dC^-}{dt} = -\beta C(t) \,. \tag{4.9}$$

Because of the competition, a steady-state value $C_{st} \leq C_{max}$ is reached if a bacterium moves sufficiently slowly:

$$C_{st} = \Big[\frac{1}{C_{max}} + \frac{\beta}{k_p} \Big]^{-1} . \tag{4.10}$$

The steady-state value C_{st} is a function of the free parameter C_{max}, which represents the limit to which the environment can sustain continual modification. For all the simulations in this work, this value was set to $C_{max} = 1$.

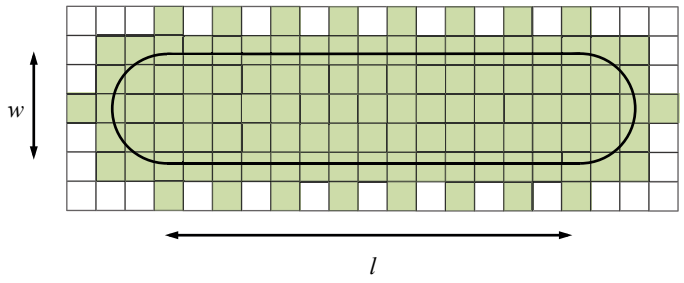

FIGURE 4.10: A discretized rod in two spatial dimensions. The green pixels are within the deposition area of the bacterium of length l and width w.

Based on previous literature [67, 87, 94], the proposed role of EPS in motility is modeled by making the local probability of pilus attachment to the substratum, P_a, scale with the the fraction K of the local area covered by EPS binding sites $K = C(x, y)/[\Delta x]^2$, so that movement is biased along trails.

$$P_a(K) = KP_{max} + (1 - K)P_{min}\,. \tag{4.11}$$

This value is bounded from below by a finite probability P_{min}, which corresponds to the natural binding affinity of T4P to the unaltered surface and defines the probability of attachment when $K = 0$. Similarly, we define a maximum attachment probability P_{max}, which represents the affinity of the pilus tip to binding sites provided by the EPS, and corresponds to the situation where $K = 1$. Simulation parameters are summarized in Table A.1.

4.3.3 Quantifying stigmergy

Describing trail following behavior quantitatively requires an explicit definition of stigmergy in the context of this system. In general, stigmergy is defined as *persistent cues left in the environment that affect the behavior of the same or other individuals arriving at the same location at a later point in time* [17]. In our case, the state variables describing the behavior of an individual are its location vector (r), its physical orientation (θ), and its velocity vector $\vec{v}$. For an isolated individual, the orientation and velocity vectors are highly correlated because of the polar nature of bacterial movement. However, in groups the velocity vector can be determined by the direction of a cluster, and may not correlate with the physical orientation of each individual within that cluster. Because our definition of stigmergy concerns individual behavior, we will consider the location and physical orientation as the metrics of interest when describing stigmergic processes. In this context we can narrow the definition of stigmergy as *persistent cues left in the environment that influence the physical orientation of the same or other individuals arriving in the same location at a later point in time.* In principle, the response to such cues need not be mimicry, but in the present case we are concerned with how stigmergy leads to trail following, which implies that mimicry is the response of interest in this specific

case. Now the definition of stigmergy becomes even more specific: *persistent cues left in the environment that cause individuals arriving at a the same location at a later point in time to mimic the physical orientation of the previous occupant of that space.*

This final definition is amenable to quantification. To achieve this, I implemented the following algorithm: the space is discretized into square subspaces with dimensions on the order of the cell length ($l = 4$). At each point in time (for which data is recorded), every bacterium in the simulation is given an index that corresponds to the subspace in which it currently resides. When one of these indices changes, it means a bacterium has moved from one subspace to another. When such an event occurs, the subspace location previously occupied is assigned a vector corresponding to the physical orientation of the bacterium that just left the space. Vectors are only recorded in subspaces associated with exit events. This assignment process is carried out over the entire space for each point in time. The result is a data cube with indices x, y, t containing for each subspace with index x, y the orientation of each bacterium that exited the space, recorded at the time index t associated with that exit event. Stigmergy can then be quantified by examining the coherence of each subspace vector in time. To do this I will define $S(t, \Delta t, r) = |\langle e^{i\theta(t)} \rangle_{[t,t+\Delta t]}|$, the magnitude of the time-averaged vector for the subspace r over the interval $[t, t + \Delta t]$. If perfect mimicry occurs in the given subspace for the entire steady state, $S = 1$ for all values of Δt. If deviations occur, S will decrease as the time interval Δt increases. The steady-state time-space average $\langle S \rangle_{r,t}(\Delta t)$ provides a meaningful metric of trail stability as a function of time (i.e., for increasing values of Δt), and I will use this value as the trail following metric in the analysis to follow.

4.3.4 Results: EPS trail following, preamble

In this section, I will present the results of simulations using two variants of the model. The first is designed to isolate the effects of EPS trail following in the

context of the bacterial motility mechanism. This first variant ignores repulsive interactions between bacteria (the bacteria can occupy the same space), which simplifies the model and allows the investigation of the parameters that directly affect stigmergy, while ignoring collective motion effects that result from collisions between bacteria. The results using this model variant highlight the importance of the retraction frequency t_{ret}, which defines the rate at which bacteria sample the space in front of them and the magnitude of displacement resulting from attachment. The second variant includes cell-cell repulsion and illustrates how trail following due to EPS deposition is made less robust by collective motion and scattering due to collisions between cells. For the simulations in this section, the maximum and minimum attachment probabilities were kept constant at $P_{max} = 1$ and $P_{min} = 0.1$. This represents the scenario where pilus affinity to freshly secreted EPS is very high, and there is a small but finite affinity between the pilus and the native surface on which the bacteria are moving.

To summarize, the results of this section indicate that stable trail following due only to EPS excretion is a fine-tuned behavior that will only be observed in circumstances of low cell density, and is highly sensitive to pilus retraction dynamics. Indeed, the experimentally derived space and time scales of T4P mediated motility discussed in section 4.1 do not allow for trail following due to EPS deposition in realistic circumstances.

4.3.5 Variant 1: ignoring collisions

With collisions between cells disabled, the system's behavior is dictated entirely by the parameters defining the deposition and degradation of EPS, and the ability of the bacteria to effectively sense the EPS gradients in space. The deposition rate k_p determines how quickly the attachment probability in the coverage area of a cell will reach the steady state. The degradation rate β determines how long it takes for the trace to disappear, and the ratio of the degradation and deposition rates determines

the steady-state attachment probability (the maximum value that can be reached for a given combination of k_p and β).

Because the retraction period t_{ret} defines the amount of time between attachment attempts, it determines the rate at which the bacteria sample the space in front of them that is available to their pili. It also helps determine the maximum possible displacement due to a single retraction event (limited also by the pilus length (r_{pili}). Because the motility mechanism combines this sensory and motor functionality, the retraction period t_{ret} is a fundamentally important parameter that determines whether or not EPS deposition can lead to trail following behavior. To illustrate this point, Figures 4.11 and 4.12 show morphological phase diagrams for two different values of t_{ret} (with collisions disabled) where the control parameters are the EPS deposition and degradation rates.

Figure 4.11 represents the situation where $t_{ret} = 0.1\ s$, which allows the bacteria almost perfect sampling of their local environment and leads to robust trail following. Three types of behavior are observable in Figure 4.11: the equilibrium phase where the EPS has become uniform which occurs when $k_p \gg \beta$, a trail-following phase that is strongest when $k_p \approx \beta$ but exists over a wide swath of parameter space, and an equilibrium phase that occurs when $k \ll \beta$ (which also corresponds to $C_{st} \ll C_{max}$ and $P_a(C_{st}) \approx P_{min}$). These three phases are highly reminiscent of those observed by Rauch *et al.* in their numerical study of stigmergy inspired by trail following in ants [56]. Indeed, their lattice-based model implementation did not include any finite-volume effects.

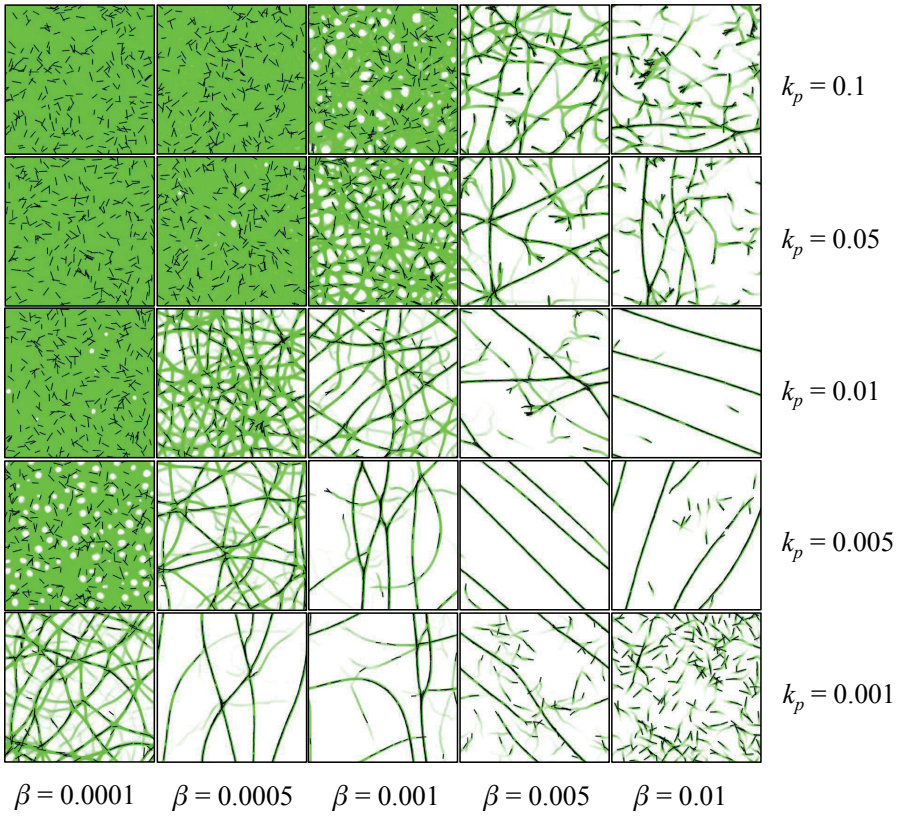

FIGURE 4.11: Snapshots taken at t_f for simulations of EPS trail following with collisions between bacteria disabled and the pilus retraction period $t_{ret} = 0.1\ s$ for a quasi-continuous sampling of EPS concentration in space. EPS trails are shown in green and bacteria are shown as black rods. Each frame corresponds to a different combination of degradation rate β and deposition rate k_p. The uniform, stigmergic, and sparse morphologies are clearly identifiable.

On the other hand, Figure 4.12 was produced by setting $t_{ret} = 10\ s$ (the value derived from the experiments presented in [34]), which allows only limited sampling of the space in front of each cell, and allows large movements to result from each binding event. Due to this stochastic sampling, no trail-following phase can be clearly identified in Figure 4.12, where the uniform phase appears to transition directly to the sparse, equilibrium phase.

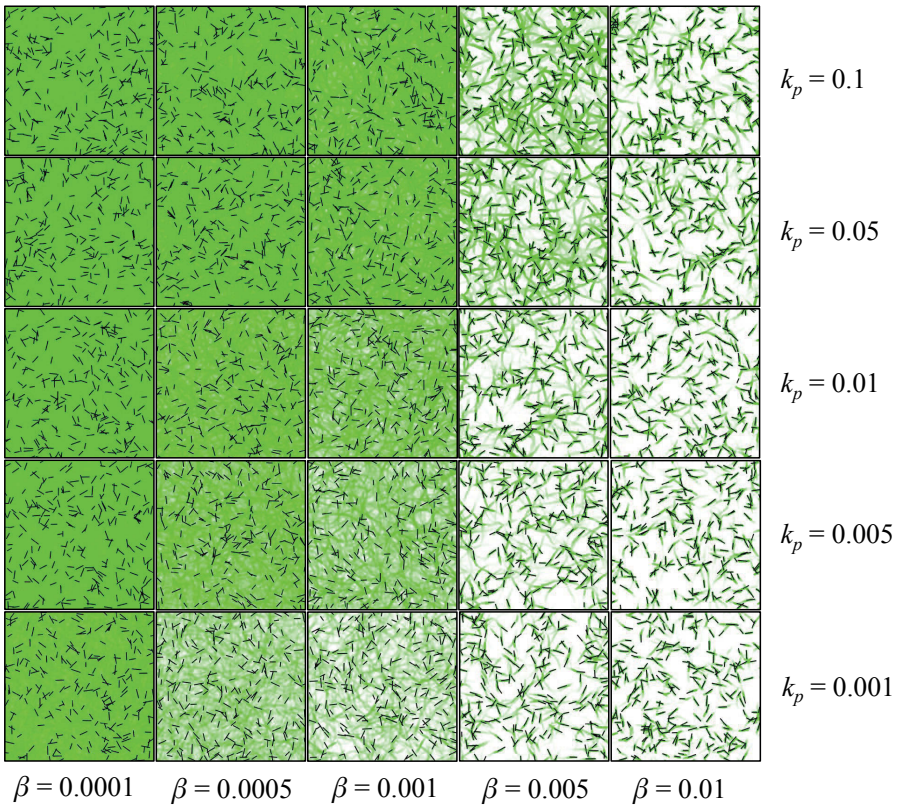

FIGURE 4.12: Snapshots taken at t_f for simulations of EPS trail following with collisions between bacteria disabled with the pilus retraction period set to the experimentally constrained value $t_{ret} = 10\ s$ for stochastic sampling of EPS concentration in space. EPS trails are shown in green and bacteria are shown as black rods. Each frame corresponds to a different combination of degradation rate β and deposition rate k_p. No stigmergic region can be clearly identified between the uniform and sparse morphologies.

These qualitative observations are confirmed by examining the stigmergy parameter $\langle S \rangle(\Delta t)$ for these two cases (Fig. 4.13), which shows that trail following is robust over long timescales when trail sampling is continuous ($t_{ret} = 0.1\ s$), but is quantitatively absent when trail sampling is stochastic ($t_{ret} = 10\ s$), for all combinations of k_p and β examined.

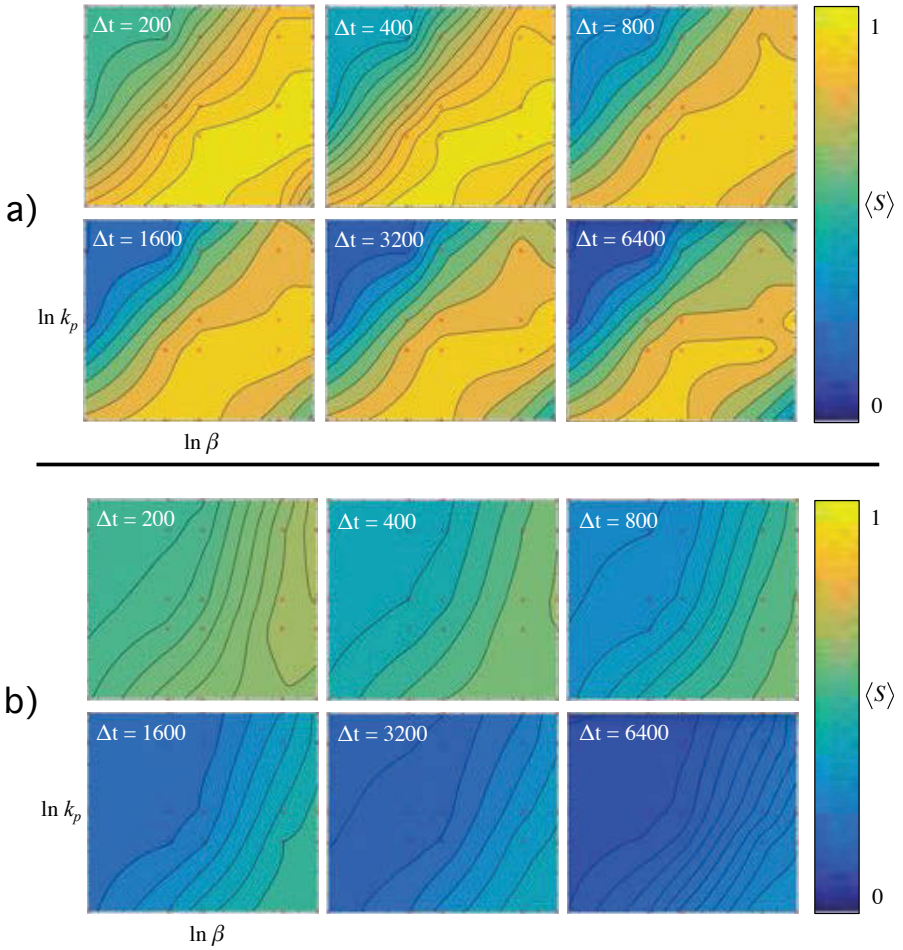

FIGURE 4.13: Interpolated contour maps of the stigmergy parameter $\langle S \rangle$ as a function of EPS degradation rate β, deposition rate k_p, and time interval Δt. Data calculated from simulations are shown as red circles superimposed on the interpolated contour. (a) Continuous spatial sampling with $t_{ret} = 0.1$ s leads to robust trail following that persists in a large band of parameter space. (b) Stochastic sampling with $t_{ret} = 10\ s$ is not sufficient to produce trail following and $\langle S \rangle$ decreases across the entire parameter space as the time interval Δt increases.

4.3.6 Variant 2: including collisions

In this section, repulsive collisions are included in the behavioral model. This introduces effects that can compete with trail following behavior and makes the phenomenon sensitive to the bacterial density. In particular, the robust trail-following phase in the collision-free model with continuous spatial sampling is not stable when collisions are considered. Even so, there is a large area of parameter space where

trail following is compatible with collisions when the sampling rate is continuous and the population is dilute. However, as the population increases, the trail-following phase disappears due to competing collective motion effects. Trail following does not occur when stochastic spatial sampling is considered, as expected based on the results of the collision-free model.

When the bacterial density is low, collisions between cells are less frequent. Therefore, it is reasonable to expect that at some low bacterial density the behavior of the model including collisions should approximate that of the collision-free model. Our results qualitatively confirm this expectation: for a low population of $N = 125$, a trail-following phase can be observed in the morphological phase diagram (Fig. 4.14). However, the robust quasi-1D paths observed in the corresponding collision-free model (Fig. 4.11) are not observed. Such configurations contain a high degree of overlap between the bacteria occupying narrow trails, and are therefore absent when collisions are included due to buckling of 1D structures. Even so, trail following is qualitatively observable and is quantitatively stable over intermediate timescales [Fig. 4.16(a)] if the conditions of low cell numbers and continuous spatial sampling are met.

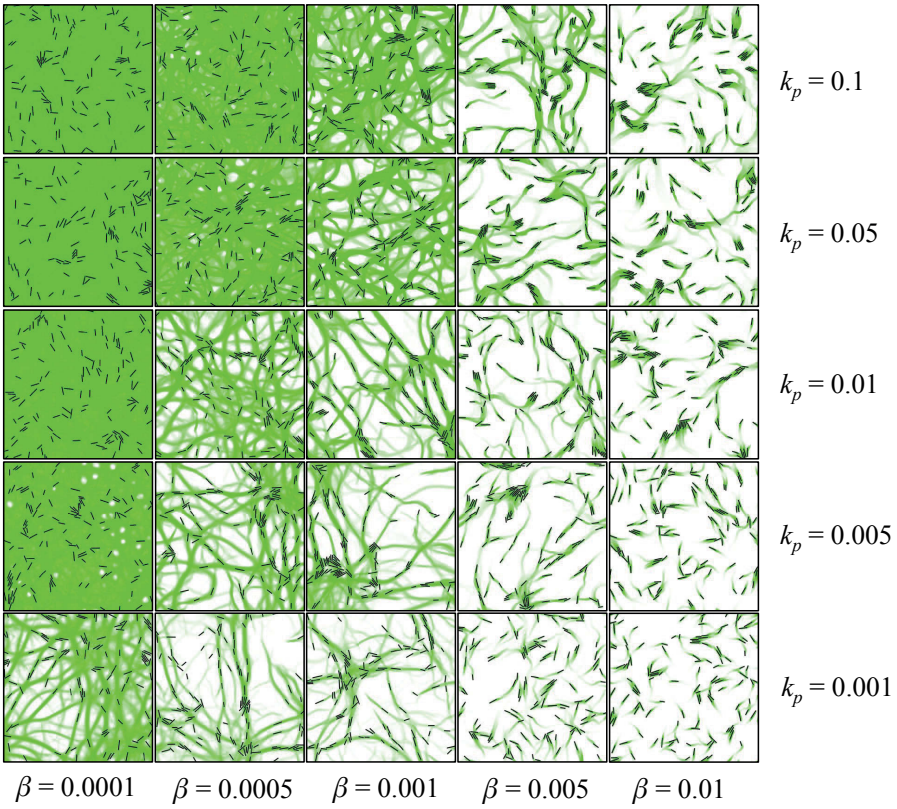

FIGURE 4.14: Snapshots taken at t_f for simulations of EPS trail following with collisions between bacteria enabled with a dilute population $N = 125$ and pilus retraction period $t_{ret} = 0.1\ s$ for continuous sampling of EPS concentration in space. Each frame corresponds to a different combination of degradation rate β and deposition rate k_p. EPS trails are shown in green and bacteria are shown as black rods. A stigmergic phase can be identified but trails are less defined due to the competing effects of collisions, clustering, and collective motion.

If cell numbers are low and nutrients are plentiful, the bacterial population can be expected to increase. Figure 4.15 and 4.16(b) show that the trail-following phase is not robust to increases in the bacterial population. Indeed, if the cell number used to generate Figure 4.14 is doubled to $N = 250$, the trail-following phase is not observable in the corresponding morphological phase diagram (Fig. 4.15) and the stigmergy parameter $\langle S \rangle(\Delta t)$ is low on all but the shortest timescale examined.

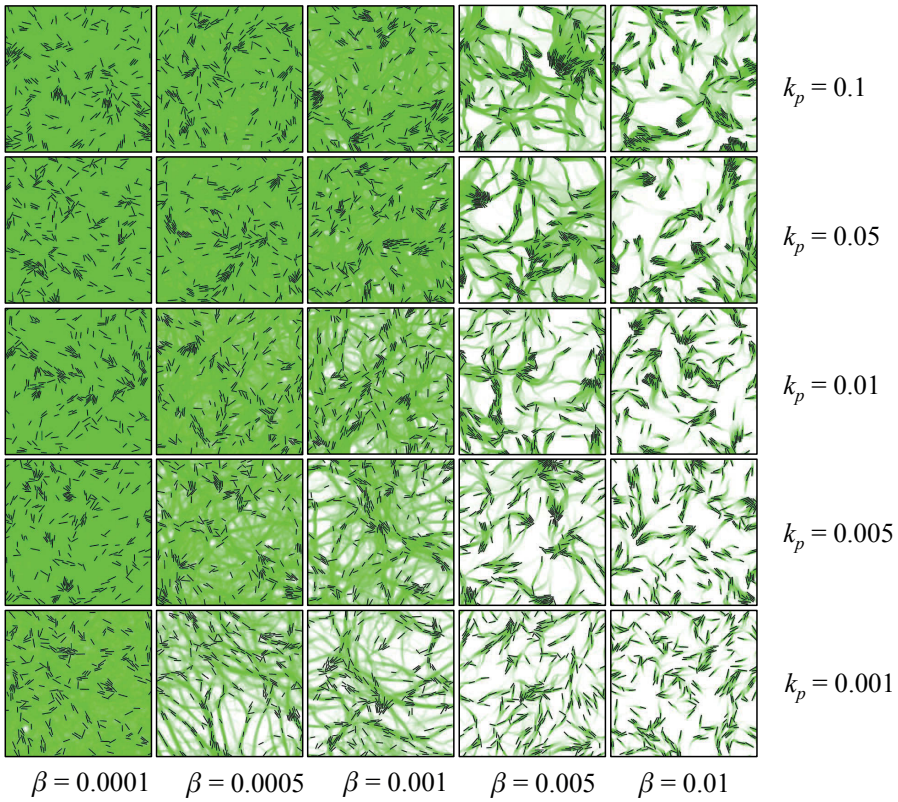

FIGURE 4.15: Snapshots taken at t_f for simulations of EPS trail following with collisions between bacteria enabled with a dilute population $N = 250$ and pilus retraction period $t_{ret} = 0.1\ s$ for continuous sampling of EPS concentration in space. Each frame corresponds to a different combination of degradation rate β and deposition rate k_p. EPS trails are shown in green and bacteria are shown as black rods. While EPS deposition promotes clustering, collective motion effects dominate over stigmergic trail following in the nonuniform phase.

The higher values of $\langle S \rangle$ on short timescales for $k_p \leq \beta$ are likely due to direction reversals occurring faster than orientational decoherence, a result of the substantially decreased steady-state attachment probability in these conditions. For completeness, the stochastic sampling regime is represented by the stigmergy parameter data in Figure A.2. As expected, when $t_{ret} = 10\ s$ EPS trail following does not occur for any of the values of k_p, β, or N investigated here.

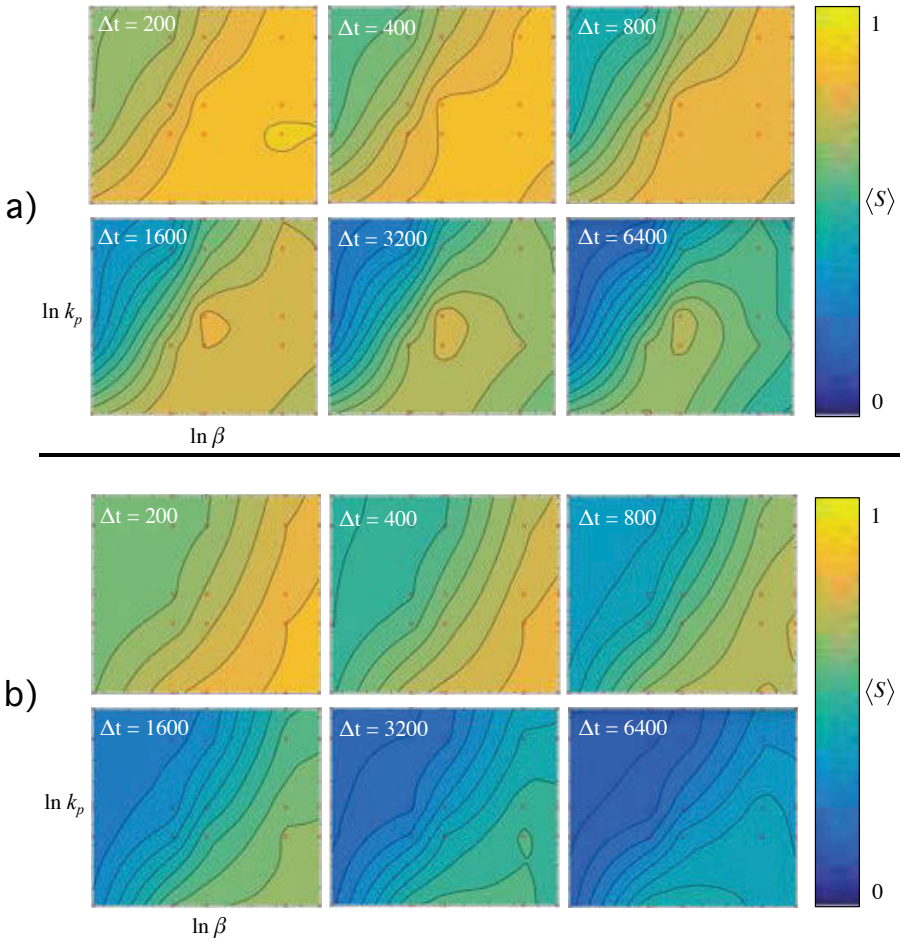

FIGURE 4.16: Interpolated contour maps of the stigmergy parameter $\langle S \rangle$ as a function of EPS degradation rate β, deposition rate k_p, and time interval Δt. For these plots, cell-cell repulsion was enabled and spatial sampling was continuous ($t_{ret} = 0.1\ s$). Data calculated from simulations are shown as red circles superimposed on the interpolated contour. (a) With $N = 125$, trail following persists in a small region of parameter space. (b) With $N = 250$, trail following ceases to occur due to interaction effects.

The results presented in this section are somewhat surprising. While EPS trail following is well-established in the literature on bacterial emergence, these results suggest that it is not responsible for the trail following observed in *P. aeruginosa* twitching motility [48]. In the next section, the model is extended to include the furrowing process reported by Gloag *et al.* [45]. The results will emphasize the importance of this mechanism in the formation of trail structures in the steady state.

4.4 Stigmergy II - sematectonic stigmergy

4.4.1 Preamble

This section is derived from a manuscript entitled: *Emergent pattern formation in an interstitial biofilm* that I wrote in collaboration with co-authors Christian Wolff, Cynthia B. Whitchurch, and Milos Toth [92, 93]. Christian taught me how to translate the simulation code from MATLAB to C++, and provided the key insight that capillary forces are likely responsible for substratum restitution. Cynthia Whitchurch participated in many fruitful discussions of bacterial motility and helped guide the conceptualization of the biophysical model presented in Chapter 3. Milos Toth supervised the project and edited the manuscript. For this section, I truncated the original manuscript to eliminate redundancies, and changed the symbols representing some model parameters for consistency with previous sections of the thesis.

4.4.2 Introduction

Here we investigate collective behavior of an interstitial biofilm by using an individual-based model that accounts for stigmergy (i.e., path following) [18, 19, 45, 46] by bacteria that comprise the biofilm. We show that subtle differences in environmental conditions can cause dramatic shifts in the emergent, collective behavior of the colony due to stigmergic effects. Specifically, an increase in substratum stiffness yields a transition from dispersed, disordered movement, to a highly stable, structured morphology characterized by a high local density of constituent bacteria that move efficiently within self-constructed channels. The ordered state, controlled by physical properties of the environment, results in a condition which reconciles two often mutually exclusive properties that are typically associated with fitness advantages: high mobility and high local density. Our findings provide insight into the

relationship between bacterial movement mechanics and the physical properties of the enclosing environment and, more broadly, into the nature of emergence and pattern formation in complex biophysical systems. Understanding such processes can help explain adaptation to specialized habitats, and inform the design of experiments and biomedical surfaces.

4.4.3 Model

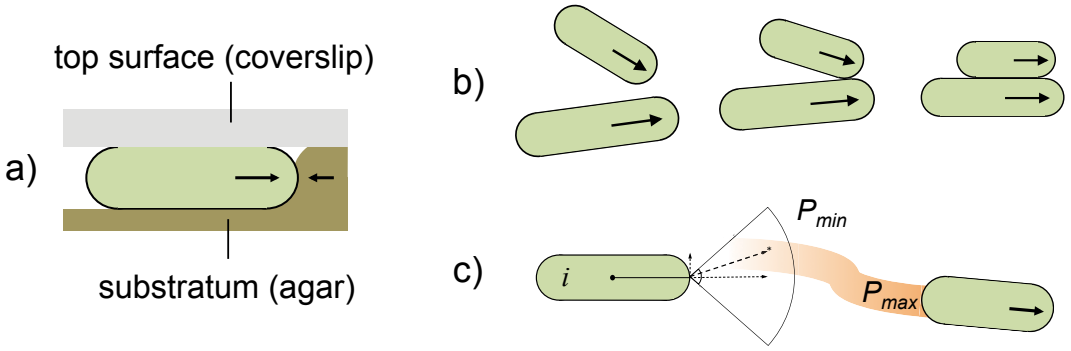

FIGURE 4.17: Primary processes implemented in the bacterium behavioral model. (a) Furrowing through an elastic substratum. (b) Alignment of rod-shaped bacteria through physical repulsion. (c) Movement bias induced by excreted extracellular polymeric substances. Bacterium i samples the space accessible by its pili by randomly selecting a point within an arc extending from a forward pole. The pilus attachment probability scales with EPS concentration (shown in orange), up to a maximum value P_{max}. In the absence of EPS, the attachment probability is given by P_{min}.

Building on the model discussed in the previous section, we implemented an individual-based model of bacterial behavior in a quasi-two-dimensional (quasi-2D) environment (Fig. 4.17). It consists of two primary components: (i) a realistic model of physical interactions between rigid, rod-shaped bacteria confined in the space between a viscous medium and a solid surface [Fig. 4.17(a) and 4.17(b)], in which the resistance to motion due to deformation of the substratum is quantified by a single parameter (a stiffness coefficient, γ), and (ii) bacterial motility that is enabled by the extension and retraction of type IV pili (T4P) and biased by extracellular polymeric

substances (EPSs) which are excreted by the bacteria [Fig. 4.17(c)]. We intentionally exclude complex phenomena such as chemotaxis and contact-based signaling in order to show that explicit simulation of high order biochemical communication processes is not necessary to explain this type of biofilm self-organization and pattern formation. Instead, morphogenesis results from two basic forms of stigmergy arising from the formation of furrows in a viscous substratum and following of EPS trails deposited by the moving bacteria. EPS following is implemented as preferential binding of pili to the EPS, as shown in Figure 4.17(c) [87, 94]. This general phenomenon is ubiquitous to a broad range of bacteria such as *P. aeruginosa* and *M. xanthus* that use type IV pili for movement while actively modifying the surface properties through substance excretion [67, 87, 94]. (Simulation source code is available, see appendix A.4.4)

We note that in this model, the EPS does not directly cause alignment of neighboring bacteria. Instead, alignment results from collisions of the rigid, rod-shaped individuals [Fig. 4.17(b), Appendix A.2.1]. We parametrized the model based on experimental data gathered for *P. aeruginosa*. It is, however, flexible and directly applicable to a broad range of biofilms that use T4P for surface motility [69].

4.4.4 Physical properties of individuals

As in the previous sections, translational motion is calculated using:

$$\frac{dx}{dt} = \frac{\vec{F}}{\mu l}\,, \tag{4.12}$$

where $\vec{F}$ is the sum of forces generated by motility $\vec{F}_p$, environmental forces $\vec{F}_s$, and particle-particle interactions $\vec{F}_{ij}$ so that $\vec{F} = \vec{F}_p + \vec{F}_s + \sum_j \vec{F}_{ij}$.

Similarly, angular velocity is given by:

$$\frac{d\theta}{dt} = \frac{12\tau}{\mu l^3}\,, \tag{4.13}$$

in which $\tau = \tau_p + \tau_s + \sum_j \tau_{ij}$ is the net torque on particle i due to motility τ_p, environmental potentials τ_s, and interaction forces τ_{ij}.

4.4.5 Sematectonic stigmergy: furrowing

In the full model, there are two types of counts, C_s and C_p, each with their own deposition and degradation rates (k_s, β_s and k_p, β_p, respectively). C_s accounts for the formation of furrows in the substratum and C_p accounts for the effects of excreted EPS on the probability of T4P attachment to the surface. The implementation of EPS secretion is detailed in section 4.3.2.

The substratum-coverslip interface resists debonding, thereby generating a force that resists bacterial motion and biofilm expansion. In our model, this force is calculated by allowing a surface deformation potential U_s to scale with the local value of C_s and the stiffness coefficient γ:

$$\gamma = \frac{dU_s}{dC_s}\,, \tag{4.14}$$

$$\vec{F}_s(x,y) = \gamma \nabla C_s(x,y)\,, \tag{4.15}$$

where $\nabla C_s(x,y)$ is the local central difference between neighboring pixels ΔC_s divided by the pixel spacing Δx.

To find the force applied along the length of a rod, $\vec{F}_s(x,y)$ is integrated over the pixels (x,y) within the area of each rod segment A_{seg} centered at position r where:

$$r \in \{-\frac{l}{2}, -\frac{l-w}{2}, -\frac{l-2w}{2} \ldots \frac{l-w}{2}, \frac{l}{2}\}\,, \tag{4.16}$$

$$\vec{F}_s(r) = \sum_{(x,y)\in A_{seg}} \vec{F}_s(x,y)\,, \tag{4.17}$$

$$\vec{F}_s = \sum_r \vec{F}_s(r)\,, \tag{4.18}$$

so that the appropriate torques can be applied:

$$\tau_s = \sum_r \vec{F}_{s\perp} r\,. \tag{4.19}$$

Here γ scales the resistance felt by a moving rod with respect to the local topographical gradient (Fig. 4.19). Physically, γ is related to the elastic properties of the substratum.

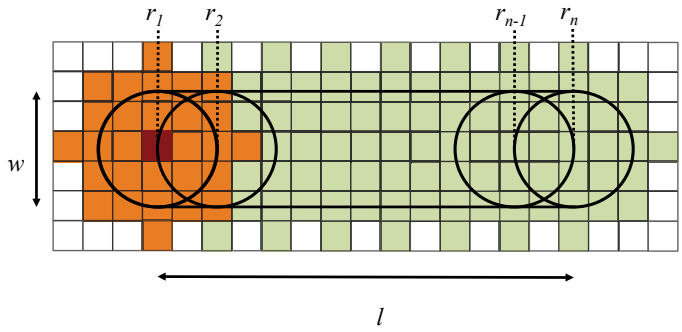

FIGURE 4.18: A discretized rod in two spatial dimensions. The squares represent the pixels used for accumulation of stigmergy tracer counts. The orange squares represent those used for calculating the local forces from substratum resistance at r_1, the discrete pixel corresponding to the center of segment 1 is colored in red.

Capillary forces are likely responsible for the observed substratum reformation in the presence (but not in the absence) of a coverslip [45], and would be relevant to γ, β_s, and k_s. Because stiffness would affect the rate at which the substratum responds to the presence of a bacterium and the rate at which furrows refill due to capillary forces, we make $\beta_s \propto \gamma^{-1}$ and $k_s \propto \gamma^{-1}$, which is equivalent to stating:

$$\frac{dU_s}{dt} = \gamma \frac{dC_s}{dt} \tag{4.20}$$

is independent of γ. This means we can recast Eqs. (4.8) and (4.9) as

$$\frac{dU_s}{dt}^{+} = k_U \frac{C_{max} - C(t)}{C_{max}} [\Delta x]^2 \,, \tag{4.21}$$

and

$$\frac{dU_s}{dt}^{-} = -\beta_U C(t) \,, \tag{4.22}$$

respectively, where $k_U = \gamma k_s = 0.05$ and $\beta_U = \gamma \beta_s = 2.5 \times 10^{-4}$ are constant for all values of γ, and describe the deformation and restitution rates of the potential field corresponding to surface topography. That is, the capillary forces and deformation forces produced by the bacteria are assumed to be independent of substratum stiffness. Consequently, it takes bacteria longer to deform a stiffer substratum, but the resulting deformation will resist restitution, and persist longer in the absence of bacteria. The restitution rate must be significantly slower than the movement rate of bacteria in order for furrows to persist in the absence of bacteria. If the restitution rate is on the order of the individual movement rate, the force generated by substratum deformation resembles surface tension that holds clusters of cells together.

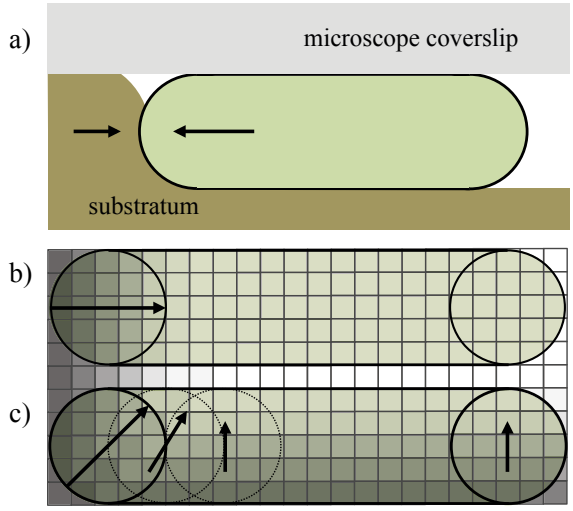

FIGURE 4.19: Forces are generated due to deformation of the substratum. (a) Schematic illustration of a bacterium furrowing into the interstitial space where it must overcome resistance from the substratum. (b, c) Top-down schematic of simulations where spatial gradients from low trace levels (dark pixels) to high (light pixels) correspond to a force field that resists particle motion due to the elastic properties of the substratum. If the gradient is aligned with the long axis of a particle, it generates a translational force only (b). A non-uniform gradient aligned with the short axis of the particle gives rise to torque as well, which is evaluated at each rod segment (c).

4.4.6 Parametrization

See section 4.1 for more details with respect to how model parameters were derived from Skerker *et al.*'s [34] analysis of individual behavior. The section below is presented as it was in the manuscript on which this chapter is based.

While precise estimates do not exist for many of the model input parameters, it has been documented that, during unobstructed twitching motility, *P. aeruginosa* move discontinuously at approximately 0.3 to 0.5 μm/s in excursions of approximately 5 μm, and pili can reach through an arc of at least 0.5π radians [34]. The average polarity reversal rate and its distribution are important parameters with respect to collective motion [50] and could be subject to a biochemical regulation mechanism [68, 95]. This regulation process is not well-characterized, and may be unique to specific species, strains and conditions. Since there are no long-range chemical gradients

in our simulations, we make the minimal assumption that bacteria reverse polarity several times during a division cycle, which can range from about 30 min to 200 min depending on conditions (see, for example, Refs. [96, 97]). Visual inspection of the microscopy data in Ref. [45] indicates that bacteria range from about 3 to 7 μm in length and are about 1 μm in girth.

Based on the observations and limitations discussed above, the following parameters can be roughly established: t_{rev}, σ_{rev}, l_{max}, l_{min}, r_{pili}, ϕ, and w. The observed unobstructed movement rate of 0.5 μm/s is established by balancing t_{ret}, F_{ret}, and μ (see section 4.1). Biological parameters that must be estimated are: k_p, P_{max}, P_b, and F_r. The repulsion force parameter F_r is simply set to a value that prevents overlap of rod centerlines during collisions. We set the EPS deposition rate k_p, to a value that allows the steady-state EPS concentration to be reached in the time that a particle passes over an area.

We set the maximum surface attachment probability $P_{max} = 0.3$, a value that approximately reconciles the maximum observed long-time movement rate observed for *P. aeruginosa* in the interstitial environment of 0.2 μm/s and the maximum single-retraction velocity of 0.5 μm/s. We set the affinity of the pilus tip to the bacterial cell surface $P_b = 0.25$, slightly lower than the maximum possible EPS attachment probability. This decision was based on the idea that attachment to the cell surface would likely be mediated by EPS materials which would have to bind to the pilus tip as well as the cell surface for movement to result from retraction. We set P_b higher than P_{min} based on the assumption that attachment to a cell surface would be favored relative to the native surface.

The experiments we wish to simulate (systematic alteration of substratum conditions) do not alter the bacteria. Therefore, their physical and biological properties were fixed in the model.

With biological parameters fixed, those relating to the environment can be systematically tuned and the results compared with experimental observations [45, 48]. The

environmental parameters are: γ, k_s, β_s, μ, P_{min}, and β_p.

The minimum attachment probability, P_{min} corresponds to the affinity of the pilus tip to either the substratum or the coverslip surface. In order for the stigmergic effects of EPS excretion to manifest, P_{min} must be lower than P_{max} so that spatial variations in binding probability can bias movement.

The timescale associated with topographical dynamics in the substratum is defined by β_s and k_s, which are important parameters with respect to pattern formation. If β_s is too high, the substratum will immediately reform after passage of a particle and individuals or clusters will become isolated from each other as the substratum closes behind them. The rate (k_s) at which particles deform the substratum determines how long it takes for a stationary particle to generate a topographical gradient around itself. Therefore, (for fixed γ, μ, and F_{ret}), k_s, t_{ret}, and P_{min} will determine whether or not movement of individuals is observed.

4.4.7 Initialization

In each simulation, 1000 particles were placed in random positions throughout a square space (side length $L = 160$ μm) with periodic boundary conditions. Particles were assigned orientations (θ), and lengths (l) from uniform distributions $[0, 2\pi)$ and $[l_{min}, l_{max}]$, respectively. Reversal clocks were initially randomized by assigning each particle a reversal period from the Gaussian distribution described by t_{rev} and σ_{rev}, and allowing the values to count down and reset according to the rules of the model for a time period of $10t_{rev}$ before starting the simulation. Pili are assumed to be initially unattached to the surface, with the countdown to the first attachment attempt selected from the uniform distribution $[0, t_{ret}]$. More details about simulation implementation can be found in Appendix A.2.2. The model parameters are summarized in Table A.1.

4.4.8 Results

The only parameter that we varied in order to cause the changes in collective behavior discussed below is the stiffness coefficient (γ) which governs the resistance experienced by the motile bacteria, the rate at which they deform the local topography, and the rate at which the furrows refill. Altering γ is akin to changing the concentration of monomeric precursor when preparing the substratum (e.g., agar or gellan gum), or altering the concentration of stabilizing divalent cations in the mixture.

We start by characterizing clustering and connectivity in the simulated biofilm for systematically increasing values of γ. The steady-state cluster size distribution (CSD), defined as the probability density P of finding an individual within a cluster of size s, is affected by the physical properties of the substratum, as is demonstrated by the plots of $P(s)$ versus γ shown in Figure 4.20. At low values of γ, the bacteria experience little resistance to movement through the substratum, no clear trail systems are visible in snapshots of the colony in the steady state [Fig. 4.20(a), Supplemental Movie S3 (Appendix C.2)], and the CSD decays exponentially [Fig. 4.20(b)]. As γ is increased, the bacteria form networks of interconnected trails [Fig. 4.20(c), Supplemental Movie S4 (Appendix C.2)] and the CSD transitions to a bimodal distribution [Fig. 4.20(d)]. The formation of large clusters that approach the system size (of 1000 bacteria) is observed when the resistance to motion approaches the force exerted by individuals attempting to move through the substratum. We refer to this process as *percolation*, because it indicates an approach to global connectivity between most of the individuals in the system. Although a finite-size study is outside the scope of the present work, it is possible that percolation would not occur in much larger systems. The maximum cluster size may instead converge to some value smaller than the system size. Percolation theory suggests that this tendency would depend sensitively on the particle density.

To quantify the transition from equilibrium clustering to percolation, we plot the maximum cluster size S_{max} reached for each value of γ, and find distinct scaling behaviors below and above a critical value $\gamma_c \approx 0.49$ [Fig. 4.20(e)], which marks the onset of the transition to the percolated state. The transition region ($\gamma_c \geq \gamma \geq \gamma_{sat}$) is highlighted by the red line in Figure 4.20(e). The maximum cluster size distribution obeys a power law within the transition region [Fig. 4.20(f)], and the system resides in stable unpercolated and percolated states below ($\gamma \leq \gamma_c$) and beyond ($\gamma \geq \gamma_{sat}$) the transition region. The change in clustering behavior around γ_c is extremely abrupt, and a cautionary sign for experimentalists – a subtle change in a physical parameter such as stiffness around a critical value can produce a dramatic change in colony behavior that may be caused purely by unintended changes in a poorly-controlled parameter.

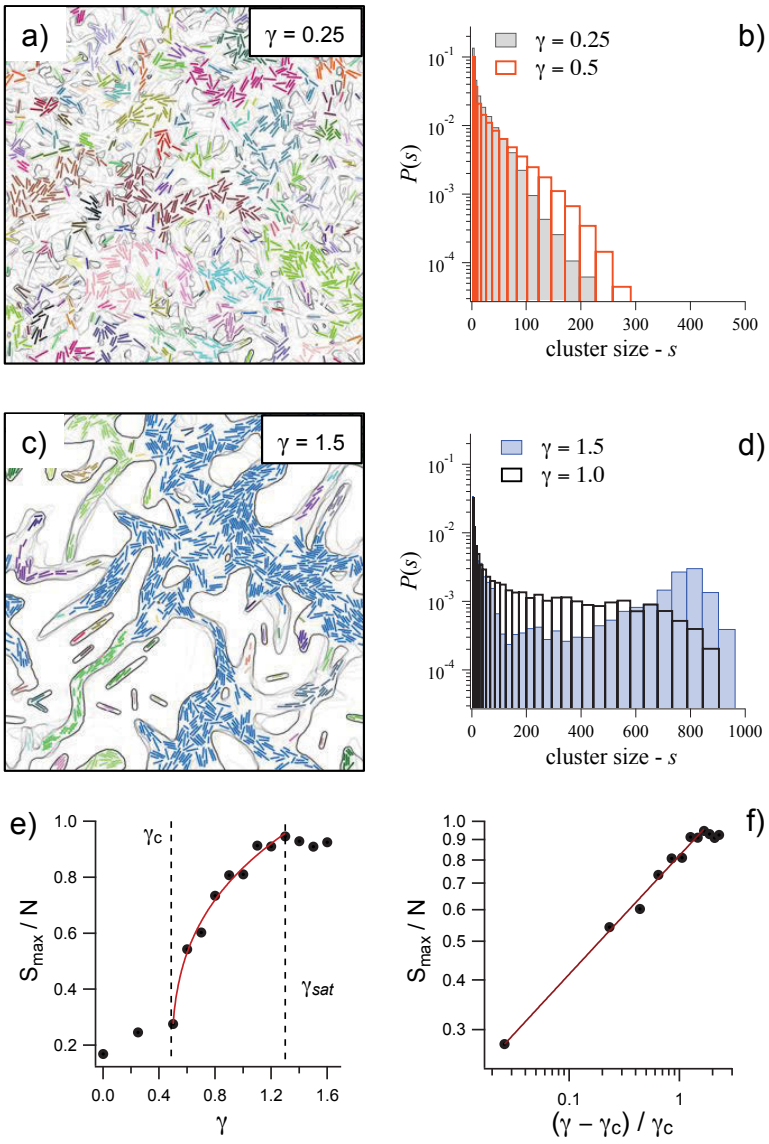

FIGURE 4.20: Clustering induced by a change in substratum stiffness, γ. (a, c) Snapshots of the colony illustrating the the influence of γ on clustering in the steady state. Bacteria in each cluster are given the same (arbitrary) color and the furrow edges are shown in gray. (b, d) The cluster size distribution, $P(s)$, transitions from an exponential decay to a bimodal distribution as γ is increased from 0.25 (low substratum stiffness) to 1.5 (high substratum stiffness). (e) Maximum cluster size S_{max} (normalized to the system size of N bacteria) versus γ, revealing a clear, critical value γ_c that marks the onset of stable trail formation. The red line indicates the transition region between unpercolated ($\gamma \leq \gamma_c$) and percolated ($\gamma \geq \gamma_{sat}$) states. (f) The maximum cluster size obeys a power law as a function of γ within the transition region, which we confirm by rescaling γ to γ_c.

The change in CSD from an exponential to a bimodal distribution seen in Figures 4.20(b) and 4.20(d) is not unique to our study. A similar transition has been observed in prior simulation studies of self-propelled rods, where it indicates a change from a state of uncorrelated movement to one of ordered collective motion [38]. Experiments with the bacterium *M. xanthus* have shown similar behaviors, with long-tailed or bimodal CSDs occurring below and above a critical cell density [39, 50]. In these studies, a critical density marks the transition from uncorrelated movement to collective motion, which is facilitated by high degrees of orientational alignment between individuals in contact. More broadly, density and orientational coherence between neighbors are fundamentally important in systems of moving agents, and constitute the two most basic control parameters in minimal models of collective motion [16].

We therefore proceed by analyzing changes in orientational coherence (the degree of alignment between neighboring bacteria) and local density associated with the changes in clustering and percolation seen in Figure 4.20.

Qualitatively, the snapshots in Figure 4.21(a) indicate the existence of two distinct states at low and high values of γ, and that the local density and degree of alignment between neighboring bacteria increase with γ, as the system transitions from the unpercolated to the percolated state. To quantify local alignment, we compute the orientational coherence $\langle\Phi\rangle$, (see Appendix A.4.2) between bacteria versus the degree of separation (DoS). For two bacteria in contact DoS = 1, for second-nearest neighbors DoS = 2 and so on. For bacteria with parallel orientations, $\Phi = 1$ (fully correlated), and for bacteria with perpendicular orientations $\Phi = -1$ (anti-correlated). The steady-state time average of the ensemble mean, $\langle\Phi\rangle$, decays exponentially as DoS increases [Fig. 4.21(b)], and the reciprocal of the corresponding decay constant (the coherence length) quantifies local orientational order. Figure 4.21(c) shows that the coherence length increases continuously with γ, and does not show a clear demarcation between the unpercolated and percolated states. However, the trend is clear, and confirms that local alignment does indeed increase with γ, in agreement

with qualitative inspection of the colony snapshots in Figure 4.21(a). We note that the snapshots in Figure 4.21(a) indicate that alignment correlates with high EPS concentration, even though EPS does not cause explicit alignment of neighboring bacteria in our model. Instead, alignment occurs through collisions of rod-shaped bacteria which are confined within the furrows.

The local density distribution also changes dramatically with γ [Fig. 4.21(d)]. At low values of γ, the local density distribution peaks near the global density (N/L^2) of 0.04 (where N and L are the total number of bacteria and the length of the simulation box respectively), as expected for a homogeneous system. Conversely, at high values of γ, the distribution peaks at 0 [corresponding to empty regions between the clusters seen in Figure 4.21(a)], and spreads out to high densities encountered within the clusters. The spreading corresponds to an increase in local density fluctuations (defined as the standard deviation of the local density) which grow systematically from the equilibrium value [indicated by a dashed line in Figure 4.21(e)] as γ increases.

Figures 4.21(d) and 4.21(e) represent density fluctuations for square subspaces of side length 10 μm. However, it is instructive to examine the density fluctuations as a function of subspace area [Fig. 4.21(f)]. Below γ_c, particle number fluctuations scale as $\Delta n \propto \langle n \rangle^{0.5}$ (where $\langle n \rangle = N[l/L]^{-2}$ is the average number of bacteria in a local area of area l^2), as expected for an equilibrium system. Above γ_c nonequilibrium giant number fluctuations (GNFs) are observed and $\Delta n \propto \langle n \rangle^{\lambda}$, with $\lambda > 0.5$ (see Appendix A.2.3 for a detailed description of our local density calculations).

The increase in density fluctuations above γ_c is important with respect to bacterial fitness because it is the high-density tail of the density distribution that corresponds to tightly packed areas where the bacteria will benefit from cooperative processes, and are more likely to withstand perturbation [21].

To investigate the balance between cluster stability and individual mobility, we introduce a novel metric: the configurational correlation, ζ, which is defined as the ratio of the persistence time (τ_1) of a global density distribution to the dwell time

(τ_2) of the constituent individuals. It is a quantitative measure of the rate at which the colony 'morphology' seen in each snapshot of Figure 4.21(a) evolves relative to the rate at which the bacteria within it are moving. A complete description of how we computed τ_1, τ_2 and ζ is provided in Appendix A.4.3.

Plots of τ_1 [Fig. 4.21(g)] and τ_2 [Fig. 4.21(h)] versus γ show, unsurprisingly, that both the global persistence time and and the individual dwell time increase monotonically with substratum stiffness. However, $\zeta(\gamma)$ is approximately constant in the unpercolated and percolated states, and increases continuously with γ in the transition region between the two states [Fig. 4.21(i)]. The transition region, $\gamma_c \leq \gamma \leq \gamma_{sat}$, demarcates a state characterized by dispersed, disordered movement ($\gamma \leq \gamma_c$), from that of a structured collective morphology with high local density and connectivity ($\gamma \geq \gamma_{sat}$). Thus, there exist two ranges of substratum stiffness, corresponding to the two stable states of the colony within which the respective modes of collective movement are insensitive to small changes in γ. The stable states are separated by a rapidly-varying transition region characterized by a high degree of sensitivity to γ.

For $\gamma \leq \gamma_c$, the self-propulsion force of individual bacteria is significant relative to the opposing force exerted by the substratum. Hence, individuals move freely, forming clusters only when random collisions occur [Fig. 4.17(b)], and disperse rapidly due to the stochastic nature of movement driven by type IV pili [see Figure 4.17(c) and the model description]. In this sub-critical regime, path following and stable clustering do not occur because the two stigmergy mechanisms are ineffective – the substratum does not produce robust topographic paths, and the EPS concentration rapidly becomes uniform throughout the system, as is seen in Figure 4.21(a) where the EPS concentration is depicted in green. Hence, movement bias caused by the environment is negligible, and stigmergy does not occur.

As γ increases, the substratum increasingly restricts the motion of individuals, and

the motility bias induced by EPS causes separated individuals to form clusters. Polarity reversals give rise to cluster elongation and allow bacteria to semi-periodically retrace their steps, reinforcing trails that eventually merge, forming the observed network of interconnected channels.

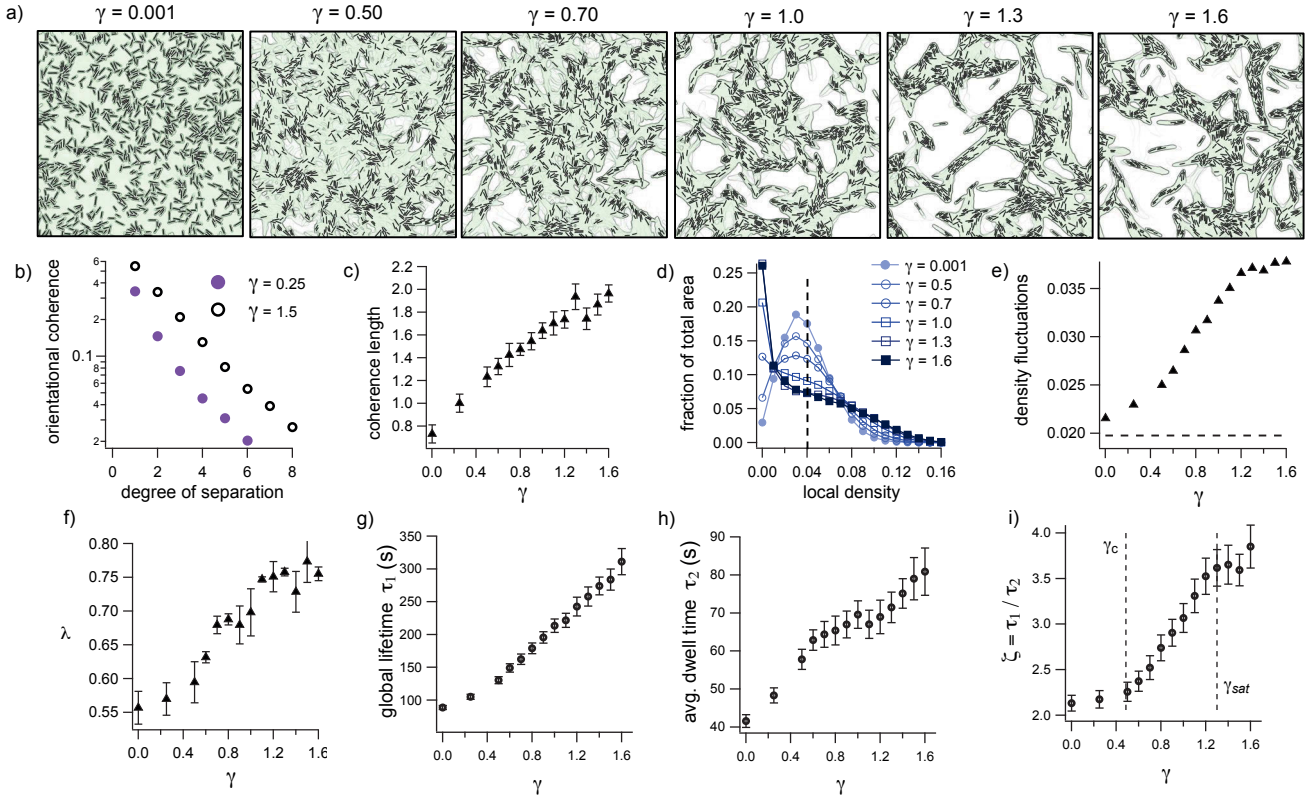

FIGURE 4.21: Steady-state properties of the biofilm versus substratum stiffness γ. (a) Snapshots of the colony superimposed on plots of EPS concentration (shown in green). The local degree of alignment increases with γ. It manifests as an increase in (b) orientational coherence and (c) coherence length versus γ. Clusters form throughout the colony as γ is increased, causing (d) broadening of the spatial density distribution and (e) an increase in local density fluctuations, which correspond to (f) nonequilibrium number fluctuations. (g) The global configuration (i.e., colony morphology) persistence time and (h) the individual bacterium dwell time both increase monotonically with γ. (h) In the percolated state ($\gamma \geq \gamma_{sat}$), the colony morphology is more stable than in the unpercolated state ($\gamma \leq \gamma_c$), relative to the movement rate of the individuals composing it. (i) This indicates percolation in conjunction with path-following. Error bars correspond to (g, h, i) the standard deviation in time, or (c, f) the 95% confidence interval of the fitting coefficient.

4.5 Discussion

Having characterized the transition between the two modes of collective behavior, we first discuss the essential features of this process and the underlying mechanisms. We then discuss how these results help us understand the interplay between biofilm fitness and morphogenesis phenomena reported in experimental studies.

The primary aim of this study was to elucidate the nature of biofilm pattern formation based on the assumptions that the constituent bacteria furrow through the substratum, and excrete EPS which can form trails that bias their motion. We note that, while the model implements two forms of stigmergy (due to furrowing and EPS following), EPS alone can give rise to trail and pattern formation even in the absence of furrowing (e.g., when $\gamma = 0$). However, this is true only in a narrow subset of the parameter space where the EPS degradation and deposition rates are fine-tuned and the pilus binding affinity to the bare surface is close to zero – conditions that are not justified given that the bacteria are known to form furrows in the systems of interest [45], and that T4P are known to bind readily to a large variety of biological and abiotic surfaces [84].

Additionally, low-concentration agar is known to favor 'swarming' or 'swimming' motility through the expression of flagella (see, for example, Refs. [66, 91]), mechanisms distinct from the one we study here. Our simulations of twitching motility are expected to apply in situations where substratum stiffness is high enough to promote the expression of T4P, which makes the substratum stiffness an intrinsic parameter in any realistic scenario involving this type of motility.

While bimodal clustering in systems of self-propelled rods has been attributed to simple steric interactions between particles [38], such a transition is not evident in our model, which is based on stochastic, apolar movement of bacteria as documented by Skerker *et al.* [34]. Indeed, below γ_c the system demonstrates equilibrium behavior, even though the cell density and mean aspect ratio are well within the parameter

space corresponding to nonequilibrium clustering as reported by Peruani *et al.* [38]. The absence of this transition is due to the stochastic nature of particle movement, in particular the discontinuous application of the pilus retraction force, and random polarity reversal (see section 4.2). However, trail following due to substratum deformation effectively facilitates nonequilibrium structure formation, despite the stochastic nature of bacterial movement. Importantly, our results indicate that EPS deposition alone is not sufficient to achieve trail formation.

This result both complements and contrasts that of Balagam and Igoshin, who recently simulated trail following in surface-motile bacteria to explain pattern formation in systems where the constituent individuals spontaneously reverse direction [53]. While they observed that trail following does indeed facilitate nonequilibrium clustering, the authors did not suggest a specific mechanism behind trail following phenomena but invoked the idea of EPS trail following to explain the corresponding experimental observations. Their implementation of trail sensing involved a Monte-Carlo sampling of the area near the forward pole of each cell to determine the trail direction. In our model such a process is analogous to the random sampling of the area accessible to pili. However, because pilus retractions pull the cell a distance on the order of the cell length [34], errors in spatial sampling lead to ineffective EPS trail following. Our results suggest that while EPS excretion plays an important role in morphogenesis by enhancing the movement rate within trails, these trails cannot form without the mechanism suggested by Gloag *et al.*, whereby the bacteria actively remodel the topography of their environment [45]. Without this effect, trail following by the preferential binding of T4P to EPS is not robust.

For the reasons discussed above, we expect our model to exhibit a robust behavioral dependence on γ similar to the one we report here for any set of parameters for which the EPS does not facilitate path following in the absence of a physical resistance to motion. The specific range of γ over which this transition occurs experimentally will be a function of the forces exerted by the bacteria. Therefore, we would not expect to see the emergence of robust trail networks in experiments where the bacteria move

through a medium that is either very soft (negligible γ) or very rigid (negligible k_s), unless the pilus binding affinity is close to zero in the absence of EPS.

Our insights into the role of γ are highly relevant to experimental studies because, whilst EPS following is difficult to manipulate experimentally, the material properties of the culture medium are relatively easy to control and can have an enormous influence on behavior. This indicates that unpredictable behavior of bacterial biofilms in the laboratory may result from subtle differences in culture preparation, and motivates novel studies of the behavioral response of bacteria to systematic manipulation of material properties.

An example of this strategy was recently reported by Ratzke *et al.*, who elegantly demonstrated the trade-off between fitness associated with low- and high-resistance environments for microcolonies of *Bacillus subtilis* (a motile, rod-shaped bacterium) suspended in solidified agar [21]. In low-density media, bacteria were able to move freely into the medium, expanding rapidly and proliferating quickly in high-nutrient conditions, while their counterparts grown in high-nutrient, high-density agar were not able to expand rapidly and formed dense patches. In low-nutrient conditions, however, the advantage was given to the high-density, slow-moving structures which were able to survive due to a cooperative metabolism process that was only possible in dense patches. These findings suggest a mutual exclusivity separating high-mobility and high-density structures.

Our results show how stigmergic processes can combine these two fitness advantages in the high-density condition. Cooperative movement processes and trail formation produce a system in which the individuals can move effectively within a densely connected structure that maintains the benefits of the biofilm without inhibiting spatial proliferation.

4.5.1 Conclusion

We have demonstrated how slight alterations in environmental conditions can lead to dramatic changes in collective motion patterns of bacteria, even when all biological parameters are fixed. The observed behavioral transition is facilitated by an interplay between two stigmergic processes. The first is biological: the bacteria actively store spatial information in the local environment in the form of excreted substances. The other is physical: spatial information is stored due to deformation of the material through which the bacteria move. The physical mechanism offers an opportunity to understand and control the behavior of bacteria without modifying their biology. Our results emphasize the essential role of agent-environment interactions in models of emergence in multi-agent systems, particularly when the environment is not static, and is modified by the activity of the agents moving within it.

Many assumptions are made in this model, which from the biological perspective appears simplistic. Indeed, it does not explicitly model any metabolic processes or complex phenomena such as cell-cell communication and adaptation. In other words, the biological state of the system is simplified, and is considered fixed for the purposes of the investigation.

The model is highly idealized from the physical perspective as well. For example, the 2D system excludes the many cell arrangements that can only be accounted for in 3D, a property that is only applicable in the case of interstitial biofilms. The complex viscoelastic interaction between the bacteria and their environment is reduced to a simple deformation potential, a phenomenological treatment that does not capture the subtleties of these processes. However, our intention here is to strike a balance between detailed models of biological, physical, and minimal (behavioral) models. Our model has elements of each of these and can be expanded in detail while still maintaining its connection to general theories of emergence in systems of self-driven individuals.

Chapter 5

Growing Biofilms

5.1 Preamble

The following two sections contain material from the article *Network patterns in exponentially growing 2D biofilms* (in review), with coauthors Xinhui Yap, Erin S. Gloag, Cynthia B. Whitchurch, and Milos Toth [98]. The manuscript content has been incorporated into a wider discussion of bacterial growth model variants.

5.2 Growth and motility

5.2.1 Introduction

In sections 4.2, 4.3, and 4.4, the results required a fundamental assumption that affects the biological, physical, and minimal description of this system: fixed cell density. In reality, biofilms are composed of cells that grow and divide. All systems of self-driven particles are thermodynamically nonequilibrium, that is, they require an energy source to fuel active particle movement. However, steady-state properties can be assigned under the assumption that, for example, energy conversion into

motion occurs at a constant rate. In the present case this condition means the retraction rate, retraction force, and population are constant on average. In sections 4.2, 4.3, and 4.4 the results consisted of these steady-state properties, which can only be measured after some interval over which the system transitions from its random initial condition to its steady state. The results (number fluctuations, structural correlation coefficient etc.) are therefore time-independent assuming the rules defining the behavior of individuals remain fixed. While this state of affairs is convenient for a quantitative description of the system, its time-independence ignores an extremely important component of morphogenesis. Whereas in the previous section the bacteria did not grow, in the sections to follow the bacteria elongate and self-replicate.

In this section, the model of individual growth and cell division discussed in section 3.3.2 is incorporated into the behavior of motile and nonmotile bacteria. The rate of self-replication defines a fundamental timescale that morphogenesis must compete with in order for pattern formation to occur. Neglecting both forms of stigmergy discussed in sections 4.3 and 4.4, I will demonstrate that motility and growth alone do not produce anisotropic pattern formation. On the contrary, motility without stigmergy facilitates isotropic spatial configurations due to diffusive mixing and buckling [99].

5.2.2 Exponential growth

As discussed in sections 3.2 and 3.3.2, we consider a situation where nutrient depletion is negligible and the bacterial growth rate is not retarded in the colony interior. Cell numbers therefore increase exponentially as growth and division take place.

As in sections 4.2, 4.3, and 4.4, individual bacteria are simulated as self-propelled, capped rods that undergo repulsive collisions with one another [Fig. 5.1(a)]. The cells elongate at a constant rate g and divide [Fig. 5.1(b)] at a critical length $l_{max} = 7\ \mu$m

into two cells each with length $l_{min} = 3\ \mu\text{m} \pm \delta l$. The parameter δl represents asymmetric division and is randomly selected at the time of division from the uniform interval $\delta l \in [0, 1]\ \mu\text{m}$. The implementation of motility used here is identical to that used in the previous sections [Fig. 5.1(c)], but neither stigmergy mechanism (marker-based or sematectonic) is included here.

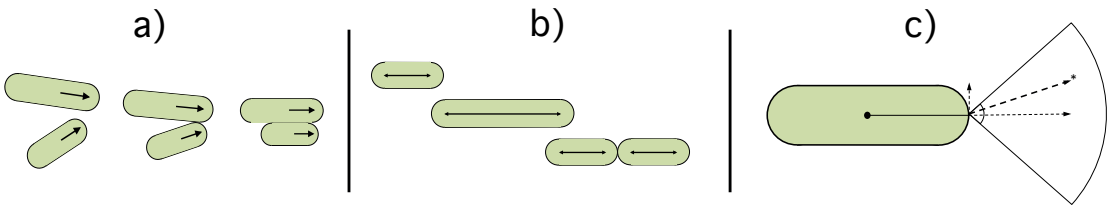

FIGURE 5.1: Rules of the behavioral model employed in this section. (a) Cells interact via repulsive collisions (see Appendix A.2.1). (b) Cells elongate and divide after reaching a critical length. (c) T4P motility is implemented as described in section 4.1.

5.2.3 Isotropic expansion

To demonstrate the effects of growth and motility on colony morphology, I ran simulations using the following parameters:

- linear elongation rate, $g = 0.001$
- uniform attachment probability, $P_a = 0.1$ (motile)
- uniform attachment probability, $P_a = 0$ (nonmotile)

With respect to colony morphology, there is a 2D expansion rate determined by the elongation rate of the cells. If expansion occurs only due to cell growth, division, and physical pushing, the colony area $A(t)$ increases exponentially in time:

$$A(t) = A_o e^{k_g t}\,, \tag{5.1}$$

$$k_g = \frac{g}{\Delta l}\ln(2)\,, \tag{5.2}$$

where A_o is the area occupied by the innoculation and Δl is the length gained between division events, making $\frac{\Delta l}{g}$ the doubling time.

The radius corresponding to the colony edge obeys:

$$r(t) \propto \sqrt{e^{k_g t}}\,, \tag{5.3}$$

Which also holds for the average displacement from the colony center of mass $\langle r \rangle$ [Fig. 5.3(a)]. This expansion model (Eqn. 5.3) only applies if the colony has a radially uniform (isotropic) density distribution. The spatial uniformity of the density distribution can be quantified by calculating ΔS_ϕ, derived from the entropy of the

distribution over k bacteria of the polar coordinate ϕ_i ($i \in \{1, 2, 3, ...k\}$) describing the vector between particle i's position and the colony center of mass. This calculation is identical to that which I applied to the entropy of the distribution of particle orientations in section 4.1 to determine the orientational decoherence time τ_θ. Here we apply it to the positional coordinate ϕ_i instead of the individual orientation θ_i (see Appendix B.1.1 for details of ΔS_ϕ calculations).

For colonies of nonmotile cells, the initial configuration is anisotropic [Figs. 5.2(a) and 5.3(d)]. As cell numbers increase, the configuration becomes isotropic. This occurs as the radius of the colony [Fig. 5.3(b)] exceeds the orientational correlation distance r_Φ. This distance r_Φ is defined as the radius at which the ensemble average of the orientational coherence value Φ as a function of radius [Fig. 5.3(d)] vanishes [i.e., $r(\langle\Phi\rangle = 0)$]. The transition from anisotropic to isotropic corresponds to the point at which $\langle r(t)\rangle$ matches the exponential model described by Eqn. 5.3. This is shown in Figure 5.3(a) as agreement of the simulation model data (black circles) and exponential growth model (red dashed line). [The calculation of $\langle\Phi\rangle(r)$ is identical to that used for $\langle\Phi\rangle(DoS)$ as described in section 4.4.8 and Appendix A.4.2, except that metric distance r is used instead of the degree of separation (DoS).]

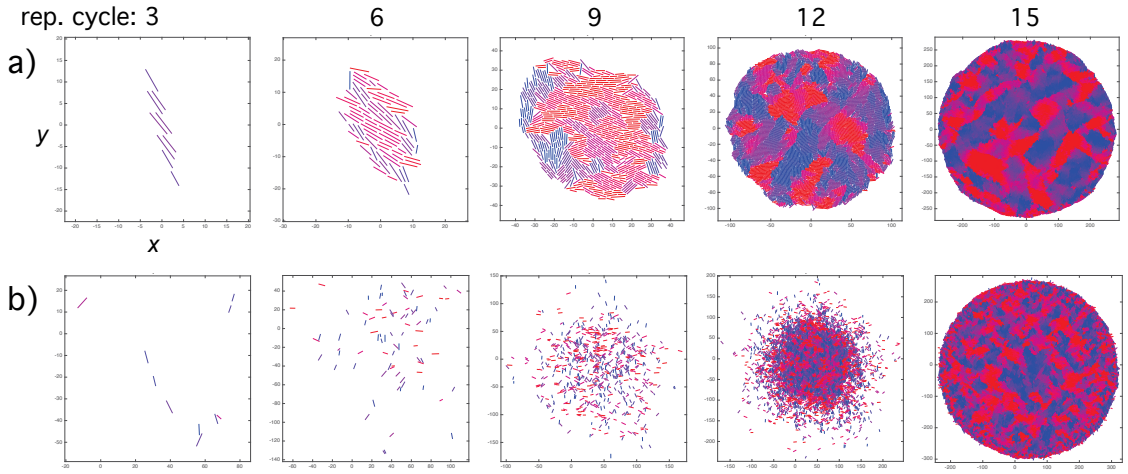

FIGURE 5.2: Colony morphology as a function of replication cycle. After 15 replication cycles, colony morphology of (a) nonmotile, and (b) motile bacteria is isotropic. Each bacterium is colored with respect to its apolar orientation (red for horizontal, blue for vertical). Larger patches of cells with similar orientations in the colony of nonmotile bacteria (a) indicate they have longer coherence length than their motile counterparts (b).

To summarize, exponential growth of nonmotile rod-shaped bacteria begins with a brief phase of anisotropic growth due to the fundamentally anisotropic initial condition of a single growing cell. This is followed by isotropic expansion as cell numbers increase and collisions between them lead to orientational decoherence (i.e., buckling instability [99]) [Fig. 5.2(a)]. After this point, the radially averaged coverage distribution as a function of distance from the colony center of mass $\eta(r)$ is isotropic and of uniform magnitude $\eta(r) \approx 1$ [Fig. 5.3(b)]. $\eta(r) > 1$ occurs due to compression of cells in the interior of the colony.

When motility is included in this model the bacteria initially diffuse, the density is low, and collisions infrequent [Fig. 5.2(b)]. If repulsive interactions are ignored, and expansion of the colony edge occurs only due to individual motility, it should obey:

$$r(t) = \sqrt{Dt}\,, \tag{5.4}$$

where D is the diffusion coefficient as established in section 4.1. During this diffusion-dominated period of colony expansion, the average displacement from the center of mass $\langle r(t) \rangle$ obeys Equation 5.4 [Fig. 5.3(a), black dashed line]. During the diffusive period, the colony density profile resembles a Gaussian distribution. It then saturates towards the center of the colony at later time points as the close-packed state is reached [Fig. 5.3(b)]. After this diffusive period $A_o\sqrt{e^{kt}} > \sqrt{Dt}$, and exponential expansion overtakes diffusive expansion [Fig. 5.3(a)]. The bacterial density profile then resembles that of the nonmotile case [Fig. 5.3(b)].

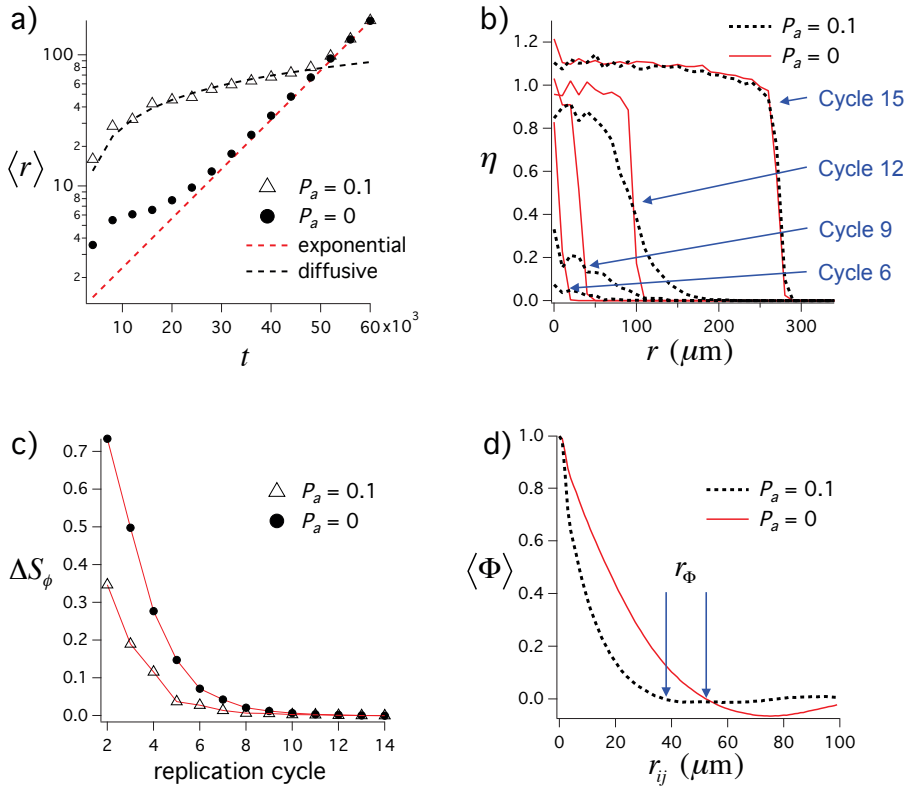

FIGURE 5.3: Characteristics of growing bacterial colonies. (a) The average distance from colony center of mass as calculated for simulations of bacteria that are motile (triangles) and nonmotile (black circles) plotted with the exponential and diffusive growth models (red and black dashed lines, respectively). (b) For the indicated replication cycles, the coverage fraction η is plotted as a function of radius from the colony center of mass for bacteria that are motile (black dashed line) and nonmotile (red line). (c) The anisotropy ΔS_ϕ of the radial density distribution plotted against replication cycle for bacteria that are motile (triangles) or nonmotile (black circles). (d) The average orientational coherence $\langle\Phi\rangle$ as a function of neighbor distance r_{ij} at t_f for bacteria that are motile (black dashed line) or nonmotile (red line). The arrows in (d) indicate the orientational correlation distances r_Φ.

During the initial diffusive phase, the system of motile bacteria lacks the spatial anisotropy of the nonmotile colony because the bacteria move randomly [Fig. 5.3(c)]. Because the cell orientations randomize due to diffusion, the orientational correlation distance is lower when the close-packed state is reached than it is in the nonmotile case. This difference in orientational coherence length is reflected in the internal

structure of the colony as seen in snapshots [Fig. 5.2(b)], where the constituent bacteria are colored by orientation. Therefore, motility facilitates isotropic expansion due to diffusive mixing in the dilute configuration. Additionally, enhanced buckling caused by motility forces may contribute to reduced coherence length in the dense phase.

5.2.4 Conclusion

In this section, I included the basic phenomenon of cell growth and division within the biophysical framework discussed in section 4.2. This was followed by a brief exploration into the behavior of 2D biofilms composed of motile or nonmotile bacteria. Both cases resulted in isotropic colony morphology. The following section introduces stigmergy into this model of colony expansion and focuses on a discussion of how stigmergy can facilitate the formation and propagation of anisotropic conditions. Such effects lead to agreement between model results and experimental observations.

5.3 Propagating anisotropy

Note: this section is derived exclusively from the manuscript *Network patterns in exponentially growing 2D biofilms* by C. Zachreson *et al.* (in review) [98]. Minor modifications have been added referencing other parts of the thesis containing relevant data. Figures and text have been modified to remove redundancy with previous sections.

5.3.1 Introduction

Anisotropic collective patterns occur frequently in the morphogenesis of 2D biofilms. These patterns are often attributed to growth regulation mechanisms and differentiation based on gradients of diffusing nutrients and signaling molecules. Here, we employ a model of bacterial growth dynamics to show that even in the absence of growth regulation or differentiation, confinement by an enclosing medium such as agar can itself lead to stable pattern formation over time scales that are employed in experiments. The underlying mechanism relies on path formation through physical deformation of the enclosing environment.

In surface-associated bacterial colonies, growth regulation caused by a diffusion-limited nutrient supply has been suggested as a primary mechanism of pattern formation, resulting in branched, locally anisotropic morphologies [8, 42]. However, diffusion-limited growth does not tell the whole story. Mechanical processes are known to play essential roles in morphogenesis [100], and we show here that deformation of the enclosing environment by moving bacteria can lead to the emergence of persistent, stable, anisotropic network patterns such as those in Figures 3.3(a) and 3.3(b) even under conditions of exponential colony growth.

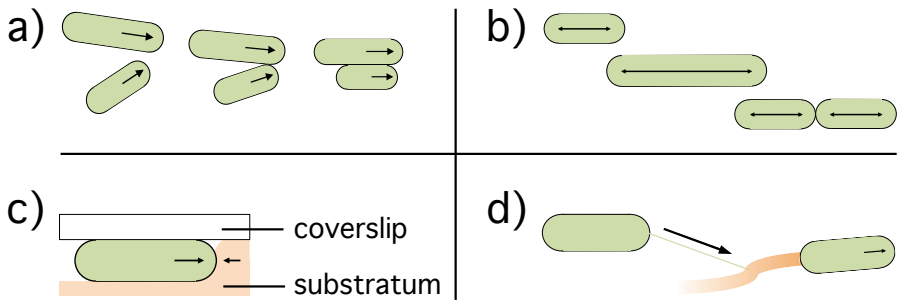

FIGURE 5.4: Schematic illustrations of the processes comprising the model of bacterial behavior implemented in this section. (a) Repulsive collisions between motile cells. (b) Cell elongation and division. (c) Furrowing: topographical modification of the substratum (sematectonic stigmergy). (d) EPS trail following (marker-based stigmergy).

Previously, Gloag *et al.* observed that these bacteria can deform the soft enclosing material through which they move, and confinement in the resulting 'furrows' appears to contribute to network pattern formation [45]. However, *P. aeruginosa* and many other surface-motile bacteria move through the extension and retraction of type IV pili [34, 69], which have increased binding affinity to extracellular polymeric substances secreted by the moving bacteria [67], a phenomenon that has also been suggested to result in trail following behavior [54, 55]. To investigate the relative importance of these two processes in the emergence of the observed network morphology, we carried out simulations of motile bacteria that interact with the hydrogel environment. The behavioral rules implemented in our simulations are illustrated in Figures 5.4(a-d). Each simulation was initiated with a single motile, growing cell, and terminated after 12 cell division cycles ($t_f = 1.37 \times 10^5\ s$). Our results verify the importance of hydrogel properties in interstitial biofilm morphogenesis. By increasing the substratum stiffness in our model, colony morphology was altered in qualitative agreement with experimental results obtained by increasing hydrogel monomer concentration (Fig. 5.5). [See [78] for details on the interstitial biofilm culture techniques used to produce the data in Figures 3.3(a), 3.3(b), and 5.5(d-f).]

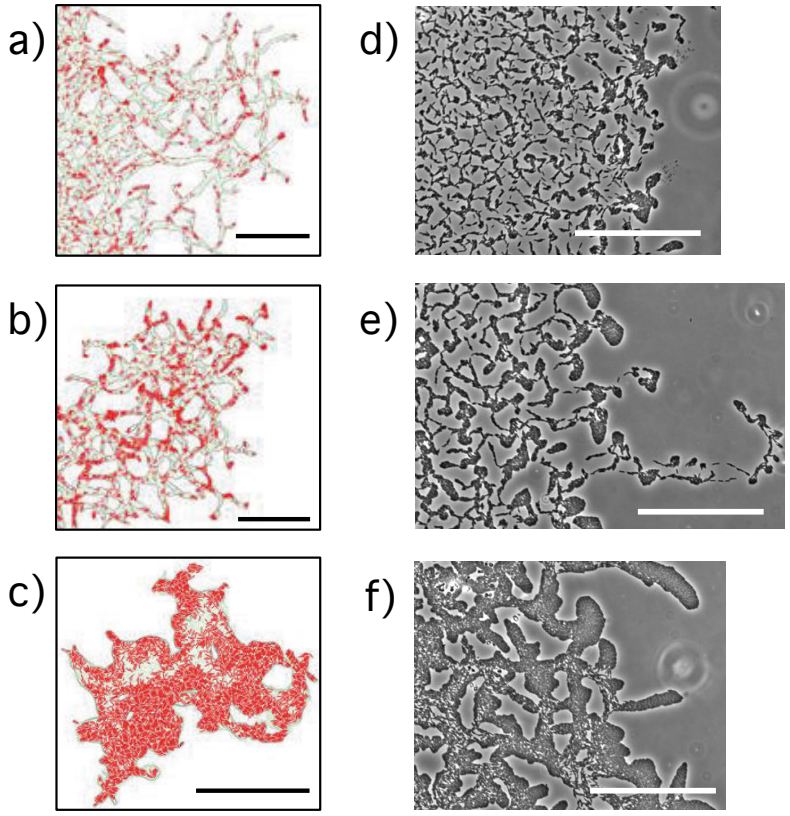

FIGURE 5.5: Snapshots of three biofilms simulated by the model with substratum stiffness coefficients of $\gamma = 0.25, 0.5, 1.0$ [(a), (b), (c), Supplemental Movies S5, S6, and S7 (Appendix C.3), respectively], illustrating the cell positions (red), EPS trails (green) and furrows (gray outline). The simulations show qualitative agreement with experiments performed using hydrogel monomer (gellan gum) concentrations of $0.5\%, 0.8\%$, and 1.2% [(d), (e), and (f) respectively]. Scale bars represent 100 μm.

Bacterial behavior emerges from a complex interplay of many nonequilibrium and stochastic processes. Isolation of factors that are fundamental to morphogenesis mechanisms requires a model that describes the complexity of the real system, with an experimentally constrained parameter space. Here, we focus on the processes of cell growth and motility as the fundamental model ingredients. The essential properties of the system that cannot be estimated *a-priori* relate to bacterial movement dynamics and individual growth rates. We therefore designed our biophysical model so as to enable incorporation of experimentally determined time-scales into these processes.

5.3.2 Model summary

The model used here is similar to one described in section 4.4, except that it includes cell growth and division. The individual growth rate used here ($g = 3.5 \times 10^{-4}\ \mu\text{m}/s$) was estimated from our experimental measurements, as described in section 3.3.2 and detailed in Appendix D [Fig. 3.3(d)].

A similar model of motility bias due to EPS secretion was published recently [54, 55]. However, our model explicitly simulates the stochastic process of pilus binding and retraction [92], instead of making a mean-field approximation based on the assumption of a large number of T4P per cell. Based on available literature, such an assumption may not be valid for *P. aeruginosa* [34]. This apparently subtle difference is significant because our findings suggest that the stochastic nature of T4P binding and retraction yields ineffective following of EPS trails that is not robust in the absence of furrowing. This is exemplified by Figure 5.6(a), which illustrates a typical colony morphology in a case where physical interactions with the substratum are weak. In such a case trail networks could, in principle, emerge exclusively via the EPS stigmery mechanism but do not, making the EPS phenomenon alone unlikely to account for network formation in *P. aeruginosa*, as discussed in more detail in section 4.3.

5.3.3 Results

Because the furrowing process is governed by the substratum deformation rate k_U and stiffness γ, these parameters control the path formation rate and degree to which cells are confined to the paths, respectively, making them critical to this stigmergy mechanism. To investigate their roles, we simulated bacterial growth under various environmental conditions defined by k_U and γ, and recorded the colony configuration (cell positions, lengths, and orientations) at 20 s intervals.

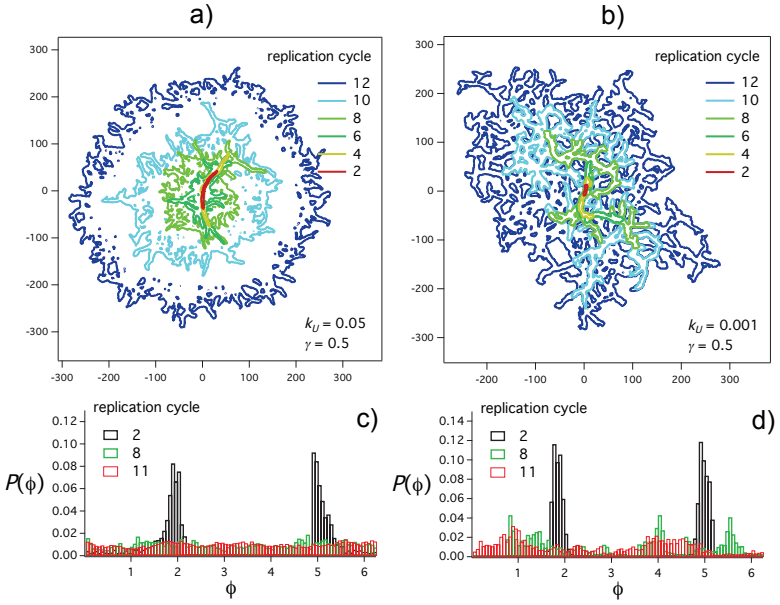

FIGURE 5.6: (a, b) Colony outline (defined as the area over which $C_s \neq 0$) plotted after a number of cell replication cycles on soft (a) and hard (b) agar [Supplemental Movies S8 and S6 (Appendix C.3), respectively]. (c, d) Histograms of polar coordinates ϕ of the constituent bacteria integrated over the indicated replication cycles for soft (c) and hard (d) agar.

We start by noting that unregulated exponential growth eventually out-paces all other processes in the model and acts to homogenize the colony morphology as $t \to \infty$ (see section 5.2). However, on the time scales probed in typical experiments, the colony can rapidly become isotropic [Fig. 5.6(a)] or it can grow in a network [Fig. 5.6(b)], depending on the values of k_U and γ. The changes in colony morphology during growth seen in Figures 5.6(a) and 5.6(b) correlate with changes in the radial distribution of cells around the colony center of mass [Figs. 5.6(c) and 5.6(d)], which transitions from a multimodal to a uniform distribution as the colony grows from a single cell moving back and forth in the hydrogel to become isotropic.

The entropy of such radial distributions as a function of length scale provides a metric of local anisotropy in the density distribution, a signature of the network morphology observed in experiment [Figs. 3.3(a) and 3.3(b)]. Our anisotropy parameter $\Delta S_\phi(r)$ reflects the entropy of each distribution relative to that of the uniform distribution. ΔS_ϕ takes a value of 1 for a 1D density distribution and approaches 0 for an isotropic

(circular) distribution (see Appendix B.1.1 for details of ΔS_ϕ calculations). We included the coordinates of every cell throughout a given replication cycle in the measured configurations so that radial anisotropy was observed only if it was stable on the timescale of population doubling. Averaging the result of $\Delta S_\phi(r)$ around the positions of $N = 1000$ randomly selected cells from such a time-integrated configuration gives an estimate of how spatial anisotropy scales as a function of distance r away from any given cell. Plots of ΔS_ϕ as a function of r for the 11th replication cycle show how anisotropy can persist under some conditions (Fig. 5.7).

Three different types of pattern emerge as the parameters defining the mechanical properties of the substratum are varied. There are two qualitatively distinct isotropic types, and a network morphology similar to the one observed in experiments. Dense configurations become isotropic due to buckling [99] [Fig. 5.7(a), $\gamma = 1.5$], while dilute configurations give isotropic diffusive behavior [Fig. 5.7(b), $\gamma = 0.25,\ 0.5$].

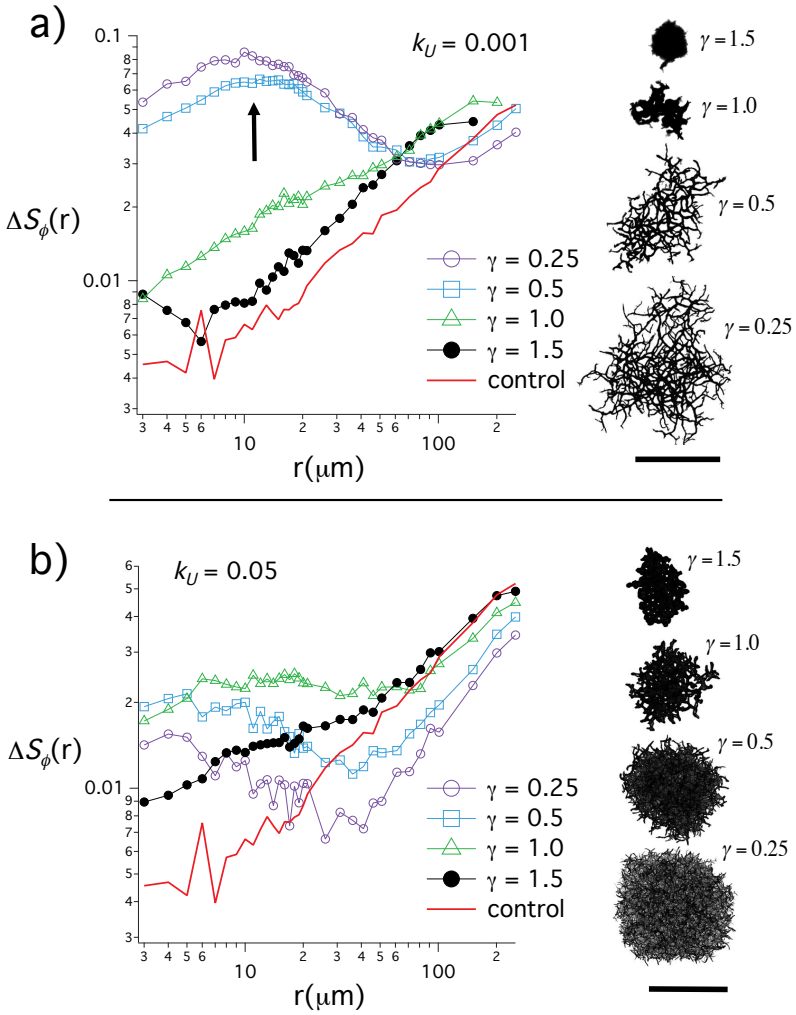

FIGURE 5.7: Plots of $\Delta S_\phi(r)$ and corresponding colony morphology after 11 division cycles simulated for values of $\gamma = 0.25, 0.5, 1.0, 1.5$, and $k_U = 0.05$ (a) and $k_U = 0.001$ (b). The red curves represent $\Delta S_\phi(r)$ for an isotropic, uniform random configuration of 150 μm radius. The arrow emphasizes a peak at low r that corresponds to local anisotropy due to network morphology. The scale bar represents 400 μm.

Due to mechanical constraint from the substratum, movement of the initial bacterium is either negligible or quasi-1D due to resistance to orientational and translational movement. As cell numbers increase, this 1D confinement facilitates collisions between cells that produce enough force to change cell orientations, causing branching. The dense configuration occurs when motility cannot out-pace volume expansion due to population growth [Supplemental Movies S7 and S9 (Appendix

C.3)]. The diffusive mode corresponds to the situation where collisions between small numbers of cells are sufficient to overcome the orientational resistance applied by the substratum. In this case, branching occurs readily in arbitrary locations within an existing trail and the system becomes isotropic as branches interlink [see Movie S8 (Appendix C.3)].

Network morphology occurs in the intermediate case, where collisions between larger numbers of cells are required for branching. EPS trails give rise to cluster formation at the ends of furrows because the movement rate within the trail is faster than at the ends. This encourages branching at the trail tips and leads to trail elongation and cluster formation at the edge of the colony, allowing expansion to out-pace growth due to cell division for extended periods of time [Supplemental Movie S6 (Appendix C.3)]. If EPS deposition is ignored and the attachment probability P_a is uniform, this condition cannot be met. In this case, qualitatively different trail-network patterns are possible [Figs. 5.8(c) and 5.8(d)] that evolve from a randomly diffusing state due to the amplification of fluctuations in surface topography [Supplemental Movie S10 (Appendix C.3)]. These patterns are distinct from those formed by *P. aeruginosa*.

5.3.4 Results of model variants lacking EPS

To detail the role of EPS in colony morphogenesis, we ran simulations using a model variant that lacks EPS deposition. Without EPS, pilus attachment probability P_a is uniform throughout the simulation space. In this case (for fixed motility parameters as described in the model description in our earlier work [92]) colony morphology depends only on γ, k_U, and P_a. We tested the model's behavior for $\gamma = 1.5, 1.0, 0.5, 0.25$, $k_U = 0.05, 0.001$, and $P_a = 0.5, 0.25$. Figure 5.8 shows results for $P_a = 0.5$. A unique morphology was observed for $\gamma = 0.5$ and $k_U = 0.001$ [Fig. 5.8(a) $\gamma = 0.5$]. Long, tapered trails with high cell density emerge near the

colony interior, surrounded by a subpopulation of diffuse cells that move independently. Examination of the morphogenesis process [Supplemental Movie S10 (Appendix C.3)] reveals a pattern formation mechanism distinct from that involving the effects of EPS [Supplemental Movies S5, S6 (Appendix C.3)], as described in the main text.

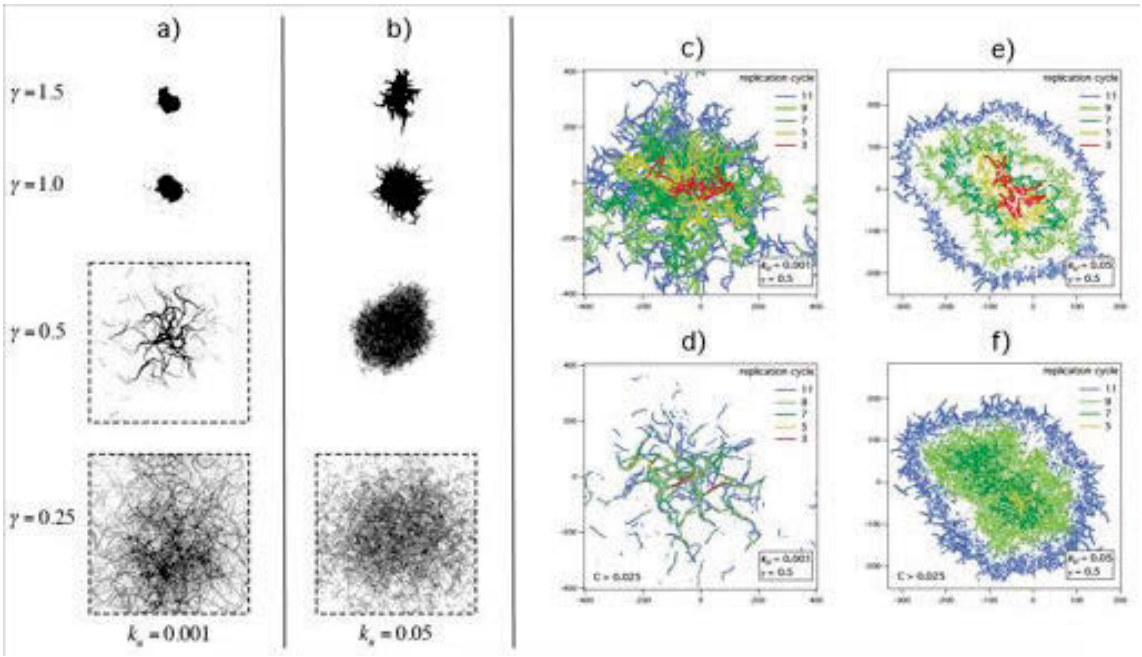

FIGURE 5.8: Colony morphologies simulated by the bacterial biofilm model without EPS deposition for constant surface attachment probability $P_a = 0.5$. Surface topography after 11 replication cycles shows dense, dendritic, network, and diffusive morphologies, depending on the substratum parameters γ and k_U (a, b). Dotted boxes indicate simulations where bacteria crossed the periodic boundaries before t_f. Contour plots (c-f) show areas of substratum deformation where $C_s > 0$ (c, e) and $C_s > 0.025$ (d, f) for the indicated replication cycles and substratum parameters.

This process occurs as follows: if the individual movement rate (as dictated by the attachment probability) is fast enough that the cells move before 'sinking' into the substratum, they initially diffuse over the surface. Due to the stochastic nature of pilus binding and polarity reversal, the cells will at some point stop moving long enough to create a substantial depression in the substratum, trapping them in position. There, they slowly move back and forth, elongating the depression in the

substratum while also growing and dividing. This process results in the observed elongated, tapered clusters that merge together to form the resulting dense network. The contour plots in Figure 5.8(c) illustrate how the tracks of the freely diffusing cells traverse the simulation space freely while Figure 5.8(d) illustrates how the network morphology coexists with the diffusing sub-population and remains confined to deep depressions in the substratum.

If the deformation rate is too fast [Figs. 5.8(b), 5.8(e), and 5.8(f)], or if the attachment probability is lower (i.e., when $P_a = 0.25$, not shown), cells sink too quickly to diffuse over the surface, favoring either an isotropic, dilute phase (if the substratum resistance is low) or a dense, dendritic phase if the substratum resistance is high enough to prevent individuals from escaping the expanding colony boundary.

Of course, even in the presence of EPS such morphologies could be expected if the affinity of pili to the unaltered surface was on the order of the constant attachment probability necessary for the formation of the patterns shown here. Therefore, EPS allows network formation to occur in conditions where the surface on which the bacteria are moving has a low affinity to T4P, and facilitates this process through a mechanism that is qualitatively distinct from that which occurs in its absence.

5.3.5 Conclusion

To conclude, we have simulated biofilm growth to explain how network morphogenesis in expanding bacterial colonies arises from an interplay between mechanical confinement and enhanced motility due to EPS deposition. These patterns emerge despite the tendency for exponentially growing colonies to expand isotropically. Moreover, their formation does not require chemotaxis, contact-based signaling, surface adhesion between cells, or EPS-mediated nematic alignment.

Chapter 6

Conclusion and Outlook

6.1 General summary

In this chapter I will summarize my findings, and discuss the wider significance of this work. I will then provide some possible future directions with the aim of applying the existing model to the design of novel experiments and medical surfaces.

I have presented a conceptual model of bacterial behavior and implemented it in computational simulations of stigmergy in *P. aeruginosa*. The conceptual model is not unique. All the phenomena included are based on experimentally observed behaviors. What is unique about this work is the way in which the known bacterial behavior was implemented in the simulations. To our knowledge, it is the first model of bacterial surface motility to make explicit the mechanism of bacterial movement. The results have provided insight into how the time and space scales of cellular motility mechanisms limit and constrain the behaviors of collectives. These insights have identified several key aspects of bacterial motility as potential targets for biological control over collective behavior (i.e., the polarity reversal period and T4P retraction frequency). Perhaps more significantly, the model has shown how subtle variations in environmental parameters such as surface charge (attachment

probability, P_a), frictional resistance (μ), and substratum stiffness (γ) can dramatically alter the behavior of bacterial collectives. These insights can help guide the design of medical surfaces that control the microorganisms inhabiting them [74].

In this sense, our work contributes to a new way of thinking about preventing and managing infection. The conventional approach of targeting individual bacteria with toxic antimicrobials has given rise to widespread antibiotic resistance, which presents a global risk to human health [101]. In biofilms, the collective properties of bacteria are key to antimicrobial resistance mechanisms that make biochemical assault ineffective [102]. However, it is becoming clear that biochemical assault is not the only way to control bacteria. Surface designs are being tested that target the physical properties of individuals or collectives, to inhibit biofilm formation [73] or regulate collective growth [74]. These strategies do not apply selection pressure to the bacterial population by killing individuals, and are therefore likely to be better long-term solutions for regulating bacterial populations. Unfortunately, there are few successful examples of these approaches, and their effectiveness in clinical environments has not yet been tested. Effective simulation techniques can help expand the scope of these studies by screening surface designs *in-silico*. To do so, they must be realistic as well as efficient.

6.2 Future directions

While this work has demonstrated the potential of the model to account for emergence in bacterial collectives, it is still limited to bacteria with rigid bodies, and is only implemented in 2D. A few immediate extensions of the existing model could increase its predictive capacity in design of medical surfaces. In the current implementation, the ability to explicitly account for interactions between bacteria and their environment is limited by the 2D implementation, making it impossible to simulate structures taller than an individual cell. Furthermore, the rigid-body treatment

of individual cells precludes its application to longer bacteria that bend in response to an applied force. The model of cell flexibility introduced by Balagam and Igoshin could relax this limitation [53].

Properties like the motility mechanism cannot necessarily be directly generalized to diverse species of pathogenic bacteria. For bacterial simulations to find application in device design, the microbiology and modeling communities must cooperate to increase the number of bacterial species for which realistic behavioral models exist. The modeling community must work directly with experimentalists to facilitate the design of these models, as we have in this work.

One of the factors preventing wide-spread collaboration is the lack of a common language and tool set within the modeling community. Initiatives such as CellModeller [103] and iDynoMics [104] have the potential to provide this. Both projects are in their early stages, but aim to provide efficient and flexible software design for the implementation of different behavioral models within a common framework. While the model presented in this work was tailor-made for the investigation of stigmergy in *P. aeruginosa*, the simple implementation could be incorporated into other simulation platforms.

Even with the fastest computers and the most efficient software, the vast numbers of individuals within bacterial communities makes the agent-based simulation of mature bacterial colonies impossible. The only way to do simulations on such scales is with a continuum description. Agent-based approaches can act as a bridge between the mechanistic details elucidated in experiments and the continuum equations. In such equations, the collective properties of the bacteria are captured by local state variables such as density, degree of orientational order, and particle flux [105]. The predictions of continuum models could be tested against individual-based models and refined accordingly.

Another possible approach to increasing the scale of agent-based models is to use superindividuals. As discussed in Chapter 2, superindividuals represent clusters

of true individuals and their interactions are more difficult to define. However, the emergent properties of clusters can be quantified with individual-based models. Such data could guide the development of cluster interaction models and make the superindividual approach feasible.

The prospect of developing a standardized methodology for designing multi-scale bacterial behavior models is very attractive. The potential application of such models in medical device design, and the fascinating physical properties of these systems, promise an expanding scientific interest in the years to come.

Appendix A

Supplement to Chapter 4

A.1 Supplement to section 4.1

A.1.1 Code summary: individual behavior

The source code used for simulation of individual behavior and determination of diffusion constants D and orientational decoherence time τ_θ as functions of T_{rev} and P_a, can be found here [106], in the following MATLAB (.m) scripts:
twitching_rods_rand_wlk_D_vs_P.m
D_vs_t.m

A.1.2 Numerical estimation of ΔH_{min}

The entropy of a finite probability distribution over n possible states is minimized when the distribution is uniform (all states have equal probability). Using the definition of entropy from information theory: $H = \sum_{i=1}^{n} p_i \ln p_i$, the entropy of an ideal uniform distribution $H_u = \ln n$. However, if a finite number k of samples are taken from a uniform distribution, the distribution of these over the n possible states

will not be precisely uniform and will have entropy $H > H_{min}$. Because this work considers finite populations, I determined the expectation value for H_{min} empirically by calculating the entropy of finite samples from a uniform distribution.

The entropy of finite, uniform distributions of k samples over n bins was estimated by calculating the entropy H of the distribution: $H(n,k) = \sum_{i=1}^{n} p_i \ln p_i$, where i denotes one of n discrete bins in the histogram, and p_i is the probability of finding one of k samples in the ith bin. ΔH (Eqn. 4.4) was calculated for 1000 random samplings from a bounded uniform distribution for systematically increasing values of $\frac{n}{k}$ and n. The resulting average, $\langle \Delta H(n,k) \rangle$ was plotted against the number of bins, n and that data used to parameterize a function of the form $\frac{n}{k}[An^b + c]$. The resulting fit coefficients were used to estimate the minimum expected entropy ΔH_{min} (the expected entropy of a uniform distribution) for arbitrary values of n and k.

The source code for these calculations can be found in the github repository associated with this thesis [106], in the following MATLAB (.m) files:

entropy_tests_3.m
S_dist.m
dS_vs_n_fittype.m

A.2 Supplement to section 4.2

A.2.1 Implementation of repulsive interactions

To model the repulsive force of collisions between cell walls, we employ a Lennard-Jones potential that yields repulsion when the distance between cells is smaller than the rod width ($d_{ij} < w$). The force $\vec{F}_{ij}$ acts along $\hat{\mathbf{r}}_{ij}$, where $\hat{\mathbf{r}}_{ij}$ is a unit vector defined by the closest points between cell centerlines (Fig. A.1). $\vec{F}_{ij}$ also generates

torque of magnitude $\tau_{rep} = [\vec{F}_{ij\perp}][r_{lev}]$, where r_{lev} is the lever arm distance and $\vec{F}_{ij\perp}$ is the component of the interaction force perpendicular to the long axis of the cell.

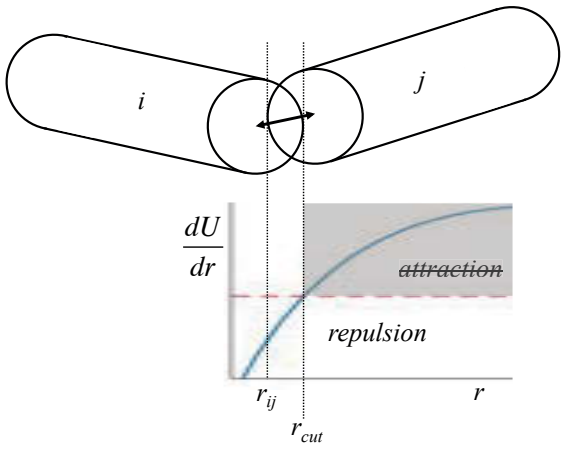

FIGURE A.1: (a) The physical repulsion scheme used to resolve collisions. Force is generated when bacteria overlap, and is applied along the vector connecting the closest points of their respective centerlines. The force is calculated from the repulsive part of a Lennard-Jones potential, defined so that the force $\frac{dU}{dr} < 0$ when $r_{ij} < w$. A distance threshold $r_{cut} = w$ is applied so that the potential is only evaluated when bacteria overlap.

We used the Vega-Lago algorithm to find distances between cell centerlines [107]. We note that the FORTRAN code provided in [107] contains an error that causes the algorithm to fail for parallel rods of different length, which we corrected in the current implementation. We also used a cell-sorting algorithm (side length $l_{max} + w$) and neighbor lists to efficiently find the distances between individuals. $|\vec{F}_{ij}|$ is calculated from the repulsive component of the potential only. The scaling of the repulsive force is given by F_r which is the maximum value reached by the attractive portion of the first derivative of the potential. Though the attractive part is ignored, this value adjusts the scaling of the repulsive region, so that a higher value of F_r yields stronger repulsion.

We used Eulerian integration to calculate changes in cell positions. The time step Δt is continuously adjusted between $\Delta t_{max} = 0.1\ s$ and $\Delta t_{min} = 0.005\ s$, so that

changes in positions do not exceed a specified maximum. To avoid numerical artifacts when $\Delta t = \Delta t_{min}$, a maximum repulsive force threshold (F_{max}) is implemented. As long as F_{max} is set to values much higher than typical interaction forces, overcompression of the particles does not result in overlap between particle centerlines (a physically impossible arrangement). The main reason for implementing this force threshold is to allow overlaps from the initially random configuration to resolve without displacements exceeding those that would result from typical particle-particle collisions.

A.2.2 Simulation details: the steady state

The following description applies to all steady-state simulations described in sections 4.2, 4.3, and 4.4.

The bacteria are initially placed randomly throughout the space, with random initial orientations. Throughout a simulation, the configuration of the bacteria (positions, orientations, and lengths) were collected every 20 s. The parameters defining individual movement mechanics remained the same as in section 4.1 (except as noted in the introduction of section 4.2 regarding slight differences in implementation of polarity reversals and pilus retractions).

A.2.3 Calculation of $\Delta\rho$ and λ

Calculating $\Delta\rho$: Quantification of density distributions on any length scale can be achieved by dividing space into discrete subregions ς of area a_{sub} (here, the subregions were 10×10 μm squares, for $a_{sub} = 100$ μm^2) and calculating the density within each subregion. A histogram of the density values of each subregion will differ dramatically for equilibrium and nonequilibrium states. For equilibrium, random configurations, the distribution will peak at the average value, which is equal to the global density, $\rho = N/L^2$, and the density fluctuations (standard deviation) of

randomly distributed particles will obey $\Delta\rho_{eq} = \sqrt{\langle n \rangle}/a_{sub}$ where $\langle n \rangle = \rho a_{sub}$ is the expectation value for the population of each subregion at equilibrium.

The density distribution values in Figure 4.21(d) represent the fractions of the total area containing the indicated particle densities. These are calculated by counting the number q of subspaces containing the indicated density $\rho(\varsigma)$ and computing the time average of qa_{sub}/L^2 for the steady state. This results in a single histogram of local density for the entire steady state. The fluctuation magnitude [Fig. 4.21(e)] is simply the standard deviation of these discrete local density values.

Calculating λ: The number fluctuation exponent λ quantifies how spatial fluctuations in particle number scale with the size of the subspace area used to count them. As mentioned above, in equilibrium systems $\Delta n \propto \langle n \rangle^{0.5}$. However, if nonequilibrium conditions are scale-independent, changing $\langle n \rangle$ by varying a_{sub} will give $\Delta n \propto \langle n \rangle^{\lambda}$, with $\lambda > 0.5$ ('giant' number fluctuations).

A.2.4 Calculation of CSD

I calculated these cluster size distributions by creating a sparse adjacency matrix containing nearest-neighbor lists of each bacterium in each moment in time for which data was collected (every 20 s). Neighbors were defined by calculating the distances between cell centerlines [107], and defining those cells within a threshold distance of 1.5 μm as neighbors. This threshold distance is slightly longer than the repulsion distance of 1 μm, but short enough to exclude second-nearest neighbors.

The cluster size probability density (CSD) represents the probability that a particle selected randomly in the steady state will belong to a cluster of a given size. CSD values are computed from the adjacency matrix: neighbors of increasing degree are identified until the unique list of particles within the cluster does not change with further iterations. The cluster size is the number of particles identified in this way. Histograms of the cluster size distribution were plotted by binning the

cluster size values for each particle into bins of increasing size (up to the system size N, $\{s = 1^2,\ 2^2,\ 3^2 ...\ [s > N]\}$). These histograms are averaged over the steady-state time period, and normalized by bin width to reflect the probability $[P(s)]$ of randomly identifying a particle within the size range defined by each bin.

To identify steady-state behavior, I generated a histogram of probabilities for each time-step and a 2D image of the values was examined to evaluate whether the system had reached the steady state.

A.2.5 Code summary: collective behavior of twitching rods

The simulation code used to produce the simulations in section 4.2 can be found here [106], in the folder **TR_PB_CZ_thesis**.

Code for density fluctuation and scaling exponent (λ) determination can be found here [106], in the folder **drho_dN_CZ_thesis**.

Code for the generation of neighbor lists and CSD calculations can be found here [106] in the folder **N_lists_CSD_CZ_thesis**.

A.3 Supplement to section 4.3

A.3.1 $\langle S \rangle$ for collision model with stochastic sampling

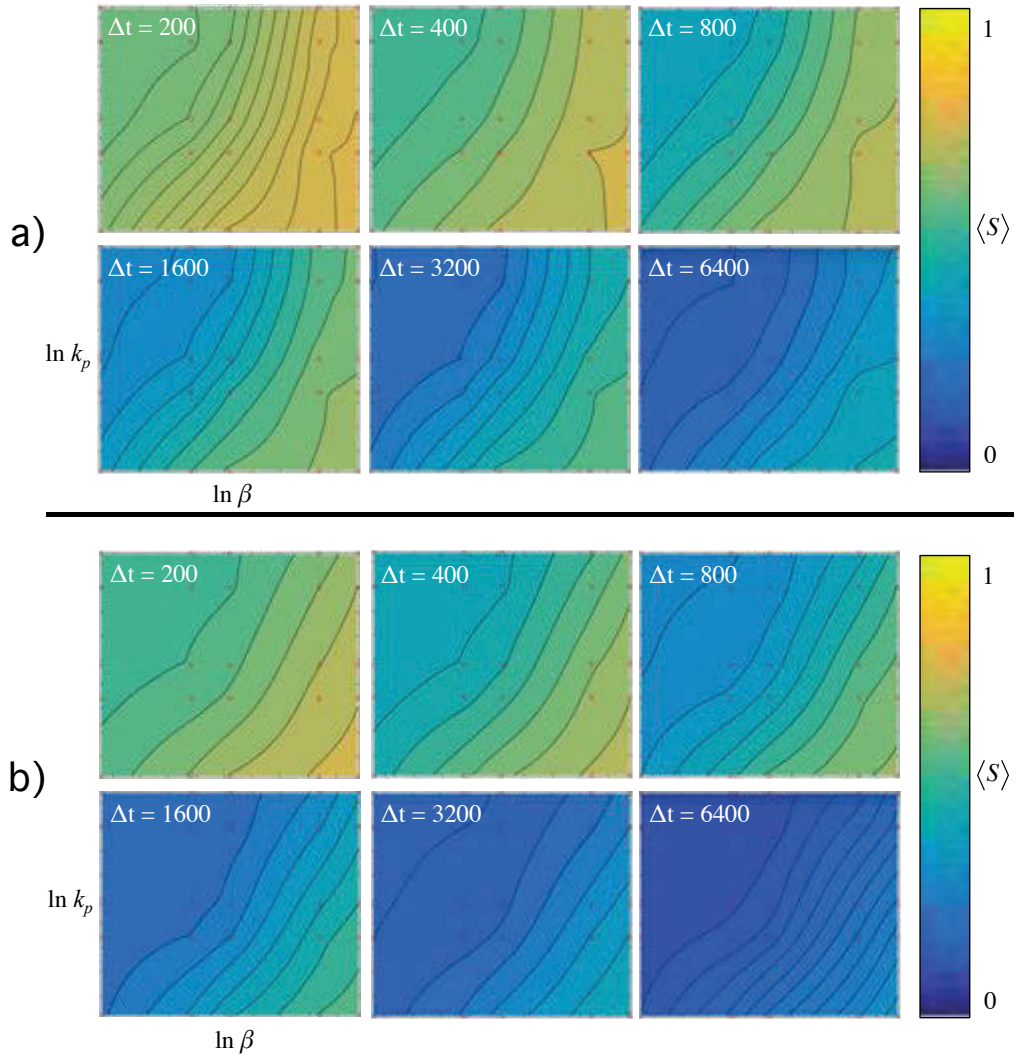

FIGURE A.2: Interpolated contour maps of the stigmergy parameter $\langle S \rangle$ as a function of EPS degradation rate β, deposition rate k_p, and time interval Δt. Here, repulsive collisions between cells were enabled. For both (a) and (b), spatial sampling was stochastic ($t_{ret} = 10\ s$). Data calculated from simulations are shown as red circles superimposed on the interpolated contour. When spatial sampling is stochastic, trail following does not occur for either of the populations tested ($N = 125$ (a), $N = 250$ (b)).

A.3.2 Code summary: EPS trail following

Code used to produce the simulations in section 4.3 can be found here [106], in the folder **EPS_only_CZ_thesis**.

Code used to calculate the path-following parameter $\langle S \rangle$ can be found here [106] in the MATLAB (.m) file **path_following_EPS_only_01_12_16.m**.

A.4 Supplement to section 4.4

A.4.1 Table of parameters

The parameter values listed in table A.1 pertain specifically to section 4.4, but are also used in other sections where applicable, unless stated otherwise.

TABLE A.1: Parameters

Parameter	Effect	Value(s) used
	Rod mechanics	
w	Rod width	w
l_{min}	Minimum rod length	$3w$
l_{max}	Maximum rod length	$7w$
F_r	Repulsive force constant	ws^{-1}
μ	Friction coefficient	w^{-1}
	Motility	
F_{ret}	Pilus retraction force	$1.5ws^{-1}$
r_{pili}	Length of pilus	l_{min}
ϕ	Angular range of pilus	0.5π
t_{ret}	Mean retraction time	$10s$
t_{rev}	Mean reversal period	$1000s$
σ_{rev}	St. dev. t_{rev}	$t_{rev}/5$
	Furrowing	
γ	Stiffness of substratum	$[0.001, 1.6]$
$k_U = \gamma k_s$	Deformation rate	$0.05s^{-1}[\Delta x]^{-2}$
$\beta_U = \gamma\beta_s$	Restitution rate	$2.5 \times 10^{-4}\ s^{-1}$
	EPS trails	
P_{min}	Minimum pilus attachment probability	0.1
P_{max}	Maximum pilus attachment probability	0.3
k_p	EPS deposition rate	$0.1\ s^{-1}[\Delta x]^{-2}$
β_p	EPS degradation rate	$5 \times 10^{-4}s^{-1}$
	Implementation	
Δx	Grid resolution	$w/4$
C_{max}	Max. tracer count per pixel	$1 \times [\Delta x]^2$
L	Simulation box dimension	$160w$
N	Number of particles	1000
t_f	Simulation duration	$5.0 \times 10^4 s^*$
t_{rec}	Data acquisition interval	$20s$
F_{max}	Max. allowed repulsion force	$10ws^{-1}$
Δt_{max}	Maximum discrete time step	$0.1s$
Δt_{min}	Minimum discrete time step	$0.005s$

*For $\gamma = [0.9, 1, 1.1, 1.3]$, $t_f = 1.0 \times 10^5$

A.4.2 Calculation of $\langle\Phi\rangle$

To calculate the average nematic orientational coherence value $\langle\Phi\rangle(DoS)$ for the ensemble as a function of DoS between particles we used the following procedure: for each particle, the orientations of n neighbors at increasing DoS are compared with that of the particle in question and averaged via the orientational coherence function:

$$\Phi_i(DoS) = \frac{\sum_{j=1}^{n} 2[\cos(\theta_i - \theta_j)]^2 - 1}{n(DoS)}\,, \tag{A.1}$$

and the ensemble average, $\langle\phi\rangle_N$ vs DoS over the entire system is calculated.

A.4.3 Calculation of ζ

The configurational correlation ζ is the ratio of two different configurational decay times. The first, τ_1, is a measure of the time it takes for a global configuration to cease resembling itself. It is computed as follows: the simulation box is divided into square subregions with side length set equal to the minimum particle length. At time t_i each subregion in the grid is assigned a 1 if occupied by at least one particle, or 0 otherwise, we refer to this as the structural configuration matrix $S(t_i)$.

We take the sum over the elements of $S(t_i)$ to find $z(t_i)$. $S(t_i)$ is then multiplied element-wise with the subsequent configuration at $t = t + dt$ and the result is $S(t_i + dt)$ this process is repeated for subsequent configurations and we find $R(t - t_i)$, the normalized sum over all elements of $S(t)$, so that $R(t - t_i) = z(t - t_i)/z(t_i)$ approaches zero as $t - t_i$ increases. Fitting $R(t - t_i)$ to a single exponential decay gives

$$R(t - t_i) = e^{[-1/\tau_1][t-t_i]}\,. \tag{A.2}$$

The other type of configurational decay constant, τ_2, is calculated similarly: at t_i, each particle is assigned an index corresponding to its grid position, and the correlation value, $\kappa(t_i) = 1$. If a particle's index changes in subsequent configurations the correlation value $\kappa(t - t_i)$ decreases by $1/N$, the decay is cumulative in time, ie: $\kappa(t - t_i)$ does not recover if a particle goes back to its location at t_i. The decay is fit to an exponential model so that

$$\kappa(t - t_i) = e^{[-1/\tau_2][t-t_i]}\,. \tag{A.3}$$

For a given simulation in the steady state $\zeta = \tau_1/\tau_2$ is a constant that fluctuates about a defined mean.

A.4.4 Code summary: sematectonic stigmergy

The simulation code used to generate the data in section 4.4 is available here [106], in the folder **Emergent_patterns_CZ_PRE_script**.

Code for analyzing orientational coherence $\langle\Phi\rangle$ as a function of DoS or r_{ij} is available here [106] in the folder **orientational_corelation** (Note: calculating $\langle\Phi\rangle(DoS)$ requires neighbor lists, see A.2.5)

Code for calculating the configurational correlation coefficient ζ is available here [106] in the folder **configurational_correlation**.

Appendix B

Supplement to Chapter 5

B.1 Supplement to sections 5.2 and 5.3

B.1.1 Calculating anisotropy parameter ΔS_ϕ

In section 5.2 this metric is used to calculate the anisotropy of the entire colony where ϕ represents the angular coordinate of each cell's position relative to the colony center of mass. In section 5.3 this metric is used to quantify local anisotropy, and is applied to the angular coordinates $\phi(j \in k)$ defining the vectors between a given cell's position and the positions of its k neighbors within a radius r defining the length scale of interest. In both cases the entropy of the ϕ distribution is defined as $S_\phi = \sum_i p_i(\phi) \ln p_i(\phi)$, where i denotes one of n discrete bins in the histogram of the distribution, and $p_i(\phi)$ is the probability of randomly selecting a ϕ value within the ith bin. By comparing S_ϕ to the value associated with the uniform distribution $S_{uni} = \ln n$, the anisotropy parameter is calculated: $\Delta S_\phi = [1 - S_\phi/S_{uni}] - H_{min}(n,k)$ where $H_{min}(n,k) \approx \frac{n}{k}[0.37n^{-0.38} + 0.0045]$ is an empirically-derived correction factor (see A.1.2). For a linear, 1D distribution $\Delta S_\phi \approx 1$, while for isotropic (i.e., circular) 2D distributions $\Delta S_\phi \approx 0$.

B.1.2 Code summary: section 5.2

Code for simulations of colony growth without stigmergy is available here [106] in the folder **Growing_twitching_rods_CZ_thesis**

Code for calculation of $\langle r\langle(t)$ and $\eta(r)$ is available here [106] in the MATLAB (.m) file **R_dist_growth_no_stig.m**.

Code for calculation of ΔS_ϕ as a function of replication cycle is available here [106] in the MATLAB (.m) file **symmetry_phi_GTR_no_stig.m**.

B.1.3 Code summary: section 5.3

Code for simulations of colony growth with stigmergy is available here [106] in the folder **Prop_aniso_script**

Code for calculation of ΔS_ϕ as a function of r is available here [106] in the MATLAB (.m) file **dS_phi_vs_r.m**.

Appendix C

Supplemental Movies

C.1 Supplemental movies: Chapter 3

- Movie S1: The advancing edge of a *Pseudomonas aeruginosa* interstitial biofilm (2000 s, 0.5 frame/s). This movie corresponds to Figure 3.3(a). (Supplemental Movie S1 in [98])
- Movie S2: The interior of a *Pseudomonas aeruginosa* interstitial biofilm (2000 s, 0.5 frame/s). This movie corresponds to Figure 3.3(b). (Supplemental Movie S2 in [98])

C.2 Supplemental movies: Chapter 4

- Movie S3: Simulated steady-state biofilm showing bacteria colored by orientation (red for horizontal, blue for vertical), corresponding to Figure 4.20(a) (soft substratum, $\gamma = 0.25$). (Supplemental Movie S1 in [92])

- Movie S4: Simulated steady-state biofilm showing bacteria colored by orientation (red for horizontal, blue for vertical), corresponding to Figure 4.20(c) (stiff substratum, $\gamma = 1.5$). (Supplemental Movie S2 in [92])

C.3 Supplemental movies: Chapter 5

- Movie S5: Simulated interstitial biofilm showing bacteria in red, EPS trails in green and substratum deformation in gray-scale. $\gamma = 0.25$, $k_U = 0.001$, ($1.35 \times 10^5 s$, 1000s/frame). (Supplemental Movie S3 in [98]).

- Movie S6: Simulated interstitial biofilm showing bacteria in red, EPS trails in green and substratum deformation in gray-scale. $\gamma = 0.5$, $k_U = 0.001$, ($1.35 \times 10^5 s$, 1000s/frame). (Supplemental Movie S4 in [98]).

- Movie S7: Simulated interstitial biofilm showing bacteria in red, EPS trails in green and substratum deformation in gray-scale. $\gamma = 1.0$, $k_U = 0.001$, ($1.35 \times 10^5 s$, 1000s/frame). (Supplemental Movie S5 in [98]).

- Movie S8: Simulated interstitial biofilm showing bacteria in red, EPS trails in green and substratum deformation in gray-scale. $\gamma = 0.5$, $k_U = 0.05$, ($1.35 \times 10^5 s$, 1000s/frame). (Supplemental Movie S6 in [98]).

- Movie S9: Simulated interstitial biofilm showing bacteria in red, EPS trails in green and substratum deformation in gray-scale. $\gamma = 1.5$, $k_U = 0.001$, ($1.25 \times 10^5 s$, 1000s/frame). (Supplemental Movie S7 in [98]).

- Movie S10: Simulated interstitial biofilm with EPS trail following disabled -pilus attachment is constant at $P_a = 0.5$. $\gamma = 0.5$, $k_U = 0.001$, ($1.35 \times 10^5 s$, 1000s/frame). (Supplemental Movie S8 in [98]).

Appendix D

Experimental Data Analysis

D.1 Image processing

The phase contrast microscopy time-series used to calculate growth rate was comprised of 1000 frames captured at 1 frame /2 s (2000 s). Phase contrast microscopy was performed using an Olympus IX71 inverted research microscope with a 100x 1.4 NA UPlanFLN objective, FViewII monochromatic camera and AnalySIS Research acquisition software (Olympus Australia, Notting Hill, VIC, Australia) fitted with an environmental chamber (Solent Scientific, Segensworth, UK).

The growth rates were determined by morphological analysis of the individual cells using a modified version of the BacFormatics image processing platform [35] which was developed in MATLAB. The calculated growth rates were slightly faster than the actual ones due to single-pixel trimming during image segmentation. To correct for this, we set the individual growth rate to $k_g = 3.5 \times 10^{-4}\ \mu\mathrm{m}s^{-1}$ in our simulations [Fig. 3.3(d)].

The source code for the beta version of the BacFormatics toolbox used for image segmentation and tracking in this work is available at:
https://github.com/ithreeMIF/BacFormatics_CZ/.

Briefly, the phase contrast images are inverted and segmented by applying a range filter, followed by local normalization [108], low-pass frequency filtering (using a vectorized version of the butterworth low-pass filter found here [109]), and thresholding. The resulting image of the cell bodies is multiplied by a binary mask that removes the spaces between cells. This "net" mask is created using morphological tophat filtering to isolate an image of the spaces between cells, followed by intensity thresholding, binarization, and inversion. After multiplication of the filtered image with the binary "net" mask, the absolute value of all pixel intensities is taken. The resulting binary image effectively segments individual cells. As a final step, segments are excluded from this image if they do not contain local maxima from an inverted version of the original phase contrast image. This process is summarized schematically in Fig. D.1.

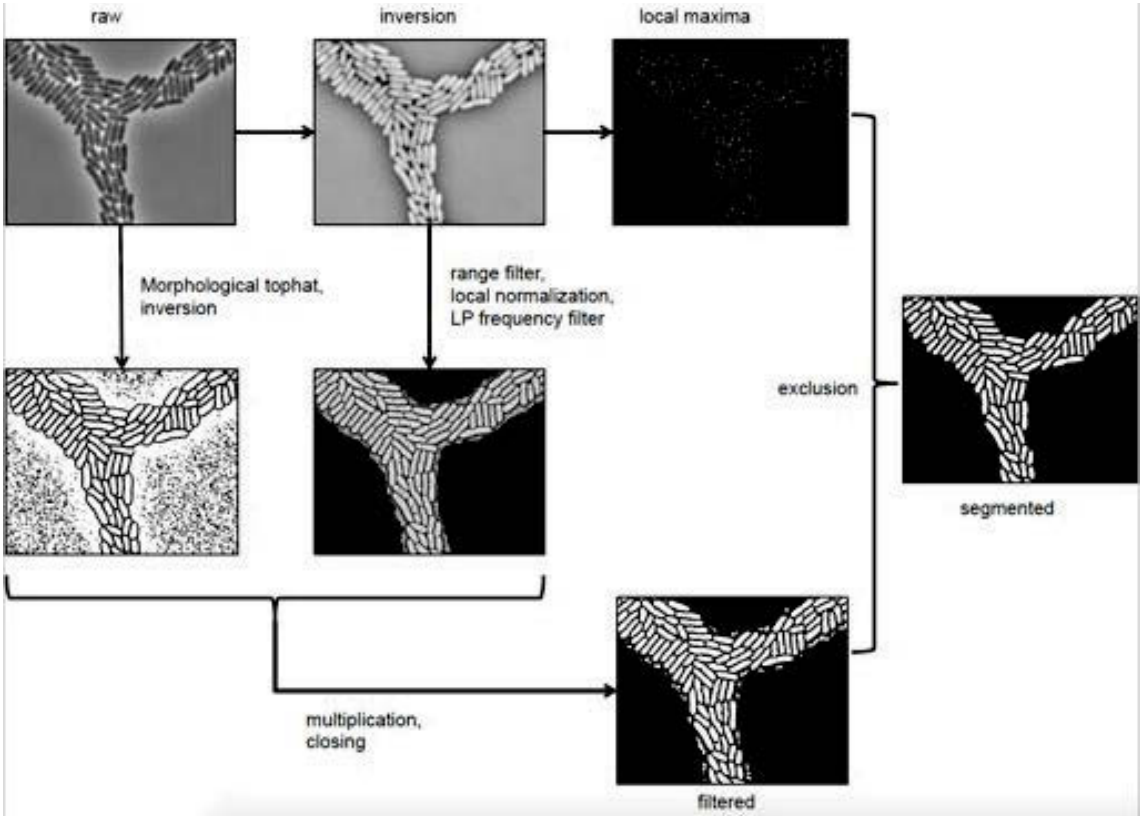

FIGURE D.1: Schematic of the image segmentation algorithm used to analyze raw microscopy data. The raw phase contrast images are translated into binary images containing only the pixels associated with bacterial cell bodies. The segmented images were used to estimate the growth rates of individual bacteria.

Cell centroid positions, orientations, lengths l, and widths w were estimated using the regionprops() function in the MATLAB image processing toolbox. Cell tracking was carried out by creating a distance matrix with the cell centroid positions in two consecutive frames and linking cell IDs based on the minimum distance traveled between frames.

D.2 Aspect ratio and growth rate calculations

Before estimating growth rate, we examined the length of each tracked cell as a function of time and identified discontinuities. These were identified based on a cutoff length variation between consecutive frames $\Delta l_{min} = 0.6$ μm (10 pixels) that is biologically unrealistic and is significant with respect to random variation in segment dimensions. Such discontinuities can occur naturally when cells divide, or when there are errors in segmentation that merge two or more cells, or split individual cells.

Between such discontinuities, the aspect ratio $\kappa = l/\langle w \rangle_t$ was calculated for each frame where $\langle w \rangle_t$ is the time average of the cell width, which should not change as the cell elongates. We estimated the rate of change of the aspect ratio for each continuous time-series of lengths by applying a linear regression to each data sequence exceeding a threshold duration ($\Delta l_{min} = 400s$, 200 frames). The slope of the linear regression accounts for an individual growth rate value. The growth rate values in the main text [Fig. 3.3(d)] therefore represent linear approximations of the rate at which the aspect ratio of each cell is increasing. This is appropriate since our model uses the cell width as its fundamental unit of length $w = 1$ μm.

Cell lengths before (l_1) and after (l_2) division were calculated as follows: first, cells that were successfully tracked for more than 100 frames were identified. Those with length $l_1 < 3$ μm were disqualified. The length data of the remaining cells was examined for single discontinuities in length $\Delta l = l_2 - l_1$ that satisfied $l_2 < 0.7 l_1$.

The length before and after such discontinuities was used as the pre- and post-division length to calculate aspect ratio from the lengths l_1 and l_2 and time-averaged cell width $\langle w_i \rangle_t$.

D.2.1 Code summary: aspect ratio and growth rate

Code used for calculating cell aspect ratios, growth rates, and aspect ratio before and after division is available here [106] in the folder **aspect_ratio_analysis_CZ_thesis**.

(Note: this code operates on data extracted from segmented images by the BacFormatics toolbox as explained in D.1)

Bibliography

[1] Terrence W Deacon. "Emergence: The Hole at the Wheel's Hub1". In: *The Re-Emergence of Emergence: The Emergentist Hypothesis from Science to Religion: The Emergentist Hypothesis from Science to Religion* 159 (2006), p. 111.

[2] Michele Ballerini et al. "Empirical investigation of starling flocks: a benchmark study in collective animal behaviour". In: *Animal Behaviour* 76.1 (2008), pp. 201–215.

[3] Michele Ballerini et al. "Interaction ruling animal collective behavior depends on topological rather than metric distance: Evidence from a field study". In: *Proceedings of the National Academy of Sciences* 105.4 (2008), pp. 1232–1237.

[4] William Bialek et al. "Statistical mechanics for natural flocks of birds". In: *Proceedings of the National Academy of Sciences* 109.13 (2012), pp. 4786–4791.

[5] Christopher Charles Whiston Taylor et al. *The atomists, Leucippus and Democritus: fragments: a text and translation with a commentary*. Vol. 5. University of Toronto Press, 2010.

[6] Aristotle and Arthur Platt. *On the generation of animals*. Kessinger Publishing, 2008.

[7] Ilya Prigogine and Isabelle Stengers. *Order out of chaos: man's new dialogue with nature*. New Science Library. Distributed by Random House, 1984.

[8] Eshel Ben-Jacob et al. “Generic modelling of cooperative growth patterns in bacterial colonies”. In: *Nature* 368.6466 (1994), pp. 46–49.

[9] Ferdi L Hellweger and Vanni Bucci. “A bunch of tiny individuals—Individual-based modeling for microbes”. In: *Ecological Modelling* 220.1 (2009), pp. 8–22.

[10] Steven A MacKay. “Computer simulation of aggregation in Dictyostelium discoideum”. In: *Journal of Cell Science* 33.1 (1978), pp. 1–16.

[11] Ioannis Karamouzas, Brian Skinner, and Stephen J Guy. “Universal power law governing pedestrian interactions”. In: *Physical Review Letters* 113.23 (2014), p. 238701.

[12] Peter M Allen and Michele Sanglier. “Dynamic models of urban growth”. In: *Journal of Social and Biological Structures* 1.3 (1978), pp. 265–280.

[13] Peter M Allen and Michèle Sanglier. “A dynamic model of urban growth: II”. In: *Journal of Social and Biological Structures* 2.4 (1979), pp. 269–278.

[14] Tamás Vicsek and Anna Zafeiris. “Collective motion”. In: *Physics Reports* 517.3 (2012), pp. 71–140.

[15] Craig W Reynolds. “Flocks, herds and schools: A distributed behavioral model”. In: *ACM SIGGRAPH Computer Graphics* 21.4 (1987), pp. 25–34.

[16] Tamás Vicsek et al. “Novel type of phase transition in a system of self-driven particles”. In: *Physical Review Letters* 75.6 (1995), p. 1226.

[17] Eric Bonabeau. “Editor’s introduction: stigmergy”. In: *Artificial Life* 5.2 (1999), pp. 95–96.

[18] Francis Heylighen. “Stigmergy as a universal coordination mechanism I: Definition and components”. In: *Cognitive Systems Research* 38 (2016), pp. 4–13. ISSN: 1389-0417. DOI: http://dx.doi.org/10.1016/j.cogsys.2015.12.002.

[19] Francis Heylighen. "Stigmergy as a universal coordination mechanism II: Varieties and evolution". In: *Cognitive Systems Research* 38 (2016), pp. 50 –59. ISSN: 1389-0417. DOI: http://dx.doi.org/10.1016/j.cogsys.2015.12.007.

[20] Rasika M Harshey. "Bacterial motility on a surface: many ways to a common goal". In: *Annual Reviews in Microbiology* 57.1 (2003), pp. 249–273.

[21] Christoph Ratzke and Jeff Gore. "Self-organized patchiness facilitates survival in a cooperatively growing Bacillus subtilis population". In: *Nature Microbiology* 1.5 (2016), p. 16022.

[22] Stuart A West et al. "Social evolution theory for microorganisms". In: *Nature Reviews Microbiology* 4.8 (2006), pp. 597–607.

[23] Francesco Ginelli et al. "Large-scale collective properties of self-propelled rods". In: *Physical Review Letters* 104.18 (2010), p. 184502.

[24] Philip S Stewart and J William Costerton. "Antibiotic resistance of bacteria in biofilms". In: *The Lancet* 358.9276 (2001), pp. 135–138.

[25] James A Shapiro. "Thinking about bacterial populations as multicellular organisms". In: *Annual Reviews in Microbiology* 52.1 (1998), pp. 81–104.

[26] Luanne Hall-Stoodley, J William Costerton, and Paul Stoodley. "Bacterial biofilms: from the natural environment to infectious diseases". In: *Nature Reviews Microbiology* 2.2 (2004), pp. 95–108.

[27] Hiroshi Fujikawa and Mitsugu Matsushita. "Fractal growth of Bacillus subtilis on agar plates". In: *Journal of the physical society of japan* 58.11 (1989), pp. 3875–3878.

[28] Mitsugu Matsushita and Hiroshi Fujikawa. "Diffusion-limited growth in bacterial colony formation". In: *Physica A: Statistical Mechanics and its Applications* 168.1 (1990), pp. 498–506.

[29] Kristopher Page, Michael Wilson, and Ivan P Parkin. "Antimicrobial surfaces and their potential in reducing the role of the inanimate environment in the incidence of hospital-acquired infections". In: *Journal of Materials Chemistry* 19.23 (2009), pp. 3819–3831.

[30] Joerg C Tiller. "Antimicrobial surfaces". In: *Bioactive Surfaces*. Springer, 2010, pp. 193–217.

[31] Michel Godin et al. "Using buoyant mass to measure the growth of single cells". In: *Nature Methods* 7.5 (2010), pp. 387–390.

[32] Tâm Mignot et al. "Evidence that focal adhesion complexes power bacterial gliding motility". In: *Science* 315.5813 (2007), pp. 853–856.

[33] Nuno M Oliveira, Kevin R Foster, and William M Durham. "Single-cell twitching chemotaxis in developing biofilms". In: *Proceedings of the National Academy of Sciences* (2016), p. 201600760.

[34] Jeffrey M Skerker and Howard C Berg. "Direct observation of extension and retraction of type IV pili". In: *Proceedings of the National Academy of Sciences* 98.12 (2001), pp. 6901–6904.

[35] Lynne Turnbull et al. "Explosive cell lysis as a mechanism for the biogenesis of bacterial membrane vesicles and biofilms". In: *Nature Communications* 7 (2016).

[36] Dmitri Volfson et al. "Biomechanical ordering of dense cell populations". In: *Proceedings of the National Academy of Sciences* 105.40 (2008), pp. 15346–15351.

[37] Ping Wang et al. "Robust growth of Escherichia coli". In: *Current Biology* 20.12 (2010), pp. 1099–1103.

[38] Fernando Peruani, Andreas Deutsch, and Markus Bär. "Nonequilibrium clustering of self-propelled rods". In: *Physical Review E* 74.3 (2006), p. 030904.

[39] Fernando Peruani et al. “Collective motion and nonequilibrium cluster formation in colonies of gliding bacteria”. In: *Physical Review Letters* 108.9 (2012), p. 098102.

[40] Melisa Hendrata et al. “Experimentally guided computational model discovers important elements for social behavior in myxobacteria”. In: *PloS One* 6.7 (2011), e22169.

[41] Antony B Holmes, Sara Kalvala, and David E Whitworth. “Spatial simulations of myxobacterial development”. In: *PLoS Computational Biology* 6.2 (2010), e1000686.

[42] FDC Farrell et al. “Mechanically driven growth of quasi-two-dimensional microbial colonies”. In: *Physical Review Letters* 111.16 (2013), p. 168101.

[43] Pushpita Ghosh et al. “Mechanically-driven phase separation in a growing bacterial colony”. In: *Proceedings of the National Academy of Sciences* 112.17 (2015), E2166–E2173.

[44] Matthew AA Grant et al. “The role of mechanical forces in the planar-to-bulk transition in growing Escherichia coli microcolonies”. In: *Journal of The Royal Society Interface* 11.97 (2014), p. 20140400.

[45] Erin S Gloag et al. “Self-organization of bacterial biofilms is facilitated by extracellular DNA”. In: *Proceedings of the National Academy of Sciences* 110.28 (2013), pp. 11541–11546.

[46] Erin S Gloag et al. “Stigmergy: a key driver of self-organization in bacterial biofilms”. In: *Communicative & Integrative Biology* 6.6 (2013), pp. 11541–6.

[47] Erin S Gloag, Lynne Turnbull, and Cynthia B Whitchurch. “Bacterial Stigmergy: An Organising Principle of Multicellular Collective Behaviours of Bacteria”. In: *Scientifica* 2015 (2015).

[48] Annalese BT Semmler, Cynthia B Whitchurch, and John S Mattick. “A re-examination of twitching motility in Pseudomonas aeruginosa”. In: *Microbiology* 145.10 (1999), pp. 2863–2873.

[49] Olga Sozinova et al. “A three-dimensional model of myxobacterial aggregation by contact-mediated interactions”. In: *Proceedings of the National Academy of Sciences of the United States of America* 102.32 (2005), pp. 11308–11312.

[50] Jörn Starruß et al. “Pattern-formation mechanisms in motility mutants of Myxococcus xanthus”. In: *Interface Focus* (2012), rsfs20120034.

[51] Yilin Wu et al. “Social interactions in myxobacterial swarming”. In: *PLoS Computational Biology* 3.12 (2007), e253.

[52] Robert P Burchard. “Trail Following by Gliding Bacteria.” In: *Journal of Bacteriology* 152.1 (1982), pp. 495–501.

[53] Rajesh Balagam and Oleg A Igoshin. “Mechanism for collective cell alignment in Myxococcus xanthus bacteria”. In: *PLoS Computational Biology* 11.8 (2015), e1004474.

[54] Anatolij Gelimson et al. “Multicellular self-organization of P. aeruginosa due to interactions with secreted trails”. In: *Physical Review Letters* 117.17 (2016), p. 178102.

[55] W. Till Kranz et al. “Effective Dynamics of Microorganisms That Interact with Their Own Trail”. In: *Physical Review Letters* 117 (3 2016), p. 038101. DOI: 10.1103/PhysRevLett.117.038101.

[56] Erik M Rauch, Mark M Millonas, and Dante R Chialvo. “Pattern formation and functionality in swarm models”. In: *Physics Letters A* 207.3 (1995), pp. 185–193.

[57] H.H. Heunert. *Swarm Development and Morphogenesis in the Myxobacteria ‘Archangium’, ‘Myxococcus’, ‘Chondrococcus’ And ‘Chondromyces’*. URL: http://bufvc.ac.uk/dvdfind/index.php/title/20852.

[58] Erin S Gloag et al. “Stigmergy co-ordinates multicellular collective behaviours during Myxococcus xanthus surface migration”. In: *Scientific Reports* 6 (2016).

[59] Dirk Helbing et al. “Active walker model for the formation of human and animal trail systems”. In: *Physical Review E* 56.3 (1997), p. 2527.

[60] Emmanuel Boissard, Pierre Degond, and Sebastien Motsch. “Trail formation based on directed pheromone deposition”. In: *Journal of Mathematical Biology* 66.6 (2013), pp. 1267–1301.

[61] Iain D Couzin and Nigel R Franks. “Self-organized lane formation and optimized traffic flow in army ants”. In: *Proceedings of the Royal Society of London B: Biological Sciences* 270.1511 (2003), pp. 139–146.

[62] Dale Kaiser. “Myxococcus-from single-cell polarity to complex multicellular patterns”. In: *Annual Review of Genetics* 42 (2008), pp. 109–130.

[63] Alfred M Spormann. “Gliding Motility in Bacteria: Insights from Studies ofMyxococcus xanthus”. In: *Microbiology and Molecular Biology Reviews* 63.3 (1999), pp. 621–641.

[64] Hong Sun, David R Zusman, and Wenyuan Shi. “Type IV pilus of Myxococcus xanthus is a motility apparatus controlled by the frz chemosensory system”. In: *Current Biology* 10.18 (2000), pp. 1143–1146.

[65] J Henrichsen. “Twitching motility”. In: *Annual Reviews in Microbiology* 37.1 (1983), pp. 81–93.

[66] Daniel B Kearns. “A field guide to bacterial swarming motility”. In: *Nature Reviews Microbiology* 8.9 (2010), pp. 634–644.

[67] Berenike Maier and Gerard CL Wong. “How bacteria use type IV pili machinery on surfaces”. In: *Trends in Microbiology* 23.12 (2015), pp. 775–788.

[68] John S Mattick. “Type IV pili and twitching motility”. In: *Annual Reviews in Microbiology* 56.1 (2002), pp. 289–314.

[69] Vladimir Pelicic. “Type IV pili: e pluribus unum?” In: *Molecular Microbiology* 68.4 (2008), pp. 827–837.

[70] Walter E Stamm. "Catheter-associated urinary tract infections: epidemiology, pathogenesis, and prevention". In: *The American Journal of Medicine* 91.3 (1991), S65–S71.

[71] Betsy Foxman. "Epidemiology of urinary tract infections: incidence, morbidity, and economic costs". In: *The American Journal of Medicine* 113.1 (2002), pp. 5–13.

[72] Davide Campoccia, Lucio Montanaro, and Carla Renata Arciola. "The significance of infection related to orthopedic devices and issues of antibiotic resistance". In: *Biomaterials* 27.11 (2006), pp. 2331–2339.

[73] James F Schumacher et al. "Engineered nanoforce gradients for inhibition of settlement (attachment) of swimming algal spores". In: *Langmuir* 24.9 (2008), pp. 4931–4937.

[74] Erin Gloag et al. "Micro-Patterned Surfaces that Exploit Stigmergy to Inhibit Biofilm Expansion". In: *Frontiers in Microbiology* 7 (2016), p. 2157. ISSN: 1664-302X. DOI: 10.3389/fmicb.2016.02157.

[75] Thilo Köhler et al. "Swarming of Pseudomonas aeruginosa is dependent on cell-to-cell signaling and requires flagella and pili". In: *Journal of Bacteriology* 182.21 (2000), pp. 5990–5996.

[76] Joerg Overhage et al. "Identification of genes involved in swarming motility using a Pseudomonas aeruginosa PAO1 mini-Tn5-lux mutant library". In: *Journal of bacteriology* 189.5 (2007), pp. 2164–2169.

[77] Michael J Richards et al. "Nosocomial infections in medical intensive care units in the United States. National Nosocomial Infections Surveillance System." In: *Critical Care Medicine* 27.5 (1999), pp. 887–892.

[78] Lynne Turnbull and Cynthia B. Whitchurch. "Motility Assay: Twitching Motility". In: *Pseudomonas Methods and Protocols*. Ed. by Alain Filloux and Juan-Luis Ramos. New York, NY: Springer New York, 2014, pp. 73–86. ISBN: 978-1-4939-0473-0. DOI: 10.1007/978-1-4939-0473-0_9.

[79] Edward J Schantz and Max A Lauffer. “Diffusion measurements in agar gel”. In: *Biochemistry* 1.4 (1962), pp. 658–663.

[80] Ariel Amir. “Cell size regulation in bacteria”. In: *Physical Review Letters* 112.20 (2014), p. 208102.

[81] Ilya Soifer, Lydia Robert, and Ariel Amir. “Single-cell analysis of growth in budding yeast and bacteria reveals a common size regulation strategy”. In: *Current Biology* 26.3 (2016), pp. 356–361.

[82] Maxime Deforet, Dave van Ditmarsch, and João B Xavier. “Cell-size homeostasis and the incremental rule in a bacterial pathogen”. In: *Biophysical Journal* 109.3 (2015), pp. 521–528.

[83] Michel Godin et al. “Measuring the mass, density, and size of particles and cells using a suspended microchannel resonator”. In: *Applied physics letters* 91.12 (2007), p. 123121.

[84] Carmen L Giltner et al. “The Pseudomonas aeruginosa type IV pilin receptor binding domain functions as an adhesin for both biotic and abiotic surfaces”. In: *Molecular Microbiology* 59.4 (2006), pp. 1083–1096.

[85] Kun Zhao et al. “Psl trails guide exploration and microcolony formation in Pseudomonas aeruginosa biofilms”. In: *Nature* 497.7449 (2013), pp. 388–391.

[86] Ian W Sutherland. “The biofilm matrix–an immobilized but dynamic microbial environment”. In: *Trends in Microbiology* 9.5 (2001), pp. 222–227.

[87] Erin J van Schaik et al. “DNA binding: a novel function of Pseudomonas aeruginosa type IV pili”. In: *Journal of Bacteriology* 187.4 (2005), pp. 1455–1464.

[88] Uri Alon et al. “Robustness in bacterial chemotaxis”. In: *Nature* 397.6715 (1999), pp. 168–171.

[89] Tau-Mu Yi et al. “Robust perfect adaptation in bacterial chemotaxis through integral feedback control”. In: *Proceedings of the National Academy of Sciences* 97.9 (2000), pp. 4649–4653.

[90] Valéry Normand et al. “New insight into agarose gel mechanical properties”. In: *Biomacromolecules* 1.4 (2000), pp. 730–738.

[91] Julien Tremblay and Eric Déziel. “Improving the reproducibility of Pseudomonas aeruginosa swarming motility assays”. In: *Journal of Basic Microbiology* 48.6 (2008), pp. 509–515.

[92] Cameron Zachreson et al. “Emergent pattern formation in an interstitial biofilm”. In: *arXiv preprint arXiv:1611.04223* (2016).

[93] Cameron Zachreson et al. “Emergent pattern formation in an interstitial biofilm”. In: *Physical Review E (accepted)* (20017).

[94] Yinuo Li et al. “Extracellular polysaccharides mediate pilus retraction during social motility of Myxococcus xanthus”. In: *Proceedings of the National Academy of Sciences* 100.9 (2003), pp. 5443–5448.

[95] Wenyuan Shi, Frances K Ngok, and David R Zusman. “Cell density regulates cellular reversal frequency in Myxococcus xanthus”. In: *Proceedings of the National Academy of Sciences* 93.9 (1996), pp. 4142–4146.

[96] Lei Yang et al. “In situ growth rates and biofilm development of Pseudomonas aeruginosa populations in chronic lung infections”. In: *Journal of Bacteriology* 190.8 (2008), pp. 2767–2776.

[97] Bart Gottenbos, HCVD Mei, and Henk J Busscher. “Initial adhesion and surface growth of Staphylococcus epidermidis and Pseudomonas aeruginosa on biomedical polymers”. In: *Journal of Biomedical Materials Research* 50.2 (2000), pp. 208–214.

[98] Cameron Zachreson et al. “Network patterns in exponentially growing 2D biofilms”. In: *arXiv preprint arXiv:1701.00194* (2017).

[99] Denis Boyer et al. “Buckling instability in ordered bacterial colonies”. In: *Physical Biology* 8.2 (2011), p. 026008.

[100] Jonathon Howard, Stephan W Grill, and Justin S Bois. "Turing's next steps: the mechanochemical basis of morphogenesis". In: *Nature Reviews Molecular Cell Biology* 12.6 (2011), pp. 392–398.

[101] Mitchell L Cohen. "Epidemiology of drug resistance: implications for a post-antimicrobial era." In: *Science(Washington)* 257.5073 (1992), pp. 1050–1055.

[102] Thien-Fah C Mah and George A O'Toole. "Mechanisms of biofilm resistance to antimicrobial agents". In: *Trends in Microbiology* 9.1 (2001), pp. 34–39.

[103] Timothy J Rudge et al. "Computational modeling of synthetic microbial biofilms". In: *ACS Synthetic Biology* 1.8 (2012), pp. 345–352.

[104] Laurent A Lardon et al. "iDynoMiCS: next-generation individual-based modelling of biofilms". In: *Environmental Microbiology* 13.9 (2011), pp. 2416–2434.

[105] MC Marchetti et al. "Hydrodynamics of soft active matter". In: *Reviews of Modern Physics* 85.3 (2013), p. 1143.

[106] URL: `https://github.com/cjzachreson/CZ_thesis_code`.

[107] Carlos Vega and Santiago Lago. "A fast algorithm to evaluate the shortest distance between rods". In: *Computers & chemistry* 18.1 (1994), pp. 55–59.

[108] Xiong, Guanglei. (2005). Local Normalization. Retrieved on Aug 1, 2016 from `http://au.mathworks.com/matlabcentral/fileexchange/8303-local-normalization`.

[109] Athiq, Mohamed. (2013). Frequency domain filtering for grayscale images. Retrieved on Aug 1, 2016 from `https://au.mathworks.com/matlabcentral/fileexchange/40579-frequency-domain-filtering-for-grayscale-images`.

Books only

[5] Christopher Charles Whiston Taylor et al. *The atomists, Leucippus and Democritus: fragments: a text and translation with a commentary*. Vol. 5. University of Toronto Press, 2010.

[6] Aristotle and Arthur Platt. *On the generation of animals*. Kessinger Publishing, 2008.

[7] Ilya Prigogine and Isabelle Stengers. *Order out of chaos: man's new dialogue with nature*. New Science Library. Distributed by Random House, 1984.